Scanning probe force microscopy of III-V semiconductor structures

C. Kameni Boumenou

2017

Scanning probe force microscopy of III-V semiconductor structures

By

Christian Kameni Boumenou

Submitted in partial fulfilment of the requirements for the degree of

MAGISTER SCIENTIAE

in the Faculty of Science at the

Nelson Mandela Metropolitan University

December 2017

Supervisor: Dr Z. N. Urgressa

Co-Supervisor: Prof J. R. Botha

ACKNOWLEDGEMENTS

I would like to thank and express my sincere gratitude:

- My supervisor, Dr Zelalem Urgressa, who supported me throughout the full completion of this project. He introduced me to the scanning probe force microscopy laboratory and has always been there to listen and engage heartily and endlessly in serious research-related discussions.
- My co-supervisor, Prof J. Reinhard Botha, who gave me the opportunity to work on this project within his group. This dissertation should not be successfully completed without his advices and encouragements. For me, he appears as one of the friendly supervisor that I have made so far.
- All the professors and staff who have helped me throughout my time in the physics department, the nanophotonics group, and the international office as well.
- Dr Jackie Nel at the University of Pretoria, for allowing me to visit their research group, and for her precious advices and discussions.
- All my colleagues at NMMU for their enormous support and a good conducive atmosphere in the lab.
- The South African Research Chairs Initiative of the Department of Science and Technology, the National Research Foundation and Nelson Mandela Metropolitan University for funding my studies.
- My parents for their encouragement and support.
- Finally, and most importantly, to Mrs Linda Zaverie for her understanding and real love.

DECLARATION

I, Christian Kameni Boumenou, s215099168, hereby declare that this MSc dissertation is my own work and has not previously been submitted for assessment or completion of any postgraduate qualification to another University or for another qualification.

Christian Kameni Boumenou

Abstract

In this dissertation, cross-sectional potential imaging of GaAs-based homoepitaxial, heteroepitaxial and quantum well structures, all grown by atmospheric pressure Metal-organic Vapor Phase Epitaxy (MOVPE) is investigated. Kelvin probe force microscopy (KPFM), using amplitude modulation (AM) and frequency modulation (FM) modes in air and at room temperature, is used for the potential imaging.

Studies performed on *n-type* GaAs homoepitaxial structures have shown two different potential profiles, related to the difference in electron density between the semi-insulating (SI) substrate and the epilayers. It is shown that the contact potential difference (CPD) between the tip and sample is higher on the semi-insulating substrate side than on the *n-type* epilayer side. This change in CPD across the interface has been explained by means of energy band diagrams indicating the relative Fermi level positions. In addition, it has also been found that the CPD across the interface increases with electron density. This result is in qualitative agreement with theory.

In addition, as known from literature, even under ambient conditions FM mode KPFM provides better lateral resolution and more realistic CPD values than AM mode KPFM. Compared to the case of AM mode analysis, where the experimental CPD values were on average $\sim 25\%$ of the theoretical values, the CPD values from FM mode analysis are on average $\sim 35\%$ of the theoretical ones. Furthermore, by using FM mode, the transition across the interface is sharper and the surface potential flattens/saturates as expected when scanning sufficiently far away from the junction. The non-neutral space charge region of the sample with an electron density of $\sim 6.7 \times 10^{18} cm^{-3}$ for example, is $\sim 0.6\,\mu m$ as measured by FM-KPFM, whereas for AM-KPFM, the width is even more than $3\,\mu m$ and the potential profiles do not saturate.

For the *p-type* GaAs homoepitaxial structures, FM mode measurements from a sample with a dopant density of $\sim 1.79 \times 10^{19} cm^{-3}$ are presented. As in the case of *n-type* GaAs, a similar potential profile showing two main domains has been obtained. However, unlike the case of *n-type* GaAs where the potential measured on the epilayer side is higher than that on the substrate side, the potential on the epilayer side of the junction is lower in this case due to the fact that the Fermi level of *p-type* GaAs is below that of the substrate.

The heteroepitaxial structures include *n-type* InGaAs grown on SI-GaAs and a 10-period GaAs/AlGaAs quantum well structure, also grown on SI-GaAs. In the case of *n-type* InGaAs/SI-GaAs structures, the potential profile resembles that of *n-type* homoepitaxial GaAs. By using the FM measurement mode, a non-neutral space charge region with a width of $\sim 0.38\ \mu m$ is obtained, while for AM mode measurements the non-neutral space charge region width is more than $3\ \mu m$; again, the potential does not saturate in the latter case. The topography image of the GaAs/AlGaAs quantum well structure clearly shows the 10 GaAs quantum wells embedded in the AlGaAs matrix. This feature is attributed to oxidation of the AlGaAs surfaces following cleaving. However, no CPD was measured across the interface. This is speculatively attributed to a combination of the tip radius and the relatively low AlAs mole fraction (0.35 in this case) in the AlGaAs matrix.

List of publications

C. **Kameni Boumenou, Z. N. Urgressa, S. R. Tankio Djiokap, J. R. Botha and J. Nel,** Effect of dopant density on contact potential difference across n-type GaAs homojunctions using Kelvin Probe Force Microscopy, Physica B Condens Matter (*In Press*).

C. **Kameni Boumenou, Z. N. Urgressa, S. R. Tankio Djiokap and J. R. Botha,** Kelvin Probe Force Microscopy on GaAs based semiconductor structures, (*In Progress*).

S. R. Tankio Djiokap, Z. N. Urgressa, C. Kameni Boumenou and J. R. Botha, Influence of a NiO intermediate layer on the properties of ZnO on Si grown by chemical bath deposition, Physica B Condens Matter (*in press*).

CONTENTS

Table of Contents

List of Figures……………………………………………………………………..i

List of tables………………………………………………………………………iv

Abbreviations……………………………………………………………………...iv

Chapter 1: Introduction…………………………………………………………1

Chapter 2: Scanning Probe Microscopy……………………………………………...4

2.1 Scanning tunneling microscopy (STM)………………………………………..4

2.2 Atomic force microscopy (AFM)…………………………………………...6

2.2.1 Basic modes of atomic force microscopy………………………………………9

Chapter 3: Kelvin Probe Force Microscopy (KPFM)………………………………14

3.1 Tapping mode atomic force microscopy (TM-AFM): practical considerations 14

3.2 Electrostatic properties of *n+/*SI -GaAs junction...19

3.3 Contact potential difference (CPD)..25

3.3.1 Overview and theory 25

a) Theoretical aspects of CPD at a semiconducting homojunction 28

b) Theoretical aspects of CPD at a semiconducting heterojunction.........................33

3.4 Amplitude modulation (AM)-KPFM 37

3.4.1 Theory...37

3.4.2 AM-KPFM set-up details 40

3.5 Frequency modulation (FM)-KPFM 41

3.5.1 Theory...41

3.6 Limitations of AM- and FM- KPFM...44

Chapter 4: Experimental Details………………………………………………..47

4.1 Sample growth characteristics...47

4.2 Instrumentation..47

4.3 Analysis conditions and probe properties 48

4.4 Sample preparation..49

Chapter 5: Results and Discussion…………………………………………………...50

5.1 CPD of *n*-GaAs/SI-GaAs and n-InGaAs/SI-GaAs using KPFM 50

5.1.1 CPD of *n*-GaAs/SI-GaAs using AM-KPFM 50

5.1.2 CPD of *n*-GaAs/SI-GaAs using FM-KPFM..58

5.1.3 CPD measurement of *n*-InGaAs/SI-GaAs using AM- and FM-KPFM.............64

5.2 CPD measurement of *p*-GaAs/SI-GaAs using FM-KPFM 65

5.3 CPD measurement of 10 period GaAs/AlGaAs quantum well structure…………...66

Chapter 6: Conclusions and outlook…………………………………………………69

References……………………………………………………………………………71

List of Figures

Figure 2.1: Operation principle of an STM: a) the bias $\boldsymbol{V}$ is applied between the tip and sample; b) the magnitude of the tunneling current $\boldsymbol{I}$ is measured as a function of position on the surface……………………………………………………………………..……………5
Figure 2.2: Schematic view of a STM set-up [29]……………………………………………...6
Figure2.3: Schematic of an AFM setup [23] ……………………………………………………7
Figure 2.4 Graphical representation of the Van Der Waals curve versus tip-sample distance and the regime for different modes of performing AFM analysis (red boxes) [38] ………..………8
Figure 2.5: Cantilever amplitude change during tapping mode measurements: a) cantilever oscillating freely in air, which means the tip is far from the sample surface; b) cantilever oscillating at lower amplitude because of damping [41]……….……………………………..10
Figure 2.6: Schematic depiction of non-contact mode AFM: (a) amplitude modulation mode and (b) frequency modulation mode. Both AM and FM modes maintain a constant tip-sample separation. AM mode uses the oscillation amplitude changes as a feedback signal while FM uses the oscillation frequency changes as feedback signal [21] ...……………………………………13
Figure 3.1: Schematic depiction of how the TM-AFM set-up adjusts the change in amplitude, attempting to match the amplitude setpoint. (a) adjustment process; (b) topography image of the sample surface……………………………………………………………………………15
Figure 3.2: Schematic representation of tapping mode AFM………..……………………16
Figure 3.3: Schematic representation showing (a) tip in contact with the sample during the height measurement and (b) tip lifted to a constant height during the CPD measurement in AM-KPFM. $\boldsymbol{V_{dc}}$ is the reverse *dc* voltage applied to compensate the CPD between the tip and the sample and the *ac* voltage $\boldsymbol{V_{ac}\sin(w_{ac}t)}$ is applied to electrically excite the cantilever [56] ..……………17
Figure 3.4: Typical cantilever tune panel for AM-KPFM. The main parameters include the drive amplitude, amplitude setpoint and drive frequency. The top curve is amplitude vs frequency, whereas the bottom curve is phase vs frequency…………………………………..…………19
Figure 3.5: Numerically simulated potential and carrier density profiles for forward biased n^{+}/SI-GaAs junction: (a) electrostatic potential and electron and hole quasi-Fermi potentials; (b) case of electron and hole densities. Dashed lines indicate the equilibrium potential (in (a)) and electron and hole profiles (in (b)), respectively [59]……………………………..………...22
Figure 3.6**:** Shockley plot for DDSA SI-GaAs compensation. T, E_C, $\boldsymbol{E_V}$, $\boldsymbol{N_c}$, $\boldsymbol{N_v}$ and E_F are temperature**,** absolute minimum of the conduction band, absolute maximum of the valence band, density of states in the conduction band, density of states in the valence band and the Fermi level energy, respectively. $E_V = 0\ eV$**,** $E_C = 1.42\ eV$, $N_c \sim 10^{18} cm^{-3}$ and $N_V \sim 10^{18} cm^{-3}$[59] ……23
Figure 3.7: Electric field versus position. $\mathrm{N_{sa,C}} = 2 \times 10^{15}\mathrm{cm^{-3}}$, $\varepsilon = 114.22 \times 10^{-12}\ F/m$ and $\mathrm{q} = 1.6 \times 10^{-19} c$ ………………………………………..…………......................25
Figure 3.8: Theoretical principle of CPD: (a) tip and sample modeled as almost in contact; relative Fermi energy levels and work functions of the tip and sample: (b) before contact (c) after electrical contact with the CPD indicated and (d) after an external reverse *dc* voltage $\boldsymbol{V_{dc}}$ is applied [41]. Here $\emptyset_{\mathbf{s}}$ and $\emptyset_{\mathrm{t}}$ are the work functions of the sample and the tip, respectively, whereas $\boldsymbol{E_{Fs}}$ and $\boldsymbol{E_{Ft}}$ are the Fermi energies of the sample and tip, respectively……………....**26**

Figure 3.9: Energy band diagram illustrating how the CPD across the interface (junction) between two layers of a semiconductor is measured: $\boldsymbol{V_{dc}(substrate)} = \emptyset_{S_b} - \emptyset_t$ when the tip is above the substrate and $\boldsymbol{V_{dc}(layer)} = \emptyset_l - \emptyset_t$ when the tip is above the layer; $\boldsymbol{E_c}$, $\boldsymbol{E_v}$ and $\boldsymbol{E_F}$ are absolute minimum of the conduction band, absolute maximum of the valence band and the Fermi level energy, respectively……………………………………………………….….........27
Figure 3.10**:** Sketch of energy band diagram using the Anderson model for : (a) semi-insulating, (b) *n-type* non-degenerate and (c) *n-type* degenerate semiconductor materials; $\emptyset_{SI}$, $\boldsymbol{\emptyset_{nd}}$, and $\boldsymbol{\emptyset_d}$ are the work functions of the semi-insulating, *n-type* non-degenerate and degenerate semiconductors materials, respectively; E_{F_i} and χ are the intrinsic Fermi level energy and electron affinity, respectively……………………………………...……………………….......28
Figure 3.11: Fermi energy level versus electron density of n-type non-degenerate and degenerate GaAs: $\boldsymbol{N_C = 4.70 \times 10^{17}\ cm^{-3}}$, $\boldsymbol{E_c = E_g = 1.424\ eV}$, $\boldsymbol{E_v = 0\ eV}$, $\boldsymbol{T = 300\ K}$, $\boldsymbol{k = 8.62 \times 10^{-5}}$ eV/K and $\boldsymbol{E_o = 1.415eV}$, slightly below E_c has been calculated from equation (3.16) for n =N_C ……………………………………………………………..……………………….....32
Figure 3.12: Sketch of energy band diagram using the Anderson model for *n-type* InGaAs grown on GaAs substrate: (a) before contact and (b) after contact. $\boldsymbol{E_c}$, $\boldsymbol{E_v}$, $\emptyset$, $\boldsymbol{\chi}$, $\boldsymbol{E_{F.}}$ $\Delta\boldsymbol{E_v}$, $\Delta\boldsymbol{E_c}$ and $\boldsymbol{V_{CPD}}$ are the absolute minimum of the conduction band, absolute maximum of the valence band, work function, electron affinity, Fermi energy, band offsets and contact potential difference, also called the built-in potential, respectively. $\boldsymbol{V}$ is used in the derivation of the CPD……………..…...34
Figure 3.13: Linear interpolation scheme for the effective masses versus mole fraction *x* in $\mathbf{In_xGa_{(1-x)}As}$. The red solid line represents the evolution of the effective mass of holes as a function of mole fraction of InAs; and the black line is that of the effective mass of the electron...35
Figure 3.14: Tip-sample modelling: (a) real situation; (b) ideal situation; $\Delta\boldsymbol{V}$ is voltage difference. Here, it is assumed that the work function of the tip is lower than that of sample and $\boldsymbol{z}$ is the tip-sample distance…………………………………………………………..…………..37
Figure 3.15: Block diagram of an AM-KPFM setup [40] …………………………...………40
Figure 3.16: The variation in oscillation frequency of the cantilever relative to its natural resonance frequency is determined by the nature of the interaction between the tip and sample [41] ………………………………………………………………………………………..….42
Figure 3.17: (a) SCM-PIT probe modeling with the following nominal probe geometries: $225\ \mu m$ length (L), $30\ \mu m$ width (W), tip $10\ \mu m$ tall (H), and having a cone half angle θ of 22.5^o; (b) the contribution of the tip cone integrated to a height h over total electric force (blue) and electric force gradient (purple) are plotted versus height (h). The "blue" plots are the electric force for tip-sample separations of $5\ nm$ and $50\ nm$. The "purple" plots are electric force gradients for the same tip-sample separations [71] …………………….….………………45
Figure 4.1: Image of Bruker Dimension Icon System…………………………...……………48
Figure 4.2: SEM image of the SCM-PIT probe downloaded from the Bruker website [74] ………………………………………..……………………………………………………….49
Figure 4.3: (a) Sketch of a cross-section of a sample consisting of a substrate and a single epilayer. (b) Cross-sectional sample mounted onto the sample holder. The tip scans across the interface……………………………………………………………………………………..49
Figure 5.1: Cross-sectional (a) topography and (b) potential images of $3\ \mu m$ thick *n-type* degenerate GaAs on SI-GaAs substrate, using AM-KPFM. The two images were taken at

different regions along the interface of the same sample. The red curves on the topography and potential images, respectively, are the average height and potential across the two different layers. The scan size was 6 $\mu m \times 4\ \mu m$ ……………………………………………..………51
Figure 5.2: Potential versus position of sample 4, repeated four times, at the same spot and with the same parameters……………………………………………………………………….......52
Figure 5.3: Cross-sectional (a) topography and (b) potential maps of 3 μm thick *n-type* degenerate GaAs grown on SI-GaAs substrate, using AM-KPFM. Four samples with the same layer thickness, but with different electron densities have been investigated. The red curves on the topography and potential images are the average scans lines, which indicate the shape of the topography and potential across the two different layers. The scan size was $6\ \mu m \times 4\ \mu m$ ……………………………………………………………………………………………53
Figure 5.4: Average potential versus position for samples 1-4, obtained by using AM-KPFM……………………………………………………………………………………54
Figure 5.5: Experimental evolution of the CPD across *n-type* GaAs/SI-GaAs versus electron density, using AM-KPFM. Vertical lines are the estimated uncertainties. Four samples with difference electron densities have been used for the investigation…………………..……….55
Figure 5.6: Schematic energy band diagrams for ideal semi-insulating and *n-type* GaAs. (a) Before contact, (b) after contact. $\emptyset_{d_{GaAs}}$, **and** $\emptyset_{SI}$ are the work functions of *n-type* degenerate GaAs and SI-GaAs, respectively; E_{F_i} and E_F are the intrinsic Fermi level energy and the Fermi level of *n-type* degenerate GaAs; E_c and E_v are the absolute minimum of the conduction band and absolute maximum of the valence band and χ_{GaAs} is the electron affinity………………....56
Figure 5.7: Theoretical evolution of the CPD across the *n-type* GaAs/SI-GaAs interface versus electron density……………………………………………………………………………..57
Figure 5.8: FM-KPFM scans of cross-sections of samples 1-4: (a) topography and (b) potential. Four GaAs/SI-GaAs samples with same the layer thicknesses (~3 μm), but with different electron densities have been investigated. The red curves on the topography and potential images, respectively, are the average scan lines, which indicate the shape of the topography and potential across the two different layers. The scan size was 6 $\mu m \times 4\ \mu m$……………………..59
Figure 5.9: AM versus FM mode KPFM: (a) average potential line and (b) Electrostatic field of the sample with the highest dopant density (sample 4). The electrostatic field has been calculated by taking the first derivative of the potential profile. A sharper transition is obtained with FM mode than AM-KPFM mode…………………………………………...…………………..61
Figure 5.10: Potential versus position for samples with different dopant density, using FM-KPFM method. The potential along the substrate side is adjusted to the same value……..……62
Figure 5.11: Experimental evolution of the CPD across *n*-GaAs/SI-GaAs versus electron density, using FM-KPFM method. The line is a guide to the eye……………………..………………63
Figure 5.12: Cross-sectional (a) topography and (b) potential images of $\mathbf{5\ \mu m}$ thick *n-type* $\mathbf{In_{0.17}Ga_{0.83}As}$ single layers grown on SI-GaAs, using both AM and FM mode KPFM. The upper part (potential and topography, respectively) has been recorded with FM mode KPFM and the lower part with AM mode KPFM. Average scan lines for topography and potential profiles are depicted in (c) and (d), respectively. A larger contrast and a sharper transition are obtained with FM mode than with AM mode KPFM……………………………..…………………64
Figure 5.13: Cross-sectional (a) topography and (b) potential images of a $\mathbf{4.8\ \mu m}$ *p-type* GaAs single layer grown on semi-insulating GaAs, obtained using FM-KPFM. Average scan lines for topography and potential profiles are depicted in (c) and (d), respectively………………..……65

Figure 5.14: Schematic representation of GaAs/AlGaAs multiple quantum wells used for measurements……………………………………………………………………………………66
Figure 5.15: Cross-sectional (a,b) topography and (c,d) potential images of GaAs/AlGaAs heterostructure, obtained using both AM and FM mode KPFM. The left-hand side (potential and topography, respectively) has been recorded with AM mode KPFM and the right-hand side with FM mode………………………………………………………………………………………....67

List of tables

Table 3.1: Coefficients A, B and C describing band gap narrowing in n-GaAs………………....31
Table 4.1 Growth conditions of samples used in this study……………………..………………47

Abbreviations

AFM	-	Atomic force microscopy
AM-AFM	-	Amplitude modulation atomic force microscopy
AM-KPFM	-	Amplitude modulation kelvin probe force microscopy
BT	-	Bipolar transistors
C-AFM	-	Conductive atomic force microscopy
CM	-	Contact mode
CPD	-	Contact potential difference
EFM	-	Electric force microscopy
FM-AFM	-	Frequency modulation atomic force microscopy
FM-KPFM	-	Frequency modulation kelvin probe force microscopy
KPFM	-	Kelvin Probe Force Microscopy
LEDs	-	Light emitting diode
MBE	-	Molecular beam epitaxy
MOCVD	-	Metal-organic chemical vapor deposition
MOVPE	-	Metal-organic vapor phase epitaxy
NCM	-	Non-contact mode
NMMU	-	Nelson Mandela Metropolitan University
PC-AFM	-	Photoconductive atomic force microscopy
QH	-	Quantum heterostructures
SEM	-	Scanning electron microscopy
SI	-	Semi-insulating
SPM	-	Scanning probe microscopy
STM	-	Scanning tunneling microscopy
TM	-	Tapping mode
V_{dc}	-	Reverse *dc* applied voltage
VDW	-	Van der waals

Chapter 1: Introduction

Recent advances in epitaxial growth of semiconductors have generated novel quantum heterostructures (QH) such as quantum wells, quantum dots and quantum wires [1, 2]. In particular, the advancement of gallium based III-V compound semiconductors, with excellent optical and electrical properties, has greatly changed semiconductor technology. Gallium arsenide (GaAs), for example possesses a direct [3] and moderate band gap (around $1.4\ eV$ at room temperature [4]). In addition, it has a high saturated electron velocity and electron mobility [5], and operates in the infrared region [6]. As in the case of most III-V compound semiconductors, it can also be grown with almost defect-free heterointerfaces [7]. Furthermore, as undoped GaAs is highly resistive to electrical current [8], it is often used as a substrate material for the epitaxial growth of other III-V semiconductors [5]. Due to these properties, several of the GaAs based III-V compound semiconductors have proven to be promising candidates for short wavelength emitters and detectors, and higher temperature power electronic devices [9]. As a result, many novel semiconductor devices such as bipolar transistors (BT), double heterojunction lasers, and high-electron-mobility transistors have been produced from these compounds [10]. In addition, devices made of these compounds are used in different communication devices such as smart phones and laptops, and in wireless and optical communication systems [7, 11]. This multitude of applications makes it hard to imagine what our lives would be like without these devices. Besides, intensive efforts still exist all over the world to create novel devices from different heterostructures of these compounds.

In principle, III-V semiconductor based heterostructures are produced by growing several dissimilar III-V compound semiconductors on top of one another. Among the best known heterostructures made of these compounds are AlAs/GaAs [12], AlGaAs/GaAs [13], InGaAs/GaAs [13], InGaAs/AlGaAs/GaAs [14] and the like. Different methods have been used to grow these heterostructures. These include Metalorganic chemical vapor deposition (MOCVD) [15] and molecular beam epitaxy (MBE) [16]. MOCVD, which is a technique widely used in our research group (NMMU), is a technology that can be used to deposit very thin layers onto a semiconductor substrate. It is used in manufacturing light emitting diode (LEDs), lasers, transistors, solar cells and others electronic and optoelectronic devices, and is nowadays the key

enabling technology for future markets with high growth potential [17]. It appears as the most powerful growth technique for III-V compound semiconductor manufacturing. Even though growth of semiconductor heterojunctions using these techniques (MOCVD and MBE) are well stablished, detailed studies of the charge transport mechanisms and the effect of surfaces and interfaces in devices made from these semiconductors are ongoing [18]. More explicitly, charge transfer between the layer and substrate, and across semiconductor interfaces (heterojunctions) need to be controlled and understood. This is mostly because the performance of QH-based devices depends directly on interface defects, the charge distribution at the junction and the atomic composition [11]. Information regarding these defects and understanding the quality of a junction can be obtained by measuring the work function or contact potential difference (CPD) of the QH as pointed out by T. Glatzel *et al.* [19] and Y. Wu *et al.* [20].

It is known that the work function of a given material is defined as the minimum energy needed to remove an electron from the Fermi-level to a point immediately outside the solid surface, in vacuum. It appears as one of the most fundamental properties of a semiconductor material, although it is highly sensitive to the surface of the material. Any change to the surface by contamination (chemical or physical) can strongly affect its work function [21]. For these reasons, exact measurements of the CPD or work function with high lateral resolution is one of the most important challenges in the surface characterization of semiconductors or semiconductor heterojunctions used in advanced devices [22]. Hence, the main motivations of this dissertation is to experimentally measure the CPD of some gallium based III-V semiconductor structures grown by MOCVD and to show how these values change with electron density, using kelvin probe force microscopy (KPFM).

To carry out these investigations, the remainder of this dissertation is divided into five chapters: As a broad outline, chapter 2 of the dissertation deals with a background study of scanning probe microscopy (SPM), while the detailed theory and set-up of KPFM are presented in chapter 3. Some limitations associated with KPFM technique are also presented in this chapter. Chapter 4 gives a brief description of the experimental method for growing the samples and of the characterization techniques employed. In addition, it summarizes the characteristics of different probes used, describes the SPM system and sample preparation procedures. The results and

discussion are presented in chapter 5, while chapter 6 summarizes the results of this work and provides suggestions for future work in this field.

Chapter 2: Scanning Probe Microscopy

Scanning probe microscopy (SPM) refers to a family of techniques that measures the properties of materials on the nano-scale, using a very sharp tip close to or in direct contact with the surface of the sample [23]. It is derived from scanning tunneling microscopy (STM) and atomic force microscopy (AFM). In principle, SPM can be used to study the topography, the morphology, surface mechanical and electrical properties of several types of structures, such as thin films, nanostructures, semiconductor homojunctions, heterojunctions and metal-semiconductor junctions. It can also be used to image the topography and morphology of softer materials like polymers and biological samples. In this chapter, an overview of these SPM techniques widely used in nanotechnology is highlighted. As the working principle of SPM is derived from that of STM and AFM, basic understanding and the working principle of a STM and AFM is first presented. Following this, different modes of AFM are highlighted. Finally, an introduction to the kelvin probe force Microscopy (KPFM) method, which is used to measure CPD, is introduced.

2.1 Scanning tunneling microscopy (STM)

STM was invented in 1981 by Gerd Bining and Heinrich Rohrer [24] at IBM Research Laboratory in Switzerland. They were awarded the Nobel Prize in Physics in 1986 for their invention. It is the first instrument that allowed scientists to study both topographical (with atomic resolution of order $\mathbf{0.1}\ \boldsymbol{nm}$ [25]) and electrical properties of materials. Surface imaging by STM is obtained by mechanically moving a very sharp conducting tip in a raster, scanning line by line, and recording the tip-surface interaction as a function of position. Figure 2.1 illustrates this phenomenon. The basic concept of STM is essentially focused on the quantum tunneling effect, a phenomenon where a particle (electron) tunnels through a barrier (air in this case) between the STM tip and the specimen. As the conduction between the tip and the specimen is distance dependent and surface sensitive, this instrument is widely used in applications involving surface investigations. It provides a $\boldsymbol{2D}$ real topographical image and can also be used to measure some of electrical properties of conducting materials.

The basic principle involves bringing a tip very close (approximately 1 nm) to the sample surface and recording the tunneling current between the tip and sample as a function of position [26].

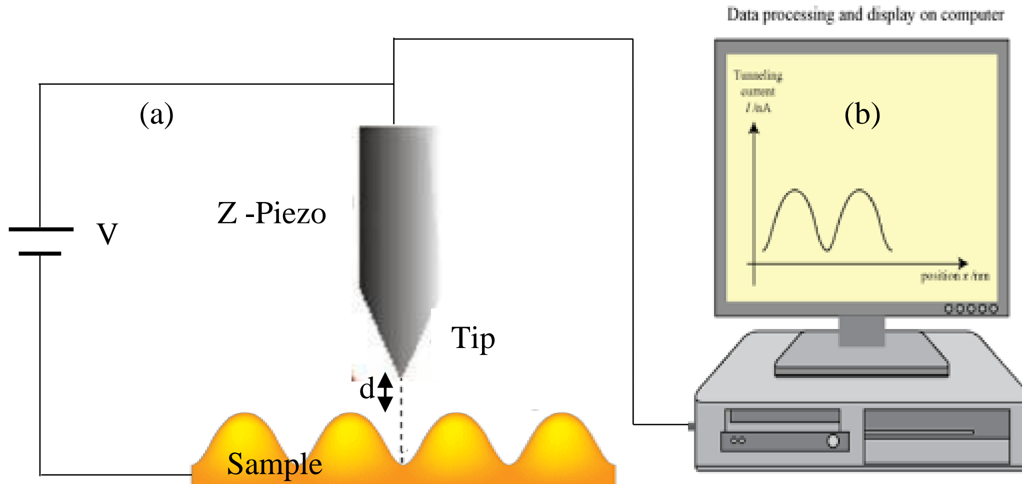

Figure 2.1: Operation principle of an STM: a) the bias $\boldsymbol{V}$ is applied between the tip and sample; b) the magnitude of the tunneling current $\boldsymbol{I}$ is measured as a function of position on the surface [27].

In this configuration (Figure 2.1 (a)), if a small dc voltage V is applied between the tip and the sample, an electric current can be detected due to the tunneling of electrons through the air gap. The direction of the flow of the current is determined by the difference in the Fermi level of the tip and the sample. The magnitude of the current strongly depends on the distance between the tip and the sample. It also depends on the morphology of the sample surface. Mathematically it is given as [28]:

$$I \approx Ve^{-(\alpha d)} \qquad 2.1$$

where I is the tunneling current, d is the tip-sample distance and α a constant. This clearly shows the exponential variation of the tunneling current with tip-sample distance, where an increase in d results in a decrease in current, or vice-versa. Hence, by scanning at a constant d the change in current can be measured and translated into topographical information of the sample surface, as shown in Figure. 2.1 (b). The schematic graph in Figure 2.1 (b) illustrates the variation in current when the tip scans across the surface at constant distance d. As indicated in this graph, the current varies exactly the same as the height profile of the surface. Consequently, the real-space

image of the sample surface can be deduced simply by measurement of the variation of the tunneling current. For its technical implementation, STM employs many components, such as a scanning tip, a piezoelectric controlled scanner, a distance controling unit, a vibration isolation system, and a computer (Figure 2.2). In this case, the tip is used to probe the sample surface, the piezoelectric material controls the plane position (x, y) and the height z of the tip, and a distance controling unit brings the tip closer to the sample. A vibration isolation system and computer meanwhile are used to isolate the measurement from any external vibrations and to record the tunneling current variation for topographical imaging, respectively.

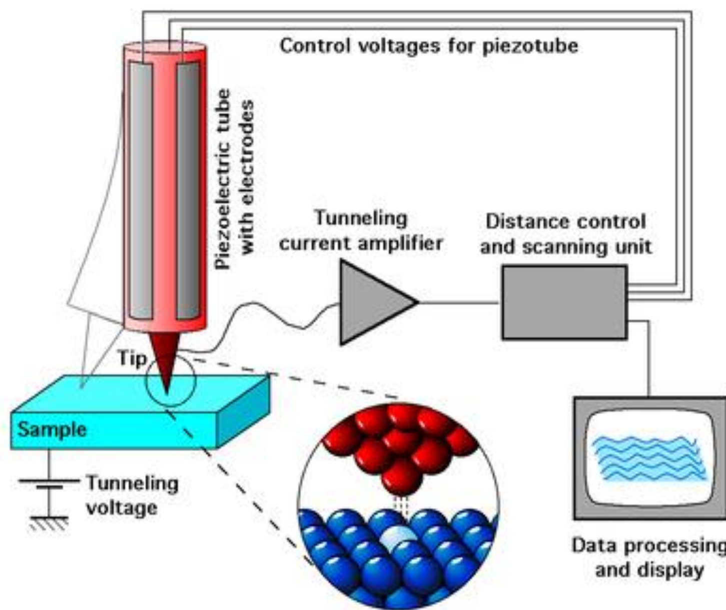

Figure 2.2: Schematic view of a STM set-up [29].

In general, as a basic tool for surface characterization, and with all its applications in air, ultra-high vacuum, water and various other liquid or gas ambient, STM has revolutionized surface science. However, like any other measurement techniques, it also has some limitations. It does not work on insulators [30], and basically is used for very flat surface topography imaging [31]. It is also complicated to quantify the height variations of the sample surface using STM. This limits the application of STM. As a result, it led to the introduction of atomic force microscopy (AFM) in 1986 [32].

2.2 Atomic force microscopy (AFM)

Unlike STM which is based on the tunneling current between the conducting tip and specimen, AFM is based on the force between the tip and the sample. Its principle can be described as follows. As can be seen in the Figure 2.3, AFM probes the surface of a sample by using a very sharp tip with a diameter on the order of $10 - 50\ nm$ [33]. The tip, located at the free end of a micrometer-scale cantilever, interacts with the sample. Light from a laser diode is reflected off the back side of the cantilever, and is sent through different optics onto a photo-detector [23]. As the tip interacts with the sample surface, the interaction forces between them cause the cantilever to deflect. The photo diode measures the cantilever deflection as the tip is scanned over the sample, or the sample (stage) is scanned under the tip. The measured cantilever deflections are thereafter converted, electronically, into an image of the scanned surface.

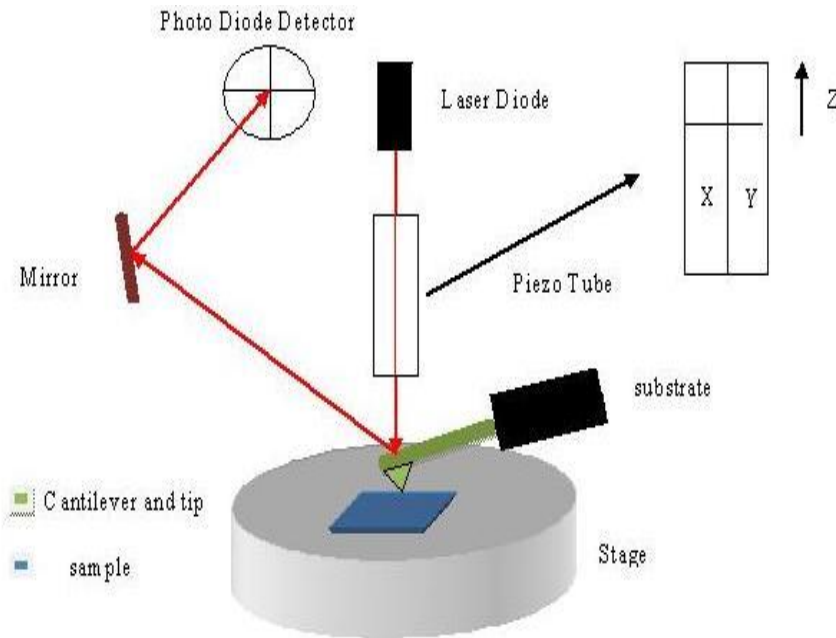

Figure 2.3: Schematic of an AFM setup [23]

The forces that contribute to the deflection of an AFM cantilever are numerous and come from various origins. Depending on the tip-sample separation, they can be long range forces such as Van Der Waals (VDW) and electrostatic forces, or short range forces (chemical forces) [34]. Many literature sources emphasize that these forces between the tip and sample depend on the nature of the sample, and the type and geometry of the probe (*i.e.* the tip) [35, 36]. In an AFM setup, these interaction forces are controlled by a piezo-tube. The piezo-tube is a material which

can expand or contract under an applied voltage. In Figure 2.3, the piezo material to which a bias voltage is applied by a feedback loop, is connected indirectly to the cantilever. This indirect connection is for controlling the horizontal position (x, y) and the height z of the scanning tip. Therefore, the piezo material is used to control the contact between the tip and sample. Otherwise, the piezo can also be connected to the stage. In this case, the tip stays motionless and all movements, namely up and down and horizontally, are done by the stage. The AFM system used for measurements in this study employs the first set-up, where the piezo electric ceramic material [23] is connected to the cantilever or to the tip.

As mentioned in the previous paragraph, several forces typically contribute to the deflection of an AFM cantilever. However, the force most commonly associated with atomic force microscopy is an interatomic force called the Van der Waals force [37]. Figure 2.4 shows the dependence of the Van Der Waals force upon the tip-sample separation.

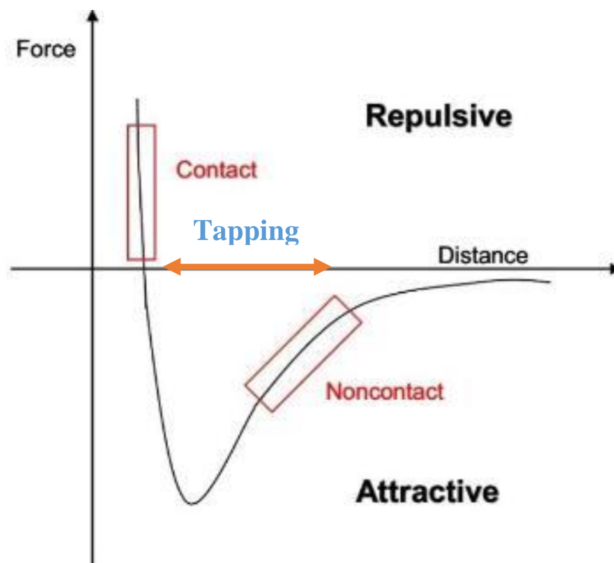

Figure 2.4: Graphical representation of the Van Der Waals curve versus tip-sample distance and the regime for different modes of performing AFM analysis (red boxes) [38].

Depending on the tip-sample separation, the VDW force curve is divided in two main regimes: contact regime and non-contact regime. In the contact regime, the tip-sample distance is less than $1\ nm$ [34], and the interatomic force between them is repulsive. In the non-contact regime, the tip-sample distance is on the order of a few nanometer and higher [34], and the interatomic force between them is attractive. The intermittent-contact mode, commonly called tapping mode in

AFM technical language, is therefore between these two regimes. Based on the mode of contact, AFM, which had the objective of overcoming the limitations of STM *i.e.* to measure the $3D$ surface topography of the material and to provide surface properties of materials that could not be studied by STM, adopted three mains approaches to perform its measurements.

2.2.1 Basic modes of atomic force microscopy

The three basic operating modes of an AFM system are contact mode (CM), non-contact mode (NCM) and tapping mode (TM).

In CM-AFM, a tip with a spring constant less than $1\ N/m$ [23] and the sample are in perpetual contact during the scan. The interaction force as shown in Figure 2.4 between them is repulsive. This repulsive force between the tip and sample causes the cantilever to bend during the scanning. Thus, by maintaining a constant distance or force between the tip and sample, and measuring the change in height of the cantilever deflection, a topography of the sample surface can be obtained.

As the tip is always maintained in contact with a sample during CM-AFM measurements, the probability to break it or to damage the sample is higher. This limitation of CM-AFM led to the introduction of the other two contact modes, namely NC-AFM (first) and thereafter TM-AFM. Except for the fact that the tip does not touch the surface, the working principle for NC-AFM is the same as the case of TM-AFM. The two modes operate using a vibrating mechanical cantilever, and have the same modeling equation.

In TM-AFM, which is the mode employed for the CPD measurements in the current project, the tip is held close to the sample surface, oscillating at or near its fundamental resonance frequency [39], and touches the sample at regular intervals. The oscillation of the tip is generated by the piezoelectric tube on which the cantilever-tip is mounted. Due to the interaction forces, which exist between the tip and sample, when the tip approaches the sample surface, the oscillation amplitude is damped. This change in amplitude can be measured and used as feedback signal for surface topographic imaging. In fact, in TM-AFM, a feedback loop monitors the amplitude of the oscillation of the tip. The measured amplitude is compared to the value defined by the amplitude setpoint parameter. When the tip encounters a change in height because of the change

in the surface morphology of the sample, its amplitude changes compared to the setpoint. The feedback loop adjusts the tip-position by moving the z-piezo until the amplitude matches the setpoint. This vertical movement of the z-piezo is recorded as the height profile of the sample. Figure 2.5 shows schematically the AFM cantilever in air (non-interacting) and at the sample surface, during TM-AFM measurements.

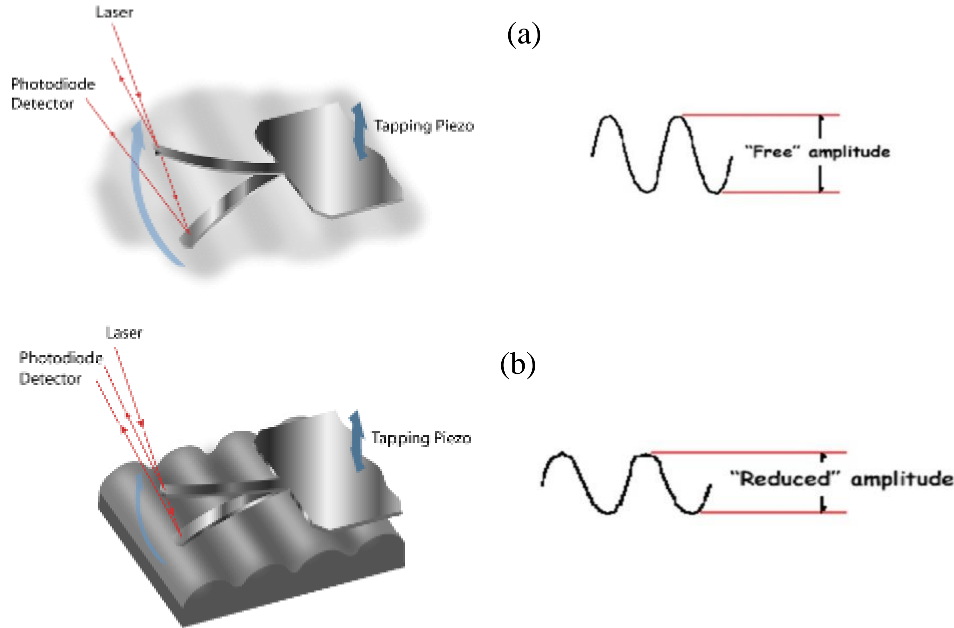

Figure 2.5: Cantilever amplitude change during tapping mode measurements: a) cantilever oscillating freely in air, which means the tip is far from the sample surface; b) cantilever oscillating at lower amplitude because of damping [40].

In NCM-AFM (also called dynamic mode), the cantilever supporting a sharp tip at its end also oscillates at or near its resonant frequency. The change in the oscillation, which obviously depends on the tip-sample interaction, is measured as in the case of TM-AFM method [41]. By considering the whole cantilever-tip as a point mass-linear spring system with a damping and a driving excitation**,** the equation of motion for the tip is written as [42]:

$$m\ddot{z} + \frac{mw_0}{Q}\dot{z} + Kz = F_{ts} + F_0\cos(w_d t) \qquad 2.2$$

where m is the mass of the cantilever, z the tip-sample distance, K is spring constant, Q the quality factor, w_0 the angular resonance frequency, F_{ts} the tip-sample interaction, F_0 and w_d the

amplitude and angular frequency of the driving force, respectively. Depending on the tip-sample interaction force F_{ts}, when the tip approaches the sample surface the oscillation amplitude is damped and the resonance frequency can also shift. These changes can be measured and used as feedback signals to image a real-space profile of the sample surface. Recent further developments of AFM have resulted in several other techniques used for probing the electrical properties of surfaces on the nanometer scale. The development of these new techniques is mostly motivated by shrinking dimensions of semiconductor materials recently achieved [43]. These new semiconductor structures with nanometer-sizes exhibit novel electrical/physical properties which need to be characterized or measured. Among these techniques, the following can be enumerated: conductive atomic force microscopy (C-AFM) [44], photoconductive atomic force microscopy (PC-AFM) [45], electric force microscopy (EFM) [46], and finally kelvin probe force microscopy (KPFM) [47].

The C-AFM technique developed in the 1990's was especially focused on determining the local electrical properties of insulating materials like SiO_2 thin films on the nanometer scale [48]. It has recently been used to investigate the effect of atomic hydrogen and step orientation on the growth behavior of InAs on misoriented GaAs (110) substrate [49]. Except for the fact that it provides simultaneously the surface topography and the current between the tip and the sample, this measurement technique is similar to STM. In fact, it combines CM-AFM and STM to execute the measurements.

PC-AFM is a method which provides the photoelectric properties of matter through its interaction with light on a nanometer scale. This technique has been used for investigating the photoelectric properties of organic thin films [50]. Its principle consists of measuring the photocurrent in an individual nanometer-scaled structure and also to image the photoelectric properties by scanning a conductive cantilever over the surface of a sample.

EFM is a technique that can be used to measure variations in electric field gradient of the surface of a sample [40]. The sample may be conducting, semiconducting or insulating. It typically employs NCM-AFM or TM-AFM with a sharp conductive tip as the basic technique to perform the measurements. However, J. W. Hong *et al*. [46] have proved that the CM-AFM technique can also be used for EFM measurements. They used it to detect the surface charge density and

the anisotropic domain wall thickness of a triglycine sulfate crystal [46]. Otherwise, EFM has been used to image surface charge [51] and dopant properties of semiconductors [52]. EFM has also been used to image the local voltage of working microelectronic structures [53], to measure local electrostatic forces [54] and charge on insulators [55].

KPFM, meanwhile, is used to measure the contact potential difference (CPD) between a sharp conducting tip and the sample. The CPD is the difference between the work function of the sample and the work function of the tip [56]. Introduced for the first time in 1991 by Nonnenmacher *et al*. [47], KPFM allows imaging simultaneously the topographic and the surface electrical properties of materials on the nano-scale. It appears nowadays as the most powerful tool, able to provide simultaneously the topography ($\sim 1\ nm$ in x-y plane and $\sim 0.1\ nm$ in the z direction) [56] and images of the surface potential distribution with sub-nanometer (under vacuum) resolution [21]. It has been used to characterize the nano-scale electronic/electrical properties of metal/semiconductor surfaces and many other semiconductor devices [49]. Recently, it has been used to characterize the electrical properties of semiconductor surfaces and many other semiconductor nanostructures. In the same way, electronic properties of defects on clean semiconductor surfaces have been explored. In light of all the opportunities offered by KPFM, it is at present the best technique used in the characterization of the electrical properties of nanostructures [21]. Hence, an investigation of the CPD of some III-V semiconductor heterostuctures grown by MOCVD, which is available in our research group, using KPFM is the goal of this project.

As pointed out above, KPFM is a technique that can be used to map the surface potential and topography of the sample. This mapping of the surface potential is usually carried out through two basic techniques: amplitude modulation AM-AFM and frequency modulation FM-AFM. In AM-AFM, the change in amplitude as a result of tip-sample interaction is measured; whereas in FM-AFM the change in oscillation frequency of the tip is measured. Figure 2.6 below is a schematic representation of AM-AFM and FM-AFM operation [21].

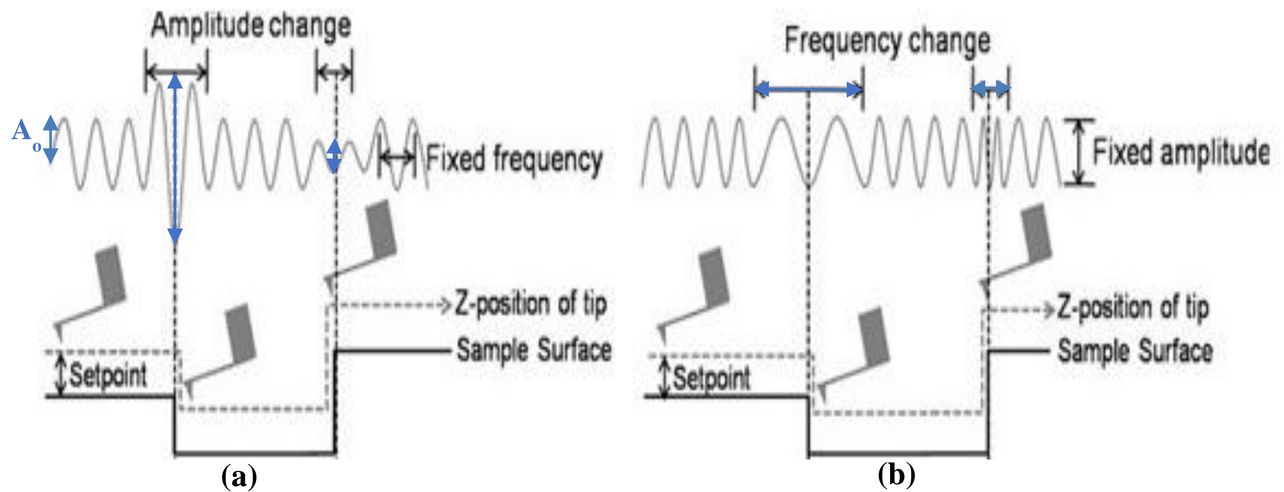

Figure 2.6: Schematic depiction of non-contact mode AFM: (a) amplitude modulation mode and (b) frequency modulation mode. Both AM and FM modes maintain a constant tip-sample separation. AM mode uses the oscillation amplitude changes as a feedback signal while FM uses the oscillation frequency changes as feedback signal [21].

As can be seen in Figure 2.6 (a), when the tip is around the flat area of the sample (left side of Figure 2.6 (a)) the amplitude of the oscillation is A_o. As the tip moves to the right where the sample surface is lower, the tip sample distance will increase, causing the interaction force to decrease and resulting in an increased oscillation amplitude of the cantilever (*i.e.* beyond the amplitude setpoint). This change in amplitude due to the decreased tip-sample interaction is monitored and adjusted by a feedback loop to adjust the tip-sample distance to its original value (*i.e*. to a pre-determined setpoint [21]). In FM-AFM mode, changes in the oscillation frequency provide information about the tip-sample interactions. The cantilever oscillation frequency changes due to tip-sample distance variations, as illustrated in Figure 2.6 (b). As in the case of AM-AFM, in FM-AFM the feedback loop adjusts the frequency to attain the setpoint frequency. The amplitude or frequency setpoint is one of the key parameters used in dynamic mode (TM and NCM) AFM. It depends on the cantilever properties and is automatically set by the system during tuning. However, it can also be adjusted by the user to improve the accuracy of the results [40]. Details of the theoretical and operating principles of AM- and FM-KPFM are described in the following chapter.

Chapter 3: Kelvin Probe Force Microscopy (KPFM)

Unlike the case of AFM, where a sharp non-conducting oscillating tip is used for probing the sample, a sharp conducting tip is used in KPFM measurements. As indicated in chapter 2, the KPFM measurements are acquired by minimizing the electrostatic force between the sample and the tip [41]. There are two modes of KPFM measurements: amplitude modulation (AM)-KPFM and frequency modulation (FM)-KPFM [19, 57]. In the AM-KPFM mode, the electrostatic force between the tip and the sample is minimized, whereas in the FM-KPFM mode the electrostatic force gradient is minimized. Both these modes involve the use of standard TM-AFM [40] with an external electrostatic force superimposed across the sample and the tip. Hence, in the first part of this chapter a brief presentation of the technical implementation of TM-AFM is described. Thereafter details of electrostatic and current transport properties of *n+/*semi-insulating GaAs junctions are described. Furthermore, the theoretical working principles of CPD are presented. Finally, the theoretical and practical aspects of AM-KPFM and FM-KPFM are described and some limitations associated with both techniques are also presented.

3.1 Tapping mode atomic force microscopy (TM-AFM): practical considerations

In TM-AFM, the cantilever is mechanically excited by a piezo tube. During the scanning process, the change in amplitude is measured and used as feedback signal to provide a topographical image of the sample surface. As the theoretical working principle of this technique has been summarized in section 2.2.1, in this section the technical implementation of TM-AFM is presented.

Like any other scanning mode in AFM, the procedure for TM begins with setting up the experiment and tuning the cantilever. Tuning the cantilever is a step that consists of electrical excitation of the cantilever so that the basic physical parameters including cantilever natural frequency, spring constant and drive amplitude are captured and stored to a parameter list in the software. Proper tuning of the cantilever is essential and will be discussed shortly.

Once the cantilever physical parameters are sent to the parameter list, the software sets all the setpoints. These include the drive amplitude, amplitude set point and the drive frequency.

Amplitude setpoint: This is the initial amplitude, automatically chosen by the system and that the feedback loop will try to keep constant during scanning by adjusting the *z*-piezo.

Drive amplitude: This is the amplitude of the electric signal which drives the piezo that oscillates the cantilever.

Drive frequency: This is the frequency of the cantilever during the scanning process. To increase the sensitivity, it should be close to the resonance frequency of the cantilever.

During scanning across the sample, the TM-AFM setup tracks these parameters through the feedback loop. If the value of a measured parameter differs from the set values, the system adjusts each parameter until the difference is minimized. For example, if the measured amplitude differs from the amplitude setpoint, the feedback loop adjusts the tip-sample distance by changing the *z*-piezo position [58]. Figure 3.1 illustrates how the TM-AFM set-up measures the change in amplitude of the cantilever oscillation according to the initial amplitude setpoint.

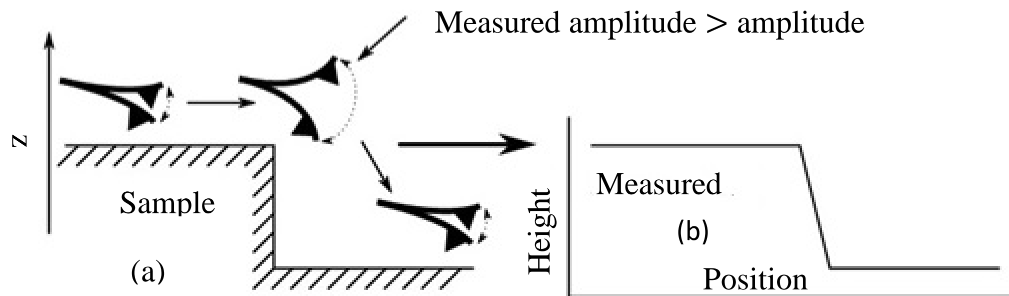

Figure 3.1: Schematic depiction of how the TM-AFM set-up adjusts the change in amplitude, attempting to match the amplitude setpoint. (a) adjustment process; (b) topography image of the sample

As indicated in Figure 3.1 (a), the tip scans across the sample with the amplitude close to the amplitude setpoint. Whilst scanning, the tip encounters a change in the topography that induces a change in the interaction force between the tip and sample. As a result, the measured drive amplitude differs from the amplitude set point. To minimize the difference between the measured amplitude and the amplitude setpoint value, the feedback moves the *z*-piezo up or down (down in this case) until the cantilever amplitude matches the setpoint gain. The vertical movement of the *z*-piezo is then recorded as the height (topographic image) of the sample (Figure 3.1 (b)) [58].

In addition, for effective imaging of the sample topography, the TM-AFM set-up uses two key components: a lock-in amplifier and a feedback loop. As an understanding of the working

principle and the interplay between these two components helps the operator to adjust appropriate scan parameters during scanning, details of these two components and how they work together need to be described.

A lock-in amplifier is a type of device that can extract a very small signal from a highly noisy environment. It consists of a signal mixer and a low pass filter. In the present context, its basic function is to extract the amplitude of the cantilever deflection due to tip-sample interaction, and to send it through to the feedback loop, where it will be adjusted and converted into an image of the scanned surface as shown in Figure 3.1 (b). Figure 3.2 presents a schematic representation of the function of the lock-in amplifier in tapping mode AFM.

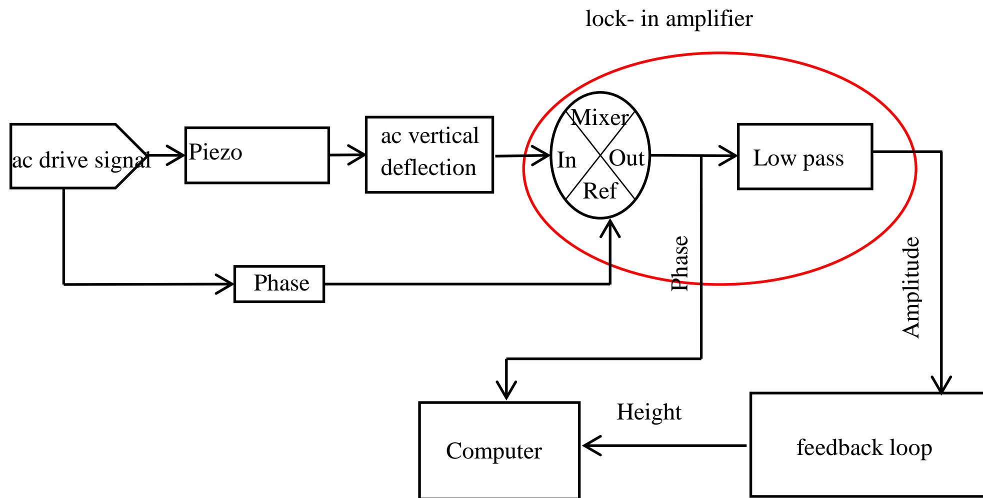

Figure 3.2: Schematic representation of tapping mode AFM.

As can be seen from Figure 3.2, an *ac* signal is initially sent to the TM piezo material. This *ac* drive signal causes the cantilever to oscillate and consequently will generate an *ac* vertical deflection. The *ac* vertical deflection mixed with the noise (from the environment) is detected by a photodiode and sent as an input to the lock-in amplifier. At the same time, the same *ac* drive reference signal with a specific phase (a value that can be modified by the user) is also sent directly to the lock-in amplifier. The main role of the signal mixer in the lock-in amplifier is to amplify the input signal, which has the same frequency as the reference signal, and to generate a *dc* output (amplitude). If both signals (the input and reference signals) are *sine* waves, their *multiplication* will produce two new signals with difference frequencies $(f_{in} - f_{ref})$ and $(f_{in} +$

f_{ref}), where f_{in} and f_{ref} are input and reference frequencies, respectively. To measure the amplitude of the *ac* vertical deflection, f_{in} and f_{ref} should be equal. When f_{in} and f_{ref} are equal, the phase difference between the input and reference signals is used for phase signal information. However, the *dc* signal and *ac* signal with $f_{in} + f_{ref}$ are sent to the low pass filter where the noise and the *ac* signal are filtered out, and the *dc* component is sent to the feedback loop. The feedback loop (which is the heart of an AFM system [58]), according to the amplitude setpoint value, adjusts the measured amplitude and uses the difference between the two values to image the topography of the sample via an automated system.

Once the topography of the sample is imaged appropriately, the electrical signal is activated (in the software) so that the CPD can be measured subsequently. The CPD values measured in this dissertation, when the data is obtained using the AM-KPFM method, are directly linked to the accuracy of the height or topography image [40]. This means that inaccurate topography measurements contribute to inaccurate electrical measurements. Hence, proper topographic imaging, in other words proper adjustment of the TM parameters, is crucial. As indicated above, CPD can be measured using either AM or FM mode. AM-KPFM involves two main stages [56]: in the first stage, the sample topography is obtained using TM-AFM and in the second stage, the cantilever stays at a constant height (lift height set by the user) with an external voltage in the form of $V_{dc} + V_{ac}\sin(w_{ac}t)$ [40] applied between the tip and sample (with a pre-set step size) to measure the CPD. Figure 3.3 shows a schematic representation of the working principle of AM-KPFM. In the case of FM, however, both the topography and potential are imaged at the same time and no lift is required.

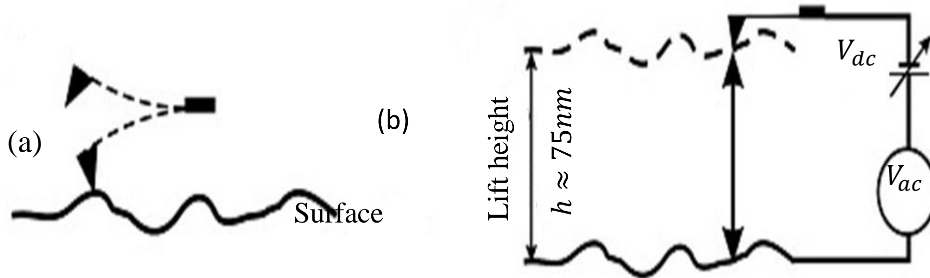

Figure 3.3: Schematic representation showing (a) tip in contact with the sample during the height measurement and (b) tip lifted to a constant height during the CPD measurement in AM-KPFM. V_{dc} Is the reverse *dc* voltage applied to compensate the CPD between the tip and the sample and the *ac* voltage $V_{ac}\,sin(w_{ac}t)$ is applied to

In conclusion, it has been emphasized that in TM-AFM, the accuracy in the topography and CPD measurements critically depends on the correct settings for the basic cantilever parameters, which include the drive amplitude, amplitude set point and the drive frequency. As indicated above, these parameters depend on the proper tuning of the cantilever. Therefore, poor tuning will generate obviously, a poor height image and consequently inaccurate CPD values, especially when using AM-KPFM. To make the feedback loop work properly or to set the appropriate parameters for the cantilever, the cantilever has to be well tuned [40]. This is mostly done by properly loading the cantilever in the cantilever slot indicated on the cantilever holder and mounting it on the Dimension Icon head. Furthermore, choosing an appropriate range of frequencies during the tuning process is also crucial. The range of frequencies selected should be according to the value of the nominal frequency supplied by the manufacturer and it is often indicated on the box containing the tip. The accurate alignment of the laser on the shiny backside of the cantilever and proper optical focusing on the cantilever is also important.

Tuning of Cantilever

Tuning of the cantilever can be done either automatically by the software or manually. A detailed procedure for this is described elsewhere [40]. Figure 3.4 shows a screen shot of an auto tuning curve where the software displays the tuning curve and parameters. The blue curve is the amplitude versus frequency and the red one is the phase versus frequency. The drive frequency is determined by the intersection of the vertical green line and the frequency-axis, whereas the amplitude setpoint is determined by the intersection of the pink horizontal line and the amplitude-axis. The intersection between the green line and the phase curve also allows an estimate of the initial phase, while a point close to the maximum in the amplitude plot is normally chosen as the initial drive amplitude.

For this particular tuning, a SCM-PIT probe from Bruker (this type of probe was used for all the AM-KPFM measurements in this project) with the nominal natural frequency in range of 60-100 kHz has been used. The drive frequency was set at 65.19 kHz and the amplitude setpoint at 35.03 nm. The initial phase and drive amplitude were $\sim 20^o$ and 56 nm, respectively. As expected, the drive frequency is well within the nominal frequency range supplied by the manufacturer.

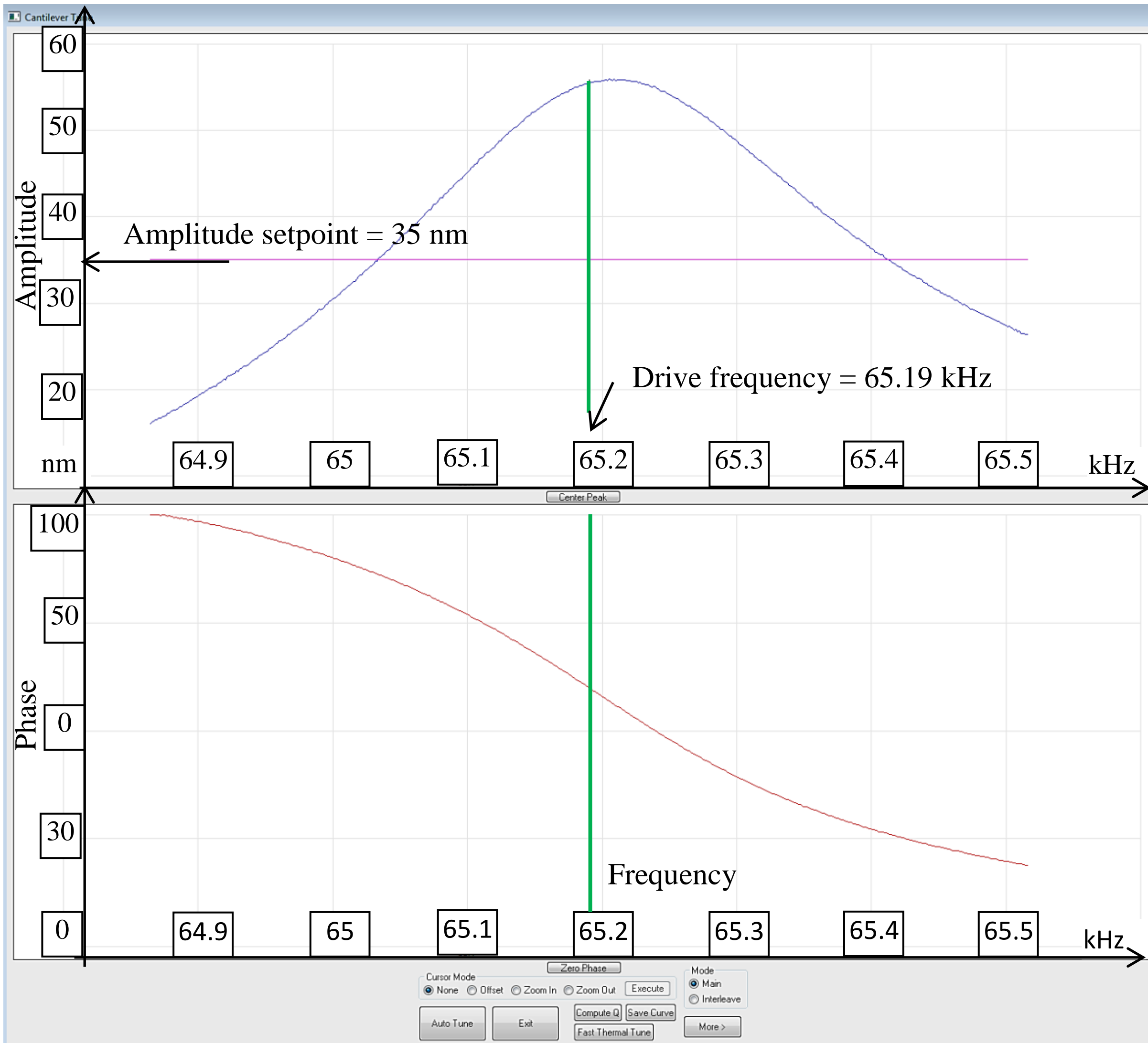

Figure 3.4: Typical cantilever tune panel for AM-KPFM. The main parameters include the drive amplitude, amplitude setpoint and drive frequency. The top curve is amplitude vs frequency, whereas the bottom curve is phase vs frequency.

3.2 Electrostatic properties of *n*+/SI -GaAs junction

Details of the electrostatic and current transport properties of *n*+/semi-insulating GaAs junctions have been described in reference [59]. In this section, the focus will be on those electrostatic properties of *n*+/SI-GaAs junctions that pertain to the results presented in chapter 5. As described in the following sections, the electrostatic properties of any junction depend primarily on the positions of the Fermi levels of the two materials that form the metallurgical junction. As indicated throughout the thesis, the n^+- *type* GaAs epilayer is doped with Si and its Fermi level is above the conduction band edge. That of the SI-GaAs is determined by the position of the

impurity used as a compensation. As described in reference [59], traditionally SI-GaAs is compensated by three generic mechanisms. These include compensation by: (i) a deep donor interacting with a shallow acceptor (DDSA), where the deep donors are As_{Ga} antisite defects (As residing on a Ga lattice site) complexed with an additional As interstitial, often known as the EL2 (its energy is approximately 0.73 eV above the valence-band edge) and the shallow acceptor is carbon or Ga_{As} antisite defects (Ga residing on a As lattice site with energy around 0.078 to 0.2 eV above the valance band edge [60]), (ii) a shallow donor and a deep acceptor (SDDA), such as large concentrations of Si and chromium (Cr), respectively; and (iii) a deep donor and a deep acceptor (DDDA), for example the EL2 as the deep donor and Cr as the deep acceptor.

In the case of the DDSA compensation scheme, at room temperature the position of the Fermi level is reported to be locked slightly above the intrinsic level (*i.e.* mid-gap) [59]. This indicates that the equilibrium electron concentration (~10^{16} cm^{-3}) in the bulk semi-insulating region is greater than the equilibrium hole concentration (~10^{15} cm^{-3}) [60]. As a result, such SI-GaAs can be considered as slightly *n*-type. Hence, when a junction is formed between an epilayer (n^+ side) and this *n-type* SI-GaAs (Figure 3.5(a)), the excess electrons from the epilayer side diffuse in to the SI region, resulting in a monotonic decrease in electron density across the junction (space charge region) as shown by the dashed line in Figure 3.5(b). The hole density follows a complementary profile [59]. Since the electron concentration in the bulk of the SI-GaAs is larger than the hole concentration, this means that the two carrier concentration profiles will not cross in the junction area, as shown by the dashed lines in Figure 3.5 (b) [59]. Thus the n^+/SI junction does not exhibit a depletion region. Similarly, in the case of DDDA, where light Cr doping is used to compensate the EL2 defect centers, the Fermi level is locked to a position slightly above the Cr deep level, which produces slightly *n-type* semi-insulating material. As a result, no depletion regions are formed in this situation also. The n^+/SI junction formed using these two compensation mechanisms behaves more like that of an isotype junction [59].

However, in the cases of SDDA compensation, which involves strong Cr compensation of residual silicon as a shallow donor, the Fermi energy position lies slightly below the intrinsic carrier energy [59]. As a result, the equilibrium hole density is greater than that of the equilibrium electron density, producing slightly *p-type* semi-insulating material, and a small depletion region will form around the junction. This causes the junction to behave more closely

akin to a more familiar anisotype (*p-n*) junction [59]. The SI-GaAs substrate used in this study was produced by Liquid Encapsulated Czochralski (LEC) growth, which implies that the compensation mechanism involves the EL2 as deep donor and residual carbon as the shallow acceptor [59, 60] (*i.e.* the DDSA scheme). As a result, no depletion region is expected.

Built-in voltage of DDSA compensated n^+/SI junction

As described for conventional *p-n* junctions below, the built-in voltage for n^+/SI-GaAs junctions is also given by the difference between the Fermi-level positions within the bulk regions on each side of the junction. Unlike the case of conventional *p-n* junctions, however, where the built-in voltage is given by $qV_{bi} = k_B T ln(N_{d,n} + \frac{N_{sa,C}}{{n_i}^2})$ (n_i being the intrinsic carrier density), the built-in voltage in the case of a n^+/SI-GaAs junction in the DDSA compensation scheme is given by [59]:

$$V_{bi} = E_{F_{n^+}} - E_{F_{SI}}$$

$$= \left[\frac{E_c}{q} + \frac{kT}{q} F^{-1}_{1/2}\left(\frac{N_{d,n^+}}{N_c}\right)\right] - \frac{kT}{q}\left[\frac{E_{dd,EL2}}{kT} + ln\left(\frac{g_{1.EL2}}{g_{0,EL2}}\right) - ln\left(\frac{N_{dd,EL2}}{N_{sa,C}} - 1\right)\right]$$

$$= \frac{1}{q}\left(E_c - E_{dd,EL2}\right) + \frac{kT}{q} ln\left(\frac{g_{1.EL2}}{g_{0,EL2}}\right) - \frac{kT}{q} ln\left(\frac{N_{dd,EL2}}{N_{sa,C}} - 1\right) + \frac{kT}{q} F^{-1}_{1/2}\left(\frac{N_{d,n^+}}{N_c}\right) \quad 3.1$$

In the above equation,

- V_{bi} is the built-in potential
- $E_{dd,EL2}$ is the position of the EL2 in the band gap
- T is the temperature
- q is the electronic charge
- k is Boltzmann's constant
- E_c is the absolute minimum of the conduction band
- $g_{0,EL2}$ is the degeneracy of the EL2 level when empty of electrons
- $g_{1,EL2}$ is the degeneracy of the EL2 level when occupied by a single electron
- $N_{dd,EL2}$ is the deep donor density
- $N_{sa,C}$ is the shallow acceptor density

- $F^{-1}_{1/2}$ is the inverse Fermi integral function of order $1/2$
- N_c is the conduction band density of states
- N_{d,n^+} is the space charge density on the n$^+$-type side of the junction

Using for the EL2: $g_{1/g_0} = 0.845$, $N_{d,n^+} = 2 \times 10^{16}\ cm^{-3}$, $E_{dd,EL2} = 0.73$ eV and for carbon: $N_{sa,C} = 2 \times 10^{15}\ cm^{-3}$ and $E_{sa,C} = 0.026\ eV$ above the valance band edge, the value of the built-in voltage between a layer with $n = 1 \times 10^{18}$ cm^{-3} and the SI substrate, at room temperature, is around 0.60 V [59]. In the same way, the variation in equilibrium potential and carrier density (*n* and *p*) across the n^+/SI-GaAs junction in the DDSA compensation scheme has been plotted and reported by R. Darling in [59]. Figure 3.5 (dashed lines) shows the evolution of these quantities as a function of position.

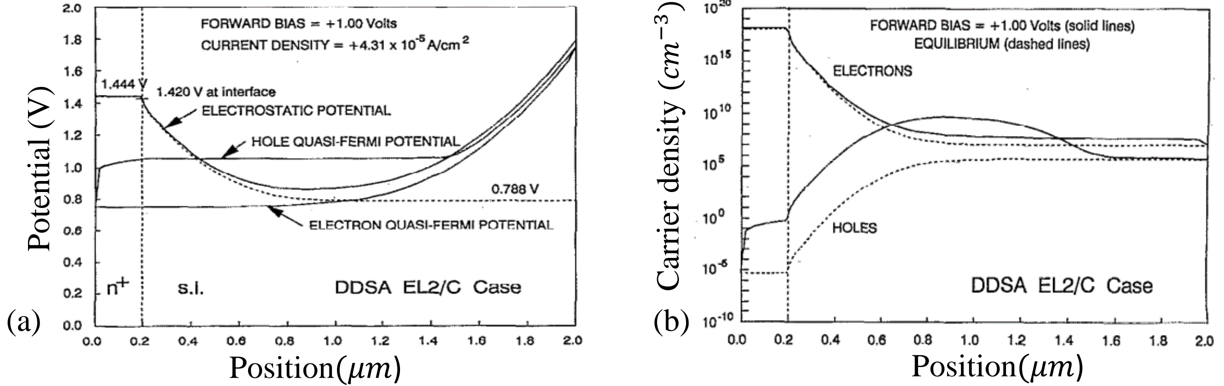

Figure 3.5: Numerically simulated potential and carrier density profiles for forward biased n^+/SI-GaAs junction: (a) electrostatic potential and electron and hole quasi-Fermi potentials; (b) case of electron and hole densities. Dashed lines indicate the equilibrium potential (in (a)) and electron and hole profiles (in (b)), respectively [59].

As can be seen in Figure 3.5 ((a) and (b)), because of the large electron density difference between the epilayer and substrate, the junction is highly asymmetrical, with nearly all of the space charge region appearing in the SI-GaAs.

As reported by R. Darling in [59] and mentioned above, the location of Fermi level in the bulk SI GaAs depends on the types of impurities and defects used as well as on the free carrier densities. Figure 3.6 [59] presents a Shockley plot for the case of DDSA compensation. This type of plot sums the contributions from all positive and negative charge species (including charged impurities/defects and free carriers of both types) on a logarithmic scale as function of the Fermi level. The Fermi level resulting in zero net space charge (i.e. space charge neutrality) is

determined as the intersection of the curves representing the net positive and net negative charges, respectively.

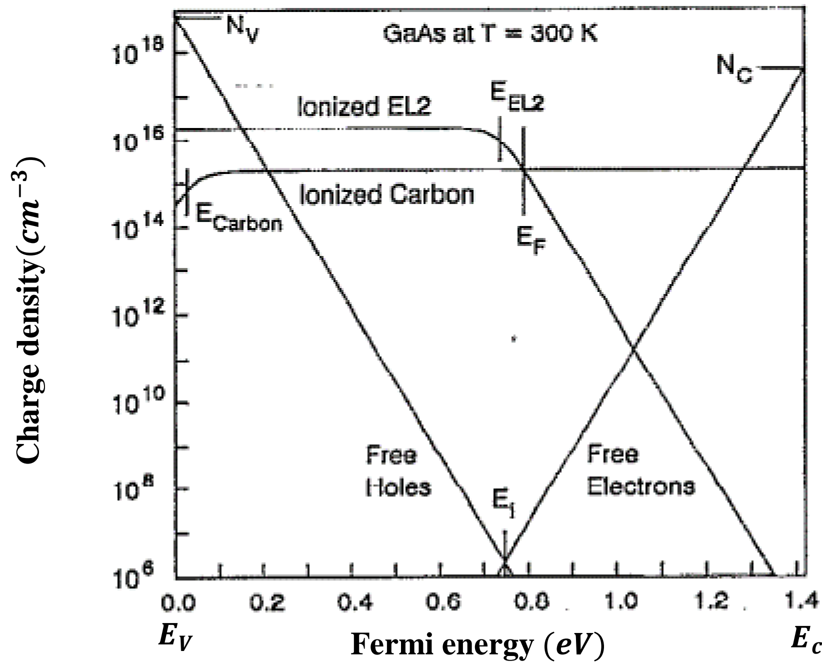

Figure 3.6**:** Shockley plot for DDSA SI-GaAs compensation. T, E_C, E_V, N_c, N_v and E_F are temperature**,** absolute minimum of the conduction band, absolute maximum of the valence band, density of states in the conduction band, density of states in the valence band and the Fermi level energy, respectively. $E_V = 0\ eV$, $E_C = 1.42\ eV$, $N_c \sim 10^{18} cm^{-3}$ and $N_V \sim 10^{18} cm^{-3}$ [59]**.**

Figure 3.6 clearly shows that the Fermi energy (E_F) for DDSA SI-GaAs compensation is slightly above the mid gap. It also shows that the Fermi energy for which space charge neutrality is achieved is slightly above the intrinsic value.

Electric field across DDSA compensated n^+/SI junction

In the same fashion, the electric field across the junction can also be theoretically described. As in the case of convectional *p-n* junctions, where charged shallow impurities on both side of the junction contribute to the field, the electric field across the n^+/SI junction also appears on both sides of the junction. The difference is the absence of a depletion region in the SI-region and the complexity of the sources (defects and impurities) contributing to the electric field. It should be noted here that the edge of a depletion region in a conventional *p-n* junction is where the majority carrier density drops to zero, leaving a fixed space charge from the ionized shallow impurity centers. The edge of the space-charge region in SI material, while similar in form, does

not arise in any way from the electron or hole densities, but is supported instead by the varying degree of ionization (or occupation) of the deep-level defects [59] . On the n^+ side of the junction only free electrons and fully ionized shallow donor levels contribute significantly to the space-charge density. As a result, the n^+ side can be treated in an identical manner to conventional abrupt *p-n* junctions [59] . If the density of fully ionized shallow donors on the n^+ side is N_{d,n^+}, the electric field is given by:

$$E_x(x) = \frac{qN_{d,n^+}}{\varepsilon}\left(x_{n^+}+x\right) \qquad 3.2$$

where $-x_{n^+} < x < 0$ is the width of the space charge region on the n+ side. As the density of electrons in the n^+ layer is much greater than that on the SI side, x_{n^+} should be comparatively small.

On the SI side of the junction, however, the situation is much more complex, with contributions to the space charge arising from many possible sources [59]. The main contribution comes from the filling of electrons of the shallow acceptor states in the SI region. As indicated above, when SI material is brought into contact with degenerate n^+-material, the electrons diffuse into the SI region, causing the Fermi level to rise within the space charge region. This has the effect of filling each of the deep levels to nearly their maximum occupancy with electrons for regions of the SI material sufficiently within the boundary of the space charge region. As a result of the space charge being controlled by deep-level defect occupation, rather than by majority-carrier depletion, the space-charge tails must be treated somewhat differently than in a conventional *p-n* junction [59].

As described in detail by Darling *et al.* [59], for the case of DDSA compensation, the EL2 defect centers are only partially ionized in the bulk of the SI region to produce charge neutrality, and become fully occupied by electrons within the space charge region. Since the EL2 is a deep donor, when fully occupied by electrons it is un-ionized and thus charge neutral. Hence, the net space-charge density is determined entirely by the residual C density, $N_{sa,C}$. As a result, the asymptotic electric field can be given by

$$E_x(x) = \frac{qN_{sa,C}}{\varepsilon}\left(x_{SI} - x\right) \qquad 3.3$$

where $0 < x < x_{SI}$ is the width of the space charge region on the SI side. Once again, as the electron densities on opposite sides of the junction are significantly different, the electric field is

asymmetric and dictated by the ratio $m = \frac{N_{d,n^+}}{N_{sa,c}}$ [59]. It is also important to note that $m = \frac{x_{SI}}{x_{n^+}} =$ 500. This implies that the space charge region of the SI side is 500 times that of the layer ($x_{SI} = 500\ x_{n^+}$). The electric field across the junction has been plotted using equation (3.2) and (3.3), and is displayed in Figure 3.7.

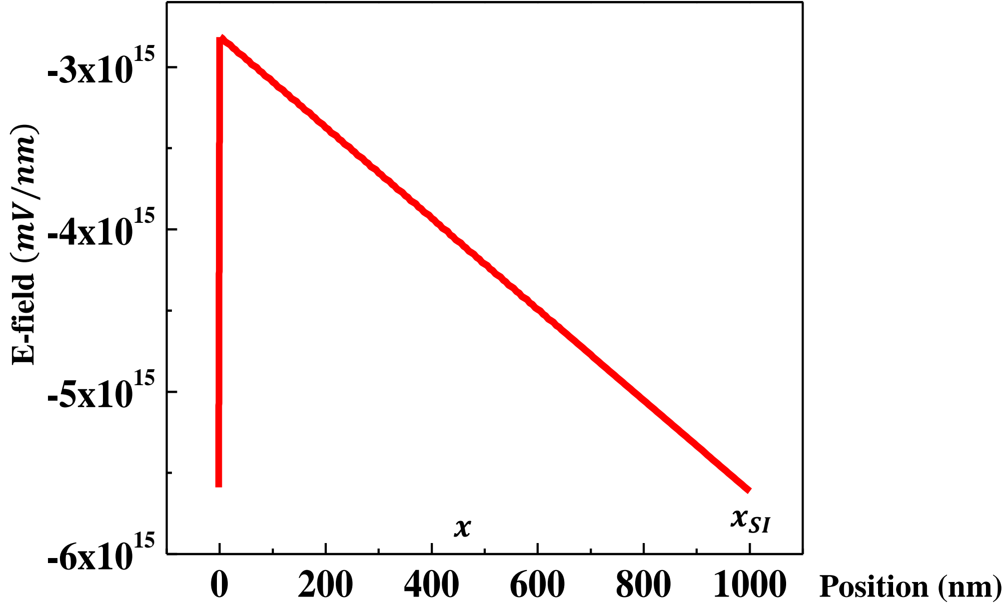

Figure 3.7: Electric field versus position. $N_{sa,C} = 2 \times 10^{15} cm^{-3}$, $\varepsilon = 114.22 \times 10^{-12}\ F/m$ and $q = 1.6 \times 10^{-19} C$.

Figure 3.7 shows that the space charge width is insignificant for $\boldsymbol{x \leq 0}$**,** (on the layer side). In general, the space charge region extends primarily into the SI side, up to a value of ~ 1000 nm for typical values of 2 nm width on the layer side, as seen in Figure 3.5. The electric field is maximum at $x = 0$ and decreases as one moves into the bulk regions.

3.3 Contact potential difference (CPD)

3.3.1 Overview and theory

In KPFM, the CPD is measured by minimizing the electrostatic force or electrostatic force gradient, caused by the flow of electrons between a sharp conducting tip and the sample. Figure 3.8 (a) demonstrates a model to describe the theoretical principles of CPD measurments. As shown in this figure, the tip and sample with different Fermi energy levels are almost brought in contact.

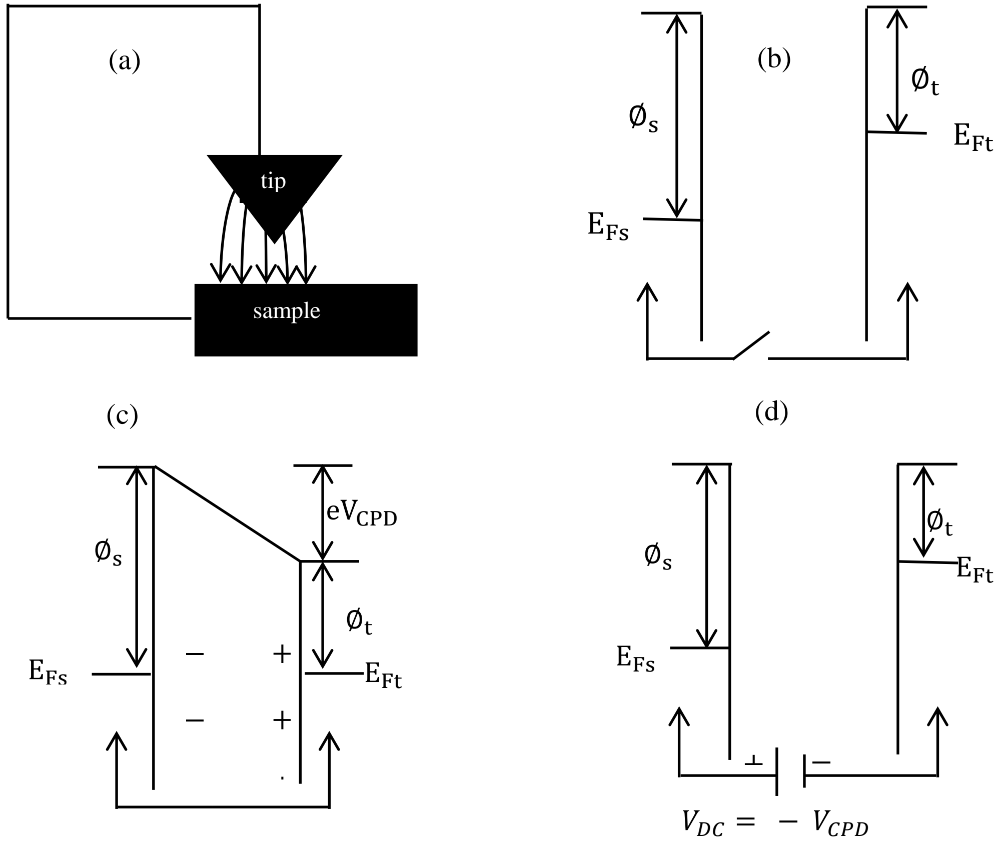

Figure 3.8: Theoretical principle of CPD: (a) tip and sample modeled as almost in contact; Relative Fermi energy levels and work functions of the tip and sample: (b) before contact (c) after electrical contact with the CPD indicated and (d) after an external reverse *dc* voltage $\boldsymbol{V_{dc}}$ is applied [40]. Here $\boldsymbol{\emptyset_s}$ and $\boldsymbol{\emptyset_t}$ are the work functions of the sample and the tip, respectively, whereas $\boldsymbol{E_{Fs}}$ and $\boldsymbol{E_{Ft}}$ are the Fermi energies of the sample and tip, respectively.

In principle, when two materials with different work functions are electrically connected to each other, due to the Fermi level difference between them, electrons will flow from the material with a lower work function (which means higher Fermi energy level) to the other until the Fermi levels are aligned. Figure 3.8 (b) shows the case of two materials (tip and sample) with different Fermi energy levels before physical contact. This figure also shows the schematic diagram of Fermi energy position of the two materials with respect to the vacuum level. If an external electrical voltage is applied between the tip and the sample, electrons flow from the material with higher Fermi energy level to the material with the lower Fermi energy level (from tip to sample in this configuration). Under this condition, the tip and the sample become charged and start to attract each other (Figure 3.8 (c)). As a result a potential difference, often known as the contact potential difference (CPD), is generated between the two materials. This contact potential noted as $\boldsymbol{V_{CPD}}$ can be measured by applying an external *dc* reverse voltage ($\boldsymbol{V_{dc}}$) until the previous

potential $\boldsymbol{V_{CPD}}$ becomes zero, Figure 3.8 (d). When $\boldsymbol{V_{CPD}}$ is zero, the *dc* voltage $\boldsymbol{V_{dc}}$ applied to cancel $\boldsymbol{V_{CPD}}$ is then recorded as the contact potential difference between the tip and sample.

Now consider the case where the sample contains multiple layers (substrate with one or more layer grown on top, for example) and each layer has a different work function so that a **built-in potential** is developed across the interface (substrate and the layer). KPFM can also be used to measure the **built-in potential** across such an interface (homo or heterojunction). The built-in potential between a layer and a substrate using KPFM is usually measured by scanning a cross-section of the sample, whereby the tip encounters both the layer and the substrate in one scan line. This means that if the layer and the substrate have different work functions, each will create different CPDs on the tip that can be used to measure the built-in potential between the layer and the substrate. Figure 3.9 demonstrates this principle.

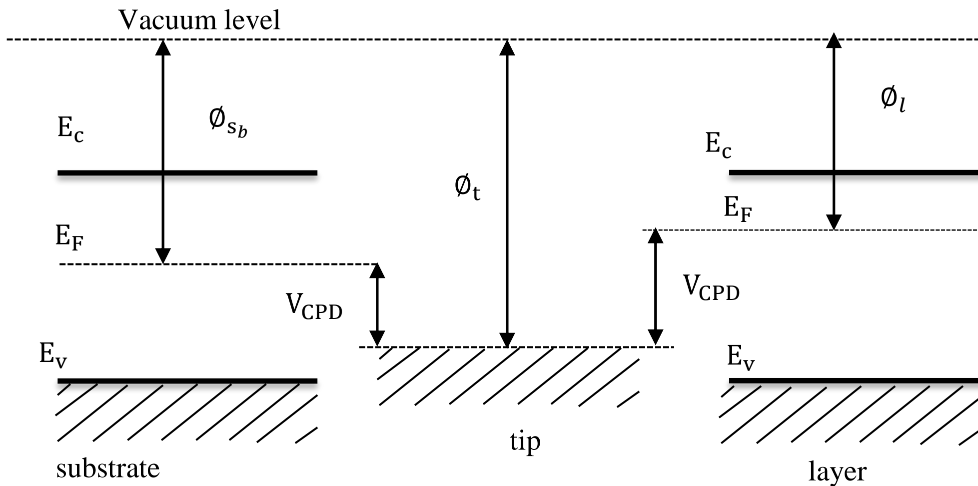

Figure 3.9: Energy band diagram illustrating how the CPD across the interface (junction) between two layers of a semiconductor is measured: $\boldsymbol{V_{dc}(substrate) = \emptyset_{S_b} - \emptyset_t}$ when the tip is above the substrate and $\boldsymbol{V_{dc}(layer) = \emptyset_l - \emptyset_t}$ when the tip is above the layer; $\boldsymbol{E_c}$, $\boldsymbol{E_v}$ and $\boldsymbol{E_F}$ are absolute minimum of the conduction band, absolute maximum of the valence band and the Fermi level positions, respectively.

Assume that the tip is scanning a cross section of the sample (containing substrate and the layer). When the tip is on the substrate side, the system measures the CPD between the tip and the substrate by applying a bias with magnitude $\boldsymbol{V_{dc}(substrate) = \emptyset_{S_b} - \emptyset_t}$, where $\boldsymbol{\emptyset_{S_b}}$ and $\boldsymbol{\emptyset_t}$ are the work functions of the substrate and that of the tip, respectively [13]. In the same scan line, when the tip reaches the layer side, it measures the CPD between the tip and layer by applying a nullifying potential given by $\boldsymbol{V_{dc}(layer) = \emptyset_l - \emptyset_t}$, where $\boldsymbol{\emptyset_l}$ is the work function

of the layer. This is repeated until the whole scan area is finished and the system displays the **built-in potential** between the layer and the substrate. Hence, the **built-in potential** between substrate and layer $\Delta\emptyset = \emptyset_{S_b} - \emptyset_l$, is approximatively obtained as an applied voltage difference, $\boldsymbol{V_{dc}(substrate) - V_{dc}(layer)}$, which equals the work function difference between substrate and layer in the case of an ideal semiconductor surface [13]. This implies that if the positions of the Fermi energy of the layer and substrate are theoretically known, the built-in potential between them can be deduced theoretically.

a) Theoretical aspects of CPD at a semiconducting homojunction

As indicated above the CPD between two layers depends on their respective work functions. The work function of a material is the minimum energy needed to raise an electron from the Fermi level to the vacuum level. It is always positive, and for semiconductors materials, its value decreases with an increase in the electron density. Its theoretical expression depends on the extent of doping of the semiconductor: semi-insulating, non-degenerate or degenerate. The schematic in Figure 3.10, based on the **Anderson model,** can be considered to express the band alignment and electron affinity.

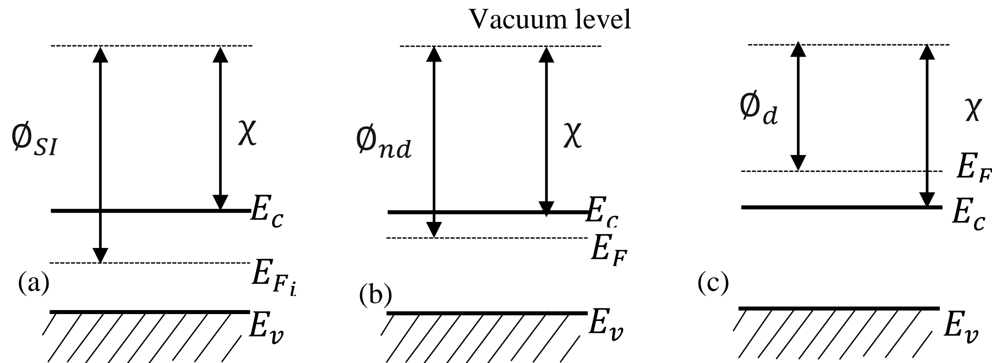

Figure 3.10**:** Sketch of energy band diagram using the Anderson model for: (a) semi-insulating, (b) *n-type* non-degenerate and (c) *n-type* degenerate semiconductor materials; $\emptyset_{SI}$, $\boldsymbol{\emptyset_{nd}}$, and $\boldsymbol{\emptyset_d}$ are the work functions of the semi-insulating, *n-type* non-degenerate and degenerate semiconductors materials, respectively; E_{F_i} and χ are the intrinsic Fermi level energy and electron affinity,

For the DDSA compensation scheme (described in section 3.2) the position of the Fermi level is slightly (0.038 eV) above mid gap. However, based on the fact that the measurements conducted in this study have been made in air, the comparison between the experimental and theoretical values is qualitative and not quantitative. Hence, for simplicity, all the following calculations

have done by assuming that the position of Fermi level on the SI side is pinned at the intrinsic level.

Based on Figure 3.10 (a), for semi-insulating semiconductor materials, the work function can be expressed as:

$$\emptyset_{SI} = \chi + (E_c - E_{F_i}) \tag{3.4}$$

where χ is the electon affinity (material dependent, but independent of doping) and the term $(E_c - E_{F_i})$ needs to be established.

It is known that, for intrinsic semiconductor materials the intrinsic density of electrons n_i is equal to the density of holes p_i. Mathematically, it can be expressed by [61]:

$$n_i = p_i \tag{3.5}$$

With

$$n_i = N_c exp\left[-\left(\frac{E_c - E_{F_i}}{kT}\right)\right] \tag{3.6}$$

$$p_i = N_v exp\left(\frac{E_v - E_{F_i}}{kT}\right) \tag{3.7}$$

and T, k, N_c and N_v are the temperature, Boltzmann constant, and density of states for the conduction and valence bands, respectively. By replacing (3.6) and (3.7) in (3.5), the latter can be written as:

$$N_c exp\left[-\left(\frac{E_c - E_{F_i}}{kT}\right)\right] = N_v exp\left(\frac{E_v - E_{F_i}}{kT}\right) \tag{3.8}$$

This implies:

$$E_{F_i} = \frac{E_c + E_v}{2} + \frac{1}{2} kT ln\left(\frac{N_v}{N_c}\right) \tag{3.9}$$

Using (3.9) and the following relationship,

$$\frac{N_v}{N_c} = \left(\frac{m_h^*}{m_e^*}\right)^{3/2}$$

where, m_h^* and m_e^* are the effective mass of holes and electrons, respectively, the expression in equation 3.9 becomes

$$E_c - E_{F_i} = \frac{E_c - E_v}{2} - \frac{3}{4} kTln\left(\frac{m_h^*}{m_e^*}\right)$$

This implies:

$$E_c - E_{F_i} = \frac{E_g}{2} - \frac{3}{4} kTln\left(\frac{m_h^*}{m_e^*}\right) \qquad 3.10$$

By using (3.10) in (3.4), the work function of a semi-insulating semiconductor can be given by:

$$\emptyset_{SI} = \chi + \frac{E_g}{2} - \frac{3}{4} kTln\left(\frac{m_h^*}{m_e^*}\right) \qquad 3.11$$

In the same way, for *n-type* non-degenerate semiconductor materials (Figure 3.10 (b)) the electron density n can be given by:

$$n = N_c exp\left[-\left(\frac{E_c - E_F}{kT}\right)\right] \qquad 3.12$$

Rearranging this equation, the work function for non-degenerate *n-type* material $\emptyset_{nd}$ (= $\chi + (E_c - E_F)$ and the Fermi energy level $E_{F_{nd}}$ can, respectively, be written as:

$$\emptyset_{nd} = \chi + kTln\left(\frac{N_c}{n}\right) \qquad 3.13$$

$$E_{F_{nd}} = E_c - kTln\left(\frac{N_c}{n}\right) \qquad 3.14$$

Therefore, the built-in potential difference between semi-insulating substrate and an *n-type* non-degenerate semiconductor of the same material can be approximated by using equations(3.11) and (3.13) which will be discussed shortly.

In the case of *n-type* degenerate semiconductor materials, which is the case for most of the samples studied in this dissertation, the Fermi energy level E_F is above the conduction band (Figure 3.10 (c)) and the work function $\emptyset_d$ can be written as:

$$\emptyset_d = \chi - (E_F - E_o) \qquad 3.15$$

E_o is the energy from which the material starts to be degenerate $(n > N_c)$ and $(E_F - E_o)$ as shown by J. Singh in reference [62] can be expressed as:

$$E_F - E_o = kT\left[ln\left(\frac{n}{N_c}\right) + \frac{1}{\sqrt{8}} \times \frac{n}{N_c}\right] \qquad 3.16$$

However, E_o is not constant. It changes with the dopant concentration and can analytically be given as:

$$E_o = E_C - \Delta E_g \qquad 3.17$$

where the term ΔE_g, which depends not only on the interaction of the free carriers with themselves (or electron-hole interactions) but also on the interaction of the free carriers with their surroundings (ionized impurities), is called band gap narrowing [63].

For *n-type* degenerate GaAs for example, ΔE_g is given by [63]:

$$\Delta E_g(meV) = A\left(\frac{n}{10^{18}}\right)^{1/3} + B\left(\frac{n}{10^{18}}\right)^{1/4} + C\left(\frac{n}{10^{18}}\right)^{1/2} \qquad 3.18$$

The coefficients A, B and C are given in table 3.1 [63].

Table 3.1: Coefficients *A, B* and *C* describing band gap narrowing in *n*-GaAs

	A (meV)	B (meV)	C (meV)
n-GaAs	16.30	7.47	90.65

By combining equation (3.15) and equation (3.16), and by replacing (3.17) in (3.16) the work function $\emptyset_{d_{GaAs}}$ and the Fermi energy level $E_{F_{d_{GaAs}}}$ of *n-type* degenerate GaAs are respectively given by:

$$\emptyset_{d_{GaAs}} = \chi_{GaAs} - kT\left[ln\left(\frac{n}{N_c}\right) + \frac{1}{\sqrt{8}} \times \frac{n}{N_c}\right] \qquad 3.19$$

$$E_{F_{d_{GaAs}}} = E_C - \Delta E_{g_{GaAs}} + kT\left[ln\left(\frac{n}{N_c}\right) + \frac{1}{\sqrt{8}} \times \frac{n}{N_c}\right] \qquad 3.20$$

Using equations (3.14), (3.16) and (3.20) for *n-type* non-degenerate, *n-type* degenerate GaAs without and with the effect of band gap narrowing taken in account, respectively, the evolution of the Fermi energy level versus electron density for GaAs is shown in Figure 3.11.

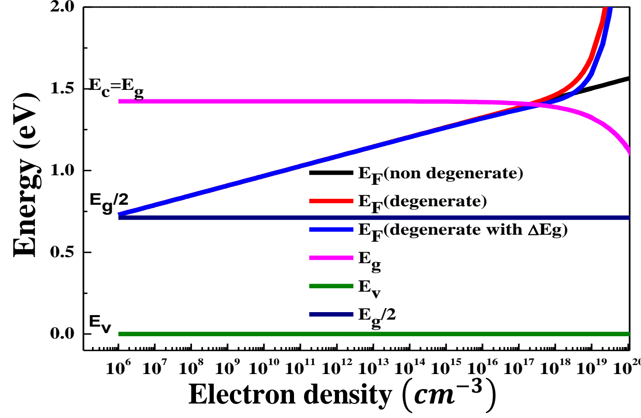

Figure 3.11: Fermi energy level versus electron density of *n-type* non-degenerate and degenerate GaAs: $\boldsymbol{N_C = 4.70 \times 10^{17}\ cm^{-3}}$, $\boldsymbol{E_c = E_g = 1.424\ eV}$, $\boldsymbol{E_v = 0\ eV}$, $\boldsymbol{T = 300\ K}$, $\boldsymbol{k = 8.62 \times 10^{-5}}$ eV/K and $\boldsymbol{E_o = 1.415 eV}$, slightly below E_c has been calculated from equation (3.16) for $n = N_C$.

Figure 3.11 shows that for $n \leq N_c$ (where N_c for GaAs is $4.70 \times 10^{17}\ cm^{-3}$) the Fermi energy level is almost the same for both degenerate and non-degenerate GaAs. Differences only become significant for electron density n greater than N_c.

In fact,

- When $n \ll N_c$ (the case of non-degenerate GaAs), n/N_c is much less than 1 and equation (3.16) can mathematically be approximated to equation (3.14) as revealed by the graph.

- When $n \gg N_c$ (case of degenerate GaAs), the graph of equation (3.14) continues to increase linearly (on a log scale) whereas the graph from equation (3.16) increases exponentially (on a log scale). Therefore, one can say that equation (3.14) can only be used for non-degenerate GaAs and equation (3.16) holds for both degenerate and non-degenerate GaAs. This final conclusion is valid for the work function as well. Furthermore, the graph also shows a small decrease in Fermi energy level (when the electron density increases) due to the effect of band gap narrowing. This lowering of the

Fermi level can be associated with the value of E_o which becomes smaller with an increase in electron density.

Based on these calculations, the ideal **built-in potential,** also called the CPD, across the junction between two different semiconductor layers can now be derived. It is equal to the difference in work functions between the layers and in this particular case can be theoretically approximated by using the relationship $|\emptyset_{S_b} - \emptyset_l|$[54].

In the case of *n-type* GaAs grown on semi-insulating GaAs substrate, for example, the CPD between the layer and the substrate depends on the concentration of the dopant:

- For *n-type* non-degenerate GaAs grown on semi-insulating GaAs,

$$V_{CPD_{nd_{GaAs}}} = \left| \frac{E_{g_{GaAs}}}{2} - kT\left[\frac{3}{4} ln\left(\frac{m^*_{h_{GaAs}}}{m^*_{e_{GaAs}}}\right) + ln\left(\frac{N_c}{n}\right)\right]\right| \quad 3.21$$

- For *n-type* degenerate GaAs grown on semi-insulating GaAs, without the effect of band gap narrowing,

$$V_{CPD_{d_{GaAs}}} = \left| \frac{E_g}{2} + kT\left[ln\left(\frac{n}{N_c}\right) + \frac{1}{\sqrt{8}} * \frac{n}{N_c} - \frac{3}{4} ln\left(\frac{m^*_{h_{GaAs}}}{m^*_{e_{GaAs}}}\right)\right]\right| \quad 3.22$$

- For *n-type* degenerate GaAs grown on semi-insulating GaAs, with the effect of band gap narrowing,

$$V_{CPD_{d_{GaAs}}} = \left| \frac{1}{2}\left(E_g - \Delta E_g\right) + kT\left[ln\left(\frac{n}{N_c}\right) + \frac{1}{\sqrt{8}} * \frac{n}{N_c} - \frac{3}{4} ln\left(\frac{m^*_{h_{GaAs}}}{m^*_{e_{GaAs}}}\right)\right]\right| \quad 3.23$$

b) Theoretical aspects of CPD at a semiconducting heterojunction

In this section, the cases of the CPD between two heterojunctions, namely *n-type* non-degenerate InGaAs on SI-GaAs and undoped *n-type* AlGaAs on SI-GaAs, are presented. As shown below, the theory behind the ideal CPD across a heterointerface (*i.e.* the interface between two different semiconductors) is slightly different. To illustrate this difference, a schematic energy band diagram of InGaAs (strain-relaxed) on GaAs substrate, using Anderson model, is shown in Figure 3.12.

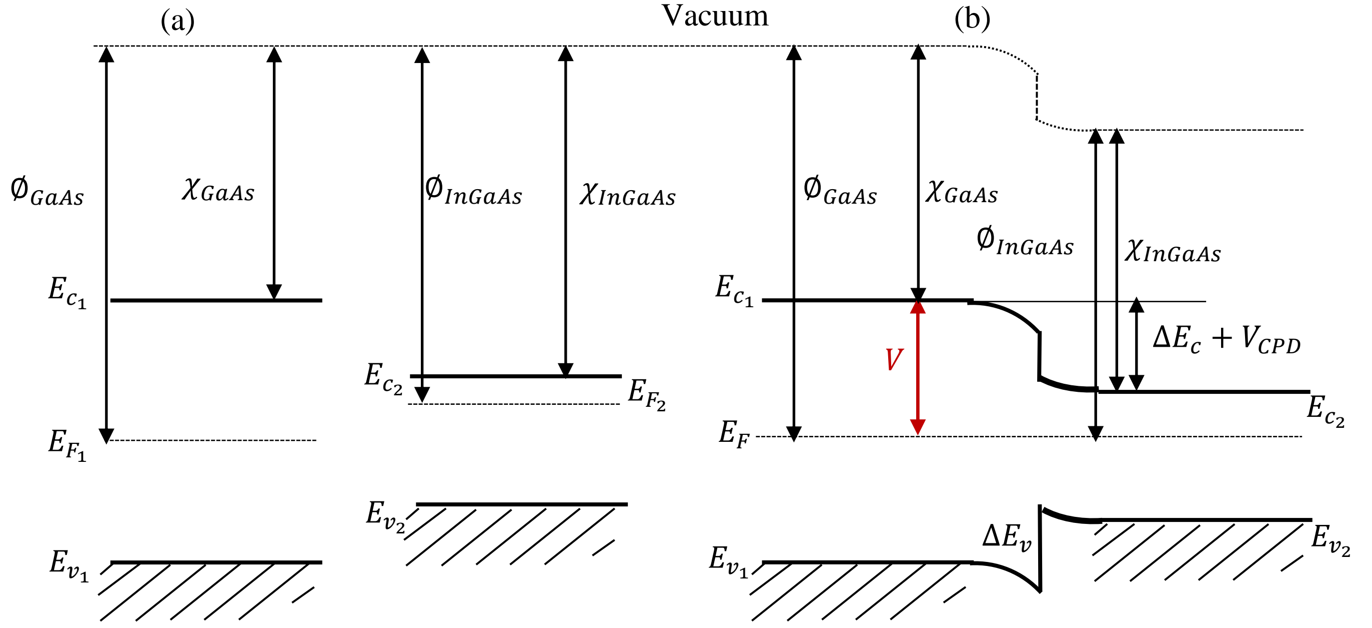

Figure 3.12: Sketch of energy band diagram using the Anderson model for *n-type* InGaAs grown on GaAs substrate: (a) before contact and (b) after contact. $\boldsymbol{E_c}$, $\boldsymbol{E_v}$, $\emptyset$, $\boldsymbol{\chi}$, $\boldsymbol{E_F}$. $\boldsymbol{\Delta E_v}$, $\boldsymbol{\Delta E_c}$ and $\boldsymbol{V_{CPD}}$ are the absolute minimum of the conduction band, absolute maximum of the valence band, work function, electron affinity, Fermi energy**,** band offsets and contact potential difference, also called the built-in potential, respectively. $\boldsymbol{V}$ is used in the derivation of the CPD.

Based on Figure 3.12 (b),

$$V = V_{CPD} + \Delta E_c + \left(E_{c_2} - E_F\right) \qquad 3.24$$

At the same time V and $E_{c_2} - E_F$ can also be written as:

$$V = \emptyset_{GaAs} - \chi_{GaAs} \qquad 3.25$$

$$E_{c_2} - E_f = \emptyset_{InGaAs} - \chi_{InGaAs} \qquad 3.26$$

By substituting (3.25) and (3.26) into (3.24), (3.24) becomes:

$$\emptyset_{GaAs} - \chi_{GaAs} = V_{CPD} + \Delta E_c + \emptyset_{InGaAs} - \chi_{InGaAs} \qquad 3.27$$

This implies,

$$\begin{aligned} V_{CPD} &= \emptyset_{GaAs} - \emptyset_{InGaAs} - \Delta E_c + \chi_{InGaAs} - \chi_{GaAs} \\ &= \emptyset_{GaAs} - \emptyset_{InGaAs} - \Delta E_c + \Delta E_c \\ &= \emptyset_{GaAs} - \emptyset_{InGaAs} \end{aligned}$$

So,

$$V_{CPD} = \emptyset_{GaAs} - \emptyset_{InGaAs} \quad 3.28$$

where $\emptyset_{GaAs}$ is given by equation (3.11) and $\emptyset_{InGaAs}$ can be expressed as follows:

$$\emptyset_{InGaAs} = \chi_{InGaAs} + kTln\left(\frac{N_c}{n}\right) \quad 3.29$$

In equation (3.29), N_c is the effective density of states in the conduction band of InGaAs.

It is essential to note that for a heterointerface, the energy band gap, electron affinity and effective masses are not constant as in the case of the homojunction (GaAs layer grown on GaAs substrate).

As can be seen in the following equations, for *n-type* InGaAs grown on SI-GaAs substrate for example, these quantities depend on the concentration of InAs in InGaAs. For unstrained $In_xGa_{(1-x)}As$, where x is the mole fraction of InAs, the energy band gap is given by: [64].

$$E_{gu}(x) = 1.43 - 1.53x + 0.45x^2 \quad 3.30$$

where $E_{gu}(x)$ is the energy band gap of unstrained InGaAs.

The effective masses and electron affinities are linearly interpolated by using the following graph.

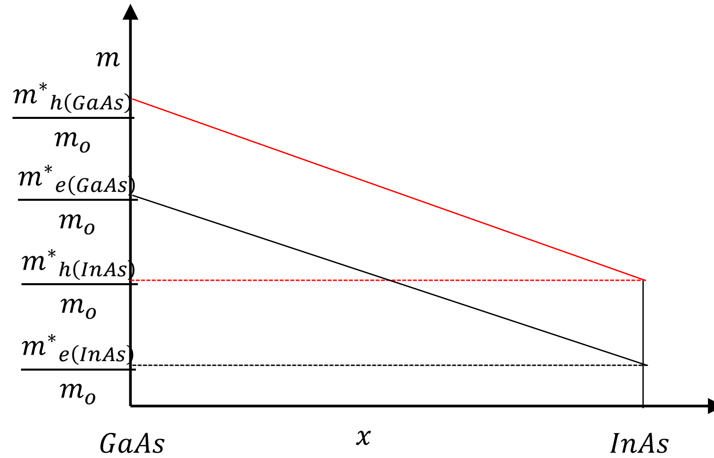

Figure 3.13: Linear interpolation scheme for the effective masses versus mole fraction x in $\mathbf{In_xGa_{(1-x)}As}$. The red solid line represents the evolution of the effective mass of holes as a function of mole fraction of InAs; and the black line is that of the effective mass of the electron.

As the measurements in this study are performed at ambient conditions, the effective masses of electrons m_e and holes m_h in GaAs and InAs at 300 K are used: $\frac{m^*{}_{e(GaAs)}}{m_0} \approx 0.064$ and $\frac{m^*{}_{e(InAs)}}{m_0} \approx 0.023$; $\frac{m^*{}_{h(GaAs)}}{m_0} \approx 0.47$ and $\frac{m^*{}_{h(InAs)}}{m_0} \approx 0.41$ [65].

Based on Figure 3.13, the formula for the effective mass of electrons and that for holes can be expressed as:

$$m^*{}_e(x) = \left(\frac{m^*{}_{e(InAs)}}{m_0} - \frac{m^*{}_{e(GaAs)}}{m_0}\right)x + \frac{m^*{}_{e(GaAs)}}{m_0} \qquad 3.31$$

and

$$m^*{}_h(x) = \left(\frac{m^*{}_{h(InAs)}}{m_0} - \frac{m^*{}_{h(GaAs)}}{m_0}\right)x + \frac{m^*{}_{h(GaAs)}}{m_0} \qquad 3.32$$

where $m^*{}_e$ is the effective mass of electrons and $m^*{}_h$ that of holes in $In_xGa_{(1-x)}As$. By inserting constant values (at 300 K), (3.31) and (3.32) can be re-written as:

$$m^*{}_e(x) = -0.045x + 0.069 \qquad 3.33$$

and

$$m^*{}_h(x) = -0.06x + 0.47 \qquad 3.34$$

In the same way, the electron affinity of $\mathrm{In_xGa_{(1-x)}As}$ as a function of mole fraction x can be established and is expressed as:

$$\chi_{In_xGa_{1-x}As} = 0.83x + 4.07 \qquad 3.35$$

Electron affinity values around $\chi_{GaAs} \approx 4.07\ eV$ and $\chi_{InAs} = 4.9\ eV$ [66] have been considered for pure GaAs and InAs, respectively. Therefore, the CPD across the interface between *n*-type non-degenerate, strain-relaxed $\mathrm{In_xGa_{1-x}As}$ grown on SI- GaAs substrate can be written as:

$$V_{CPD_{In_xGa_{(1-x)}As}} = \frac{E_{g_{GaAs}}}{2} + \left(\chi_{GaAs} - \chi_{In_xGa_{(1-x)}As}\right) - \left[kTln\left(\frac{N_c(x)}{n}\right) + \frac{3}{4}kTln\left(\frac{m^*{}_{h(GaAs)}}{m^*{}_{e(GaAs)}}\right)\right] \qquad 3.36$$

Where n is the electron density in undoped InGaAs. In the same way, the CPD of AlGaAs grown on SI-GaAs can be expressed as by:

$$V_{CPD_{Al_xGa_{(1-x)}As}} = \frac{E_{g_{GaAs}}}{2} + \left(\chi_{GaAs} - \chi_{\,Al_xGa_{(1-x)}As}\right) - \left[kTln\left(\frac{N_c(x)}{n}\right) + \frac{3}{4}kTln\left(\left(\frac{m^*{}_{h(GaAs)}}{m^*{}_{e(GaAs)}}\right)\right)\right] \quad 3.37$$

Where n is the electron density in undoped AlGaAs. One of the main objectives of this study is to experimentally determine the **built-in potentials across** various homo- and heterojunctions using KPFM methods and to compare these values with the CPD-values given by equations (3.23), (3.36) and (3.37). This has been attempted by employing the two main operating modes, namely AM-KPFM and FM-KPFM.

3.4 Amplitude modulation (AM)-KPFM

3.4.1 Theory

As described above, the determination of the CPD using AM-KPFM is based on measurements of the electrostatic forces between the sharp conducting tip and the sample. Theoretically, the tip and the sample can be modeled as a parallel plate capacitor [41]. Figure 3.14 illustrates this configuration in which the Fermi level of the tip is assumed higher than that of the sample causing electrons to flow from tip to sample. Hence the tip and sample become the positively and negatively charged sides of the capacitor, respectively.

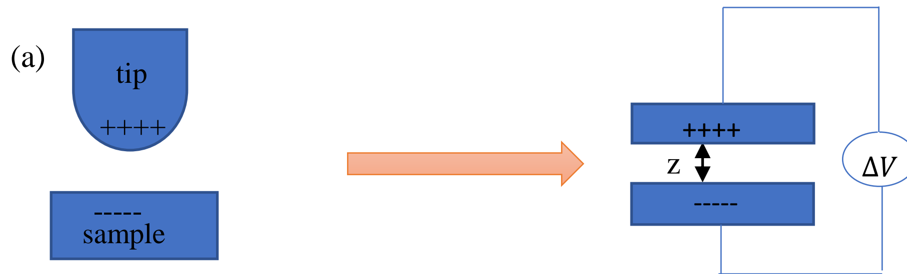

Figure 3.14: Tip-sample modeling: (a) real situation; (b) ideal situation; ΔV is voltage difference. Here, it is assumed that the work function of the tip is lower than that of sample and z is the tip-sample distance.

With this configuration, the electrostatic force between the tip and sample can be written as [67]:

$$F_{el} = -\frac{1}{2}\frac{\partial C}{\partial z}(\Delta V)^2 \quad 3.38$$

In the above equation, F_{el} is the electrostatic force between the tip and sample, $\frac{\partial C}{\partial z}$ the capacitance gradient which depends on the tip geometry and the tip-sample distance z [67] and ΔV is the potential difference.

The potential difference, ΔV, in KPFM operation consists of both *ac* and *dc* components. The *ac* component, in the form of $V_{ac}\sin(w_{ac}t)$, is applied by the piezo to electrically excite the cantilever at or near its resonance frequency. The *dc* component consists of the CPD and the externally applied voltage to compensate the CPD; *i.e* $\Delta V_{dc} = V_{dc} - V_{CPD}$.

Hence, over all:

$$\Delta V = V_{dc} - V_{CPD} + V_{ac}\sin(w_{ac}t) \quad 3.39$$

By definition, V_{CPD} is given by [68]:

$$V_{CPD} = \frac{\Delta\emptyset}{e} = \frac{\emptyset_s - \emptyset_t}{e} \quad 3.40$$

here e is the elementary charge, $\emptyset_s$ and $\emptyset_t$ are the work functions of the sample and the tip, respectively.

Substituting equation (3.39) in equation (3.38), the term $(\Delta V)^2$ involves *sine* square. By using the trigonometric relationship: $\cos(2x) = 1 - 2[\sin(x)]^2$, equation (3.38) can also be rearranged and written as [57]:

$$F_{el} = \underbrace{-\frac{\partial C}{\partial z}\left[\frac{1}{2}(V_{dc} - V_{CPD})^2 + \frac{V_{ac}^2}{4}\right]}_{\substack{dc\ term \\ F_{dc}}} \underbrace{- \frac{\partial C}{\partial z}(V_{dc} - V_{CPD})V_{ac}\sin(w_{ac}t)}_{\substack{w\text{ term} \\ F_{w_{ac}}}} + \underbrace{\frac{\partial C}{\partial z}\frac{V_{ac}^2}{4}\cos(2w_{ac}t)}_{\substack{2w\text{ term} \\ F_{2w_{ac}}}} \quad (3.41)$$

Here, the oscillating electric force $F_{w_{ac}}$ (w term) acts as a sinusoidal driving force that can excite motion in the cantilever. This is mostly because of the fact that the cantilever responds only to force at/or near its resonance frequency. In other words, the F_{dc} and $F_{2w_{ac}}$ components do not

cause any significant oscillation of the cantilever [40]. In particular, the F_{dc} term which involves the CPD information is constant. This implies that it cannot generate any electrical vibration of the cantilever. The term $F_{2w_{ac}}$ meanwhile is an *ac*-signal but does not contain the CPD information that the KPFM technique measures. Those two terms (F_{dc} and $F_{2w_{ac}}$) are therefore used for topography and capacitance microscopy imaging [41], respectively. The $F_{w_{ac}}$ term, which simultaneously contains the ac-signal with frequency w_{ac} and CPD information, can hence be used to measure the CPD [57] between the tip and sample by minimizing the amplitude ($\frac{\partial C}{\partial z}(V_{dc} - V_{CPD})V_{ac}$) of the force $F_{w_{ac}}$. As indicated above, the main purpose of the feedback loop is then to minimize this amplitude during the AM-KPFM measurements. More explicitly, when the *dc* applied bias equals the work function difference ($V_{dc} = V_{CPD}$), the amplitude of the force at w_{ac} becomes zero and the lock-in amplifier measures the applied *dc* bias which is interpreted as V_{CPD}. However, with the information from the amplitude alone, the feedback loop cannot minimize the difference between the applied bias and the work function. As can be seen from the $F_{w_{ac}}$ term in equation (3.41), namely $\frac{\partial C}{\partial z}(V_{dc} - V_{CPD})V_{ac}\sin(w_{ac}t)$, when $V_{dc} - V_{CPD}$ is different from zero (or not minimum), one cannot measure the work function correctly. For example, a value of $V_{dc} - V_{CPD} = 1\ V$ will translate into the same amplitude as a value $V_{dc} - V_{CPD} = -1\ V$. Hence, the feedback loop will not function properly. So, based on feedback from the amplitude alone, the system (feedback loop) cannot minimize the amplitude correctly and this leads to inaccurate CPD values. For this purpose, the feedback system during AM-KPFM measurements also requires the lock-in phase to be set correctly by the operator. In the AM-KPFM set-up of the Nanoscope software, there are two ways that the operator can adjust the lock-in phase: automatically by the software or using a manual electrical sweep [40]. In both cases, the software displays the amplitude vs lock-in-phase where the operator selects the lock-in-phase around which the amplitude is minimum.

Once the lock-in phase is properly set, the AM-KPFM technique measures the amplitude of the electrostatic force $F_{w_{ac}}$. The main target of the potential feedback loop is to adjust V_{dc} such that $V_{dc} - V_{CPD} = 0$. When this is fulfilled the system measures the CPD at that instant, which equals V_{dc} for that particular point on the sample. Once the CPD is measured, which is the work

function of the sample relative to that of the tip, equation (3.40) can be used to deduce the work function of the sample provided that that of the tip is calibrated against a known sample [41].

3.4.2 AM-KPFM set-up details

This section is focused on the practical procedure of an AM-KPFM system. As indicated above, the AM-setup measures the amplitude of the cantilever oscillation, induced by the electrostatic force $F_{w_{ac}}$, using two main stages. During the first stage, the surface topography (height variations) is determined using TM-AFM. During the second stage, the surface is retraced at a set lift height from the surface to measure the CPD. During this second stage, the drive piezo is turned off, *i.e*. the cantilever is no longer excited mechanically but electrically by applying an *ac* voltage $V_{ac}\sin(w_{ac}t)$ directly to the tip or to the sample. The amplitude of the electrostatic force generated is therefore detected by a lock-in amplifier and is sent through the feedback loop for CPD recording. To understand this, a block diagram representing a typical set-up of the electronic system of during AM-KPFM is shown in Figure 3.15.

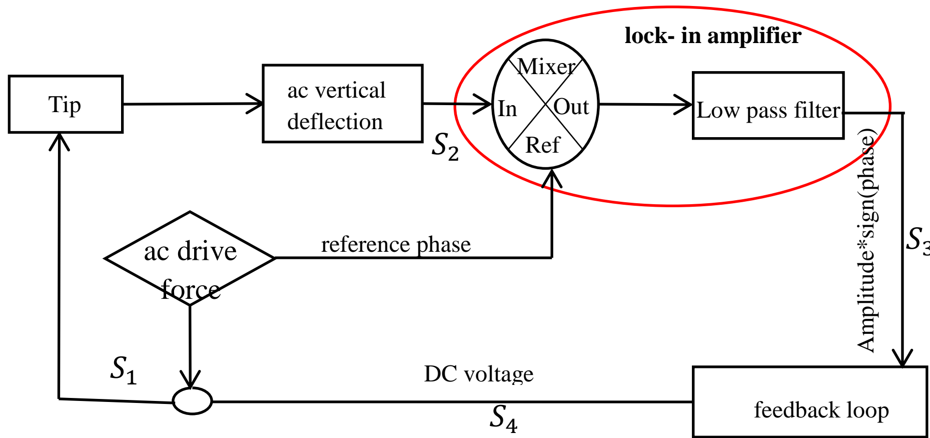

Figure 3.15: Block diagram of an AM-KPFM setup [40]

To elaborate the setup, signals at each stage is labelled as S_1 to S_4 as shown in Figure 3.15. Each of these signals are [69]:

$$S_1: \quad V_{ac} + V_{ac}\sin(w_{ac}t) \qquad 3.42$$

$$S_2: \quad F_{w_{ac}} = -\frac{\partial C}{\partial z}(V_{dc} - V_{CPD})V_{ac}\sin(w_{ac}t + \alpha) \qquad 3.43$$

$$S_3: \qquad F_{w_{ac}} = \frac{\partial C}{\partial z}(V_{dc} - V_{CPD})V_{ac}\cos(\alpha - \beta) \qquad 3.45$$

$$S_4: \qquad V_{dc} \qquad 3.46$$

As shown in this diagram, an external voltage expressed as S_1 is sent to the tip. It can also be applied to the sample. At the same time the *ac* component with reference phase β of this external voltage is also directly sent to the lock-in amplifier. If there is a work function difference (V_{CPD}) between the tip and the sample, this external *ac* voltage will cause the cantilever to deflect. The cantilever deflection with its phase shift α detected by the photodiode (shown as S_2), mixed with the noise from the environment, is sent to the input of the lock-in-amplifier. As described in section 3.1, the lock-in amplifier receives this *ac* signal, measures its amplitude (S_3) and sends it to a feedback loop through the low pass filter. The main role of feedback is to apply a *dc* bias (S_4) to the sample/tip and try to bring the oscillation amplitude (caused by CPD between the tip and the sample) of the cantilever to be zero. As can be seen from S_2, in addition to its amplitude, the signal also contains its phase, $\sin(w_{ac}t + \alpha)$. Hence, the lock-in phase can be adjusted properly, as discussed above.

3.5 Frequency modulation (FM)-KPFM

3.5.1 Theory

Unlike AM-KPFM, where changes in the amplitude of the cantilever oscillation is measured, in FM-KPFM the change in frequency ($\Delta \boldsymbol{f}$) is measured by the system. In this technique, the cantilever-tip is considered as a spring point-mass system, subjected to a damping force [42] that oscillates with a frequency of $f_o = \frac{1}{2\pi}\sqrt{\frac{K}{m}}$.

However, depending on the tip-sample interaction, this frequency can be shifted to lower or higher values as illustrated in Figure 3.16.

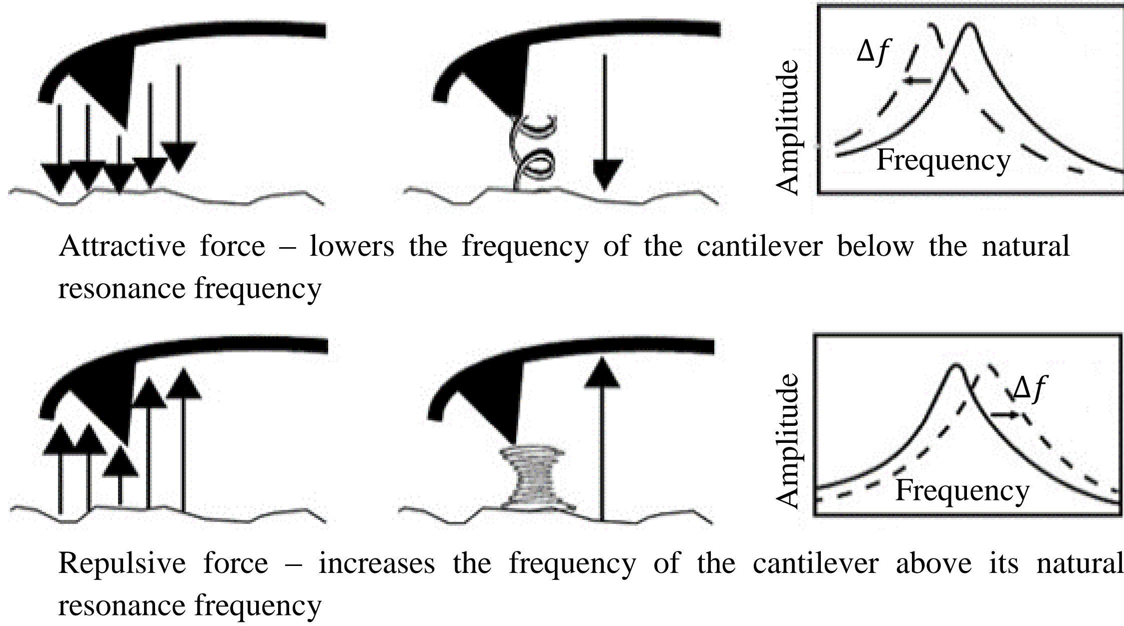

Figure 3.16: The variation in oscillation frequency of the cantilever relative to its natural resonance frequency is determined by the nature of the interaction between the tip and sample [40].

Figure 3.16 shows the change in frequency $\boldsymbol{f}$ of the cantilever in response to any additional force gradient caused by sample-tip interaction [40]. As indicated in the top left side of Figure 3.16, when the tip is far away from the sample, the sample attracts the tip. As a result the resonance frequency of the cantilever decreases. On the other hand, when the tip is too close to the sample surface, as shown in the bottom left in Figure 3.16, the sample repels the tip, causing an increase in the cantilever frequency. Using basic spring-mass theory, the effective spring constant (k_{eff}), which is the sum of the natural cantilever spring constant and the spring constant created by the tip-sample interaction (electrostatic force in this case), can be written as [42]:

$$K_{eff} = K - \frac{\partial F_{w_{ac}}}{\partial z} \quad ; \qquad f_{eff} = \frac{1}{2\pi}\sqrt{\frac{K - \frac{\partial F_{w_{ac}}}{\partial z}}{m^*}} \qquad 3.46$$

Here $\frac{\partial F_{w_{AC}}}{\partial z}$ is the spring constant created by the electrostatic force and f_{eff} the effective resonance frequency; K is the natural spring constant of the cantilever-tip system, *i.e* the spring constant without any tip-sample interaction, and m^* is the mass of cantilever.

Due to the fact that the cantilever is electrically vibrated by an external *ac* source, and the fact that the cantilever responds only to forces applied at/or near its resonance frequency (see section

3.4.1), the tip-sample interaction force F_{ts} of equation (2.2) is replaced by the electrostatic force $F_{w_{ac}}$ between the tip and sample.

As can be seen from equation (3.46), the effective spring constant of the cantilever is no longer constant; likewise its effective resonance frequency. Both of these depend directly on the magnitude of the electrostatic force gradient between the tip and the sample. For small oscillation amplitudes and force gradients, the frequency shift $(f_{eff} - f)$ can be approximated by [57, 67]:

$$\Delta f = f_{eff} - f \approx -\frac{f_o}{2K}\left(\frac{\partial F_{w_{ac}}}{\partial z}\right) \quad 3.47$$

In equation (3.47), the frequency shift is proportional to the electrostatic force gradient. This equation provides a quick and easy way to interpret experimental observations [41]. In addition, details of equation (3.47) can also be used to provide a better understanding of the frequency shift in FM-KPFM measurements. As can be seen from this equation, in the repulsive regime (when the tip is very close to the sample surface), the electrostatic force gradient $\left(\frac{\partial F_{w_{ac}}}{\partial z}\right)$ is negative, which means that Δf is positive in the repulsive regime. Hence, one can deduce that a repulsive force will shift the natural resonance frequency to higher values. In the attractive regime (tip far from the sample), $\frac{\partial F_{w_{ac}}}{\partial z}$ is positive and Δf will be negative. In this case, the natural resonance frequency will be reduced.

From equation (3.41), specifically the second term on the right side, $F_{w_{ac}} = \frac{\partial C}{\partial z}(V_{dc} - V_{CPD})V_{ac}$, the mathematical formula which links the electrostatic force gradient and the frequency shift Δf can be given by:

$$\Delta f \approx \frac{f_0}{2K}\left[\frac{\partial^2 C}{\partial z^2}(V_{dc} - V_{CPD})V_{ac}\sin(w_{ac}t)\right] \quad (3.48)$$

In FM-KPFM the change in frequency $\boldsymbol{\Delta f}$, which is determined by the gradient of the force (not the interaction force itself as in the case of AM-KPFM), is measured by the system. It is also important to note that in FM-KPFM, both the topography image and the CPD measurements are simultaneously obtained in a single-pass (no lift is required). While the deflection of the

cantilever is mechanically generated by a piezo-material to image the surface topography, the amplitude of the frequency shift caused by the tip-sample interaction is used to obtain the CPD. Otherwise, the operational principles of FM-KPFM is similar to that of AM-KPFM. As in the case of AM-KPFM, FM-KPFM also uses a lock in amplifier and feedback loop to measure the CPD. The amplitude of the frequency shift is first measured by the lock-in amplifier and then sent to the feedback loop, where it is minimized by a *dc* compensation voltage ($V_{dc} = V_{CPD}$) for CPD measurements.

3.6 Limitations of AM- and FM- KPFM

KPFM nowadays appears as a most powerful technique used to image the surface potential of a sample. However, measurements performed using this technique can be affected by several physical factors or experimental conditions [43]. In ambient conditions, for example, the value of the measured CPD is influenced by contamination, oxide layers, or trapped surface charges [47]. In fact, the humidity plays an important role on the charging of an insulator [69]. At low humidity (10% relative humidity) the effect of trapped surface charges can be detected in the CPD image [69]. Such charging effects become less prominent at high humidity (80% r.h.) [69]. The value of the measured CPD can also be limited by the bandwidth of the photodiode used for the detection of the cantilever oscillation. In many commercial AFM systems, a photodiode with a bandwidth of $\sim 500\ Hz$ [41] is used. This means that amplitude variations of the oscillating cantilever at frequencies higher than 500 kHz cannot be detected using this technique. In order to increase the sensitivity of the cantilever, the cantilever sometimes needs to be tuned at its second resonance frequency, which is around $6.28f_o$ [67], where f_o is the first fundamental resonance frequency of the cantilever. This means that, for a cantilever with fundamental resonance frequency around 60-100 kHz, the second resonance frequency at around 378-628 kHz cannot be measured using this system. KPFM is also very sensitive to tip-sample distance, tip radius [67] and the geometry of the probe [70]. This is more important for AM-KPFM, where the measurements are realized at a certain lift height, and the tip-sample distance has to be well chosen. The tip should not be too far or too close to the sample surface. If too close, the tip can crash into the sample surface, which results in noisy measurements. However, if the tip is too far from the surface, the resolution will be poorer because the tip will not sense any force from the sample. Furthermore, AM-KPFM is very sensitive to a rough topography also. Any change in the

surface topography, even from bad cleaving, induces significant parasitic variations in the output signal, irrespective of the optimization of the feedback loop gain [43]. In the same way, it has been shown that the *cantilever* surface dominates the local electrostatic interaction when the tip apex is too small [70]. Figure 3.17 displays the effect of probe geometry on CPD measurements. More explicitly, the relative contribution of the tip cone, integrated to a height h, versus total interaction, is plotted for different tip-sample distances against tip height (h) [71].

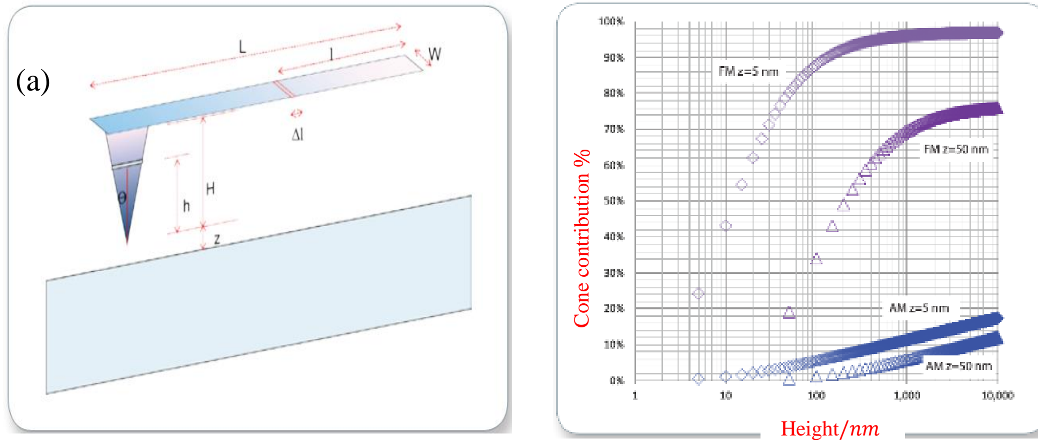

Figure 3.17: (a) SCM-PIT probe modeling with the following nominal probe geometries: $\mathbf{225\ \mu m}$ length (L), $\mathbf{30\ \mu m}$ width (W), tip $\mathbf{10\ \mu m}$ tall (H), and having a cone half angle θ of $\mathbf{22.5^o}$; (b) the contribution of the tip cone integrated to a height h over total electric force (blue) and electric force gradient (purple) are plotted versus height (h). The "blue" plots are the electric force for tip-sample separations of $\mathbf{5\ nm}$ and $\mathbf{50\ nm}$. The "purple" plots are electric force gradients for the same tip-sample separations [71].

In Figure 3.17 (a), it was assumed that the probe is a good conductor, which means that the potential is the same all over the probe, and charges are only distributed on the surface. C. Li *et al.* [71], using Figure 3.17 (b), demonstrated the impact of the geometry of the probe and the tip-sample distance on CPD measurements. As can be seen from this figure, the value of CPD measured depends both on the KPFM mode used and on the tip-sample separation. For AM-KPFM, when the lift height is 5 nm, the contribution of the whole tip cone remains below 50%, indicating its spatial resolution is dominated by the width of the cantilever (on the micrometer scale), also implying that the CPD obtained is not local, but a convolution over the large area covered by the cantilever [71]. Due to the slow decay of the interaction, the force induced by the mesoscopic tip cone and the cantilever will be in most cases greater than the force induced by the small tip apex, even though the latter is much closer to the sample [72]. On the other hand, for

FM-KPFM, at the same lift height above the surface (5 *nm*), the CPD between the tip and sample is almost 100% dependent on the tip cone. Hence, the CPD measured during FM-KPFM is determined primarily by the area right underneath the tip. Therefore, the FM mode probably provides a credible accuracy and better lateral resolution [71]. However, the same figure shows a small variation of the tip cone contribution with tip-sample distance. When the tip is at around $50\ nm$ above the sample surface, the contribution of the tip cone decreases for both AM and FM mode measurements, which demonstrates the strong dependence of spatial resolution on probe-sample distance. Compared to AM-KPFM, where the electric force, proportional to $1/_{z^2}$ is measured [67], the better resolution obtained during FM-KPFM can be explained by the fact that the electric force gradient, which is proportional to $1/_{z^3}$, is measured.

Chapter 4: Experimental Details

This chapter gives a brief description of the experimental method for growing the samples and of the characterization techniques employed. In addition, the SPM system is described and the characteristics of different probes used are also summarized. Finally, sample preparation, including cleaving, mounting and alignment, is briefly described.

4.1 Sample growth characteristics

All the samples used in this study are based on GaAs semiconductor structures grown by atmospheric pressure Metal-organic Vapor Phase Epitaxy (MOVPE). Three different types of structures have been investigated. These are GaAs-based homoepitaxial, heteroepitaxial and quantum well structures. The homoepitaxial structures included *Si*-doped (*n-type)* and *Zn*-doped (*p-type)* degenerate GaAs grown on semi-insulating (SI) GaAs substrate. For these homoepitaxial structures, samples with different electron densities have been chosen. The heteroepitaxial samples include *n-type* $In_xGa_{1-x}As$ grown on SI-GaAs and a 10-period GaAs/AlGaAs quantum well structure, also grown on SI-GaAs. The growth conditions are summarized in table 4.1 below. Details of the growth system have been presented elsewhere [73]. The dopant density (as determined by Hall measurements at room temperature) of each homoepitaxial sample will be given in chapter 5.

Table 4.1 Growth conditions of samples used in this study.

Sample type	V/III ratio	Growth temperature (^{o}C)
n-type GaAs	20	740
p-type GaAs	70	670
n-type InGaAs	50	670
GaAs/AlGaAs quantum wells	90/112	740

4.2 Instrumentation

All electrical and structural properties of the samples presented in this dissertation have been obtained using a Bruker Dimension Icon available in our research group and in the Department of Physics, University of Pretoria. An image of this powerful system is depicted in Figure 4.1.

Figure 4.1: Image of Bruker Dimension Icon

The Bruker Dimension Icon includes several components, such as a Dimension Icon scan head, an optical microscope, an electronic block, a computer etc.... The description and working principles of these components are clearly described in the Dimension Icon Manual [40].

4.3 Analysis conditions and probe properties

All the measurements (using AM or FM mode KPFM) have been performed in air and at room temperature. Regarding the AM-KPFM mode, the measurements have been conducted using SCM-PIT probes with the following nominal characteristics: tip radius $\sim 20nm$, length $200 - 250\mu m$, width $23 - 33\mu m$ and thickness $2.5 - 3.5\mu m$. In addition, a lift height in the range of $50 - 75\ nm$ has been used. Figure 4.2 below shows a scanning electron microscopy (SEM) image of the SCM-PIT probe, obtained from the Bruker website [74]. As can be seen from this figure, the probe consists of two main parts: the tip and the cantilever. The tip apex is the part of the probe that interacts with the sample. The deflection of the cantilever meanwhile is used to quantify the interaction force between the tip and the sample surface. As described in chapter 2 when the tip interacts with the sample surface, the interaction forces between them cause the cantilever to deflect. A photodiode detector measures the deflection of the cantilever and thereafter converts it, electronically, into an image of the scanned surface. For the FM mode,

PFQNE-Al probes with the following nominal characteristics: tip radius ~8 nm, length ~42 μm, width ~40 μm and thickness ~0.3 μm have been used. Unless specified, in both modes an external dc voltage has been applied directly to the tip.

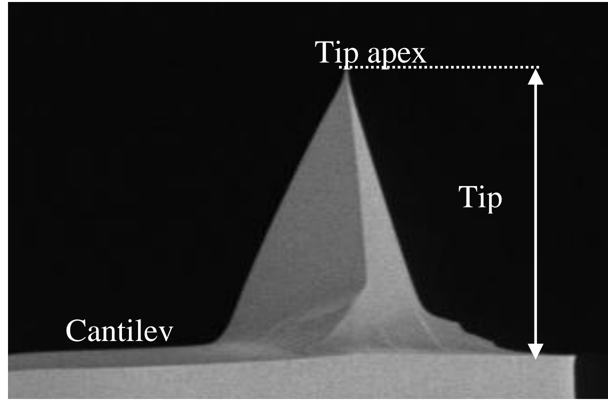

Figure 4.2: SEM image of the SCM-PIT probe downloaded from the Bruker website **[74]**.

4.4 Sample preparation

In all cases the samples were manually cleaved from the back side (using a diamond tip scriber), mounted on a cross-sectional sample holder and investigated within the same day to reduce contamination/oxidation. Figure 4.3 below shows a schematic diagram of (a) a cross-sectional view of: a single layer grown on SI-GaAs and (b) a sample mounted onto the cross-sectional sample holder. The red rectangle indicts the ideal scan area. The scan area was chosen such that both the substrate and the layer can be scanned at the same time with the scan axis perpendicular to the junction. Information regarding the thickness of each layer will be presented in chapter 5.

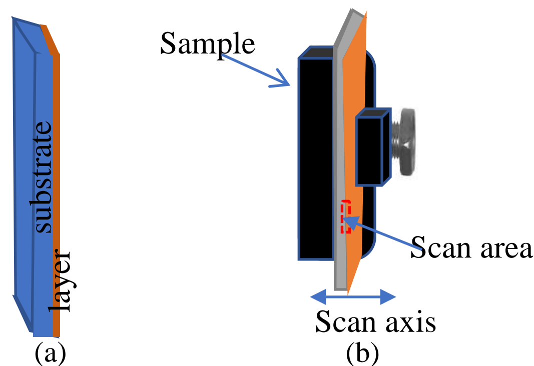

Figure 4.3: (a) Sketch of a cross-section of a sample consisting of a substrate and a single epilayer.
(b) Cross-sectional sample mounted onto the sample holder. The tip scans across the interface.

Chapter 5: Results and Discussion

In this chapter, cross-sectional potential profiles and topography images of GaAs-based III-V semiconductor structures have been investigated. In particular, cross-sectional potential and topography measurements of both *n-type* and *p-type* degenerate GaAs and undoped *n-type* InGaAs, all grown on semi-insulating (SI) GaAs substrate, have been studied. Furthermore, similar studies have been performed on GaAs/AlGaAs heterostructures grown on SI-GaAs. The results performed on *n-type* GaAs and *n-type* InGaAs are presented in section 5.1. In particular, the dependence of the built-in-potential across the homojunction between *n-type* degenerate GaAs epilayers and SI-GaAs substrate (n-GaAs/SI-GaAs) as a function of electron density of the layer is presented. In addition, theoretical simulations of the built-in-potential across the interface are also reported. Section 5.2 presents the results performed on *p-type* degenerate GaAs layers (p-GaAs/SI-GaAs). Finally, section 5.3 presents the results performed on a 10 period GaAs/AlGaAs quantum well structure.

5.1 CPD of *n*-GaAs/SI-GaAs and *n*-InGaAs/SI-GaAs using KPFM

In this section, the studies carried out on n-GaAs/SI-GaAs and n-InGaAs/SI-GaAs, using both AM-KPFM and FM-KPFM methods, are reported. In the case of n-GaAs/SI-GaAs, four samples with difference dopant densities have been considered. These samples, for purpose of discussion, are named sample 1-4 and have room temperature electron densities of $\sim(4.9 \pm 0.98) \times 10^{18}\ cm^{-3}$, $\sim(6.3 \pm 1.2) \times 10^{18}\ cm^{-3}$, $\sim(6.5 \pm 1.3) \times 10^{18}\ cm^{-3}$ and $\sim(6.7 \pm 1.36) \times 10^{18}\ cm^{-3}$, respectively. The uncertainties in these values represent a maximum estimated error in the Hall measurements of 20%. The electron density of the undoped *n-type* InGaAs/SI-GaAs meanwhile, is $\sim(1.0 \pm 0.2)\ \times 10^{17} cm^{-3}$.

5.1.1 CPD of *n*-GaAs/SI-GaAs using AM-KPFM

This subsection contains three parts. In the first part, topography and potential imaging of different areas on the same sample is presented. The second part presents the average potential profiles on a single area, obtained by withdrawing and re-engaging the tip several times, using the same scan parameters. This is followed by a study of the effect of dopant density on the CPD. Figure 5.1 presents cross-sectional (a) topography and (b) potential images of $3\ \mu m$ thick *n*-GaAs/SI-GaAs. The two images were taken at different regions along the interface between the

layer and the substrate. The red curves on the topography and potential images, respectively, are the average scan lines, which indicate the average height and potential across the layer and substrate. The scan size was 6 $\mu m \times 4$ μm.

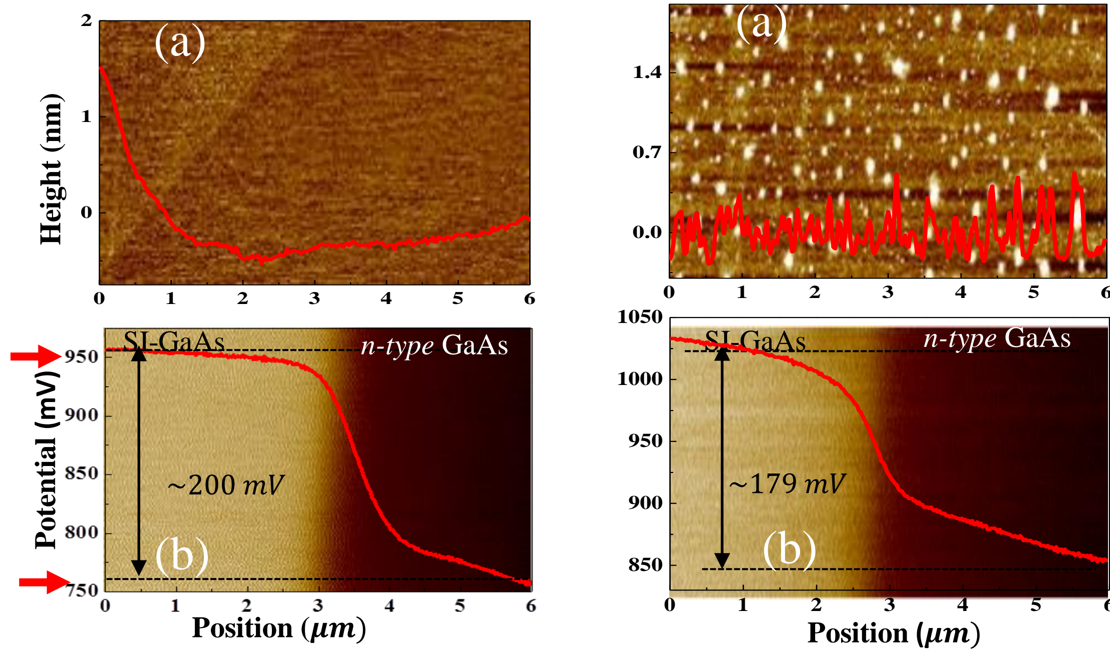

Figure 5.1: Cross-sectional (a) topography and (b) potential images of 3 μm thick *n-type* degenerate GaAs on SI-GaAs substrate, using AM-KPFM. The two images were taken at different regions along the interface of the same sample. The red curves on the topography and potential images, respectively, are the average height and potential across the two different layers. The scan size was 6 $\mu m \times 4$ μm.

As can be seen from both topography images, the homojunction shows a smooth interface between the layer and the substrate. However, the images show different features. It is believed that the features seen on the topography image on the right are introduced during cleaving or contamination during handling. It is also important to note that, after scanning different areas on a freshly cleaved sample, the topography features were found to be different for each. Unlike the case of topography images, however, similar potential profiles have been obtained for both regions. Both potential images in Figure 5.1 illustrate two main regions, related to the difference in electron density between the substrate and layer. It is also important to notice that there is no correlation between the topography and potential, indicating that the choice of scan parameters yielded no cross-talk between topography and potential values. Nevertheless, the values of the CPD of the two areas are slightly different. As shown by the red arrows on the left-hand side of the potential images, a *dc* voltage of ~950 mV was applied during the KPFM measurements

when the tip was on the side of the SI substrate, while a voltage of ~750 mV was applied when the tip was scanning the layer; this gives a CPD of $\sim 200\ mV$. This value is $\sim 179\ mV$ for the second region. To understand this variation in CPD of the two different regions, the potential profile of a single area was measured by engaging and withdrawing the tip several times. Figure 5.2 shows the resulting potential profiles for the sample with the highest dopant density (sample 4).

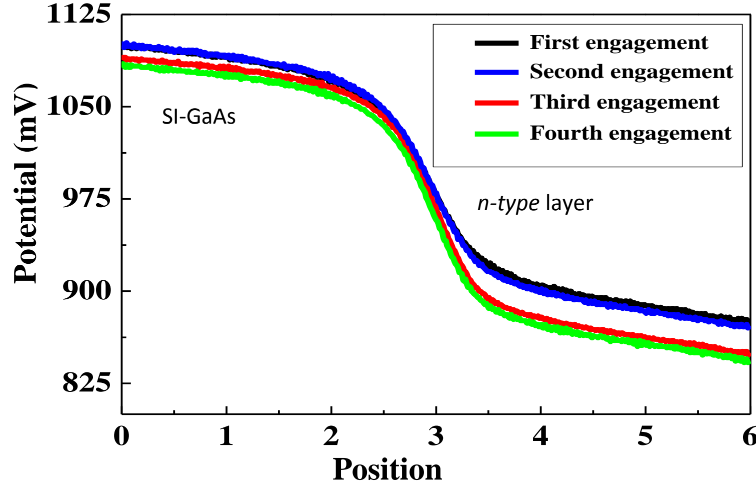

Figure 5.2: Potential versus position of sample 4, repeated four times, at the same spot and with the same parameters.

As can be seen from Figure 5.2 the first two scans are very similar. However, as the number of engagements and withdrawals increases the value of the *dc* voltage reduces on both side, obviously causing changes in the CPD. This is attributed to the deterioration of the tip or to the automatic adjustment of the amplitude setpoint after the tip engages the sample. The values of the *dc* voltage on the substrate side vary from $1100\ mV$ during the first engagement to $1083\ mV$ for the fourth engagement. The uncertainty in the mean measured value for the *dc* voltage on the substrate side, which is given by $\frac{R}{2\sqrt{N}}$, where R and N are the range and the number of measurements, respectively, is estimated to be $\sim 4.25\ mV$. For the same scan lines on the layer side, the error is about $8\ mV$. Therefore, the error propagation in the CPD between the two sides of the junction is found to be $\sqrt{(4.25)^2 + 8^2} \sim 9mV$. Hence, the error in the CPD measured using AM mode will be considered as $\pm 9\ mV$ in the subsequent discussion. The main objective of this subsection is to investigate the effect of dopant density on the CPD by using AM-KPFM. Hence, in the following paragraph, the effect of dopant density on the CPD is presented. Figure 5.3 presents cross-sectional potential and topography profiles of samples 1-4. The red curves on

the topography and potential images, respectively, indicate the average shape of the topography and potential across the different layers.

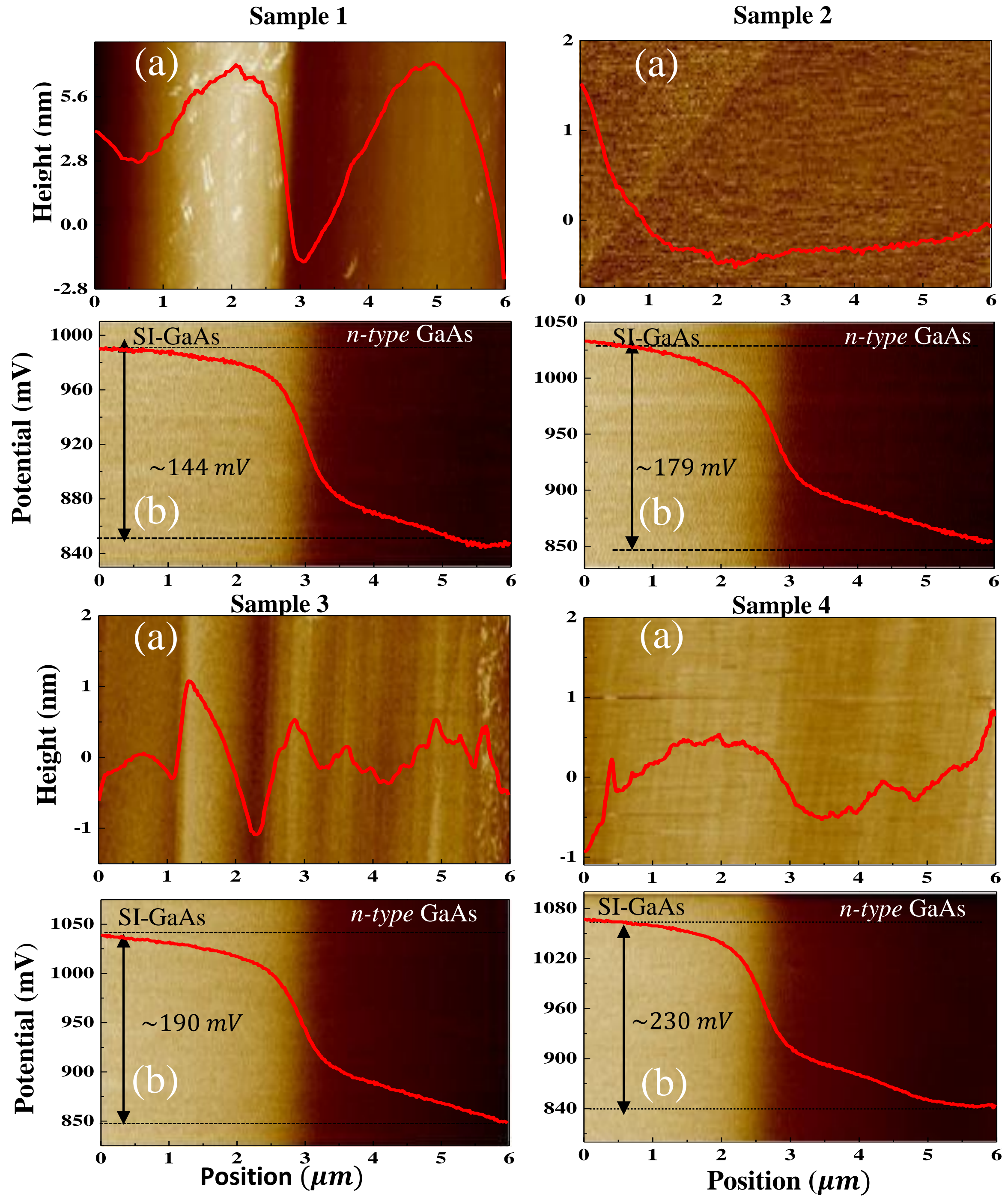

Figure 5.3: Cross-sectional (a) topography and (b) potential maps of **3 μm** thick *n-type* degenerate GaAs grown on SI-GaAs substrate, using AM-KPFM. Four samples with the same layer thickness, but with different electron densities have been investigated. The red curves on the topography and potential images are the average scans lines, which indicate the shape of the topography and potential across the two different layers. The scan size was **6 μm × 4 μm.**

As pointed out above, the topography features vary from sample to sample. Once again, even if each sample has different features, the potential profiles of all four samples look similar and there is no correlation between the potential and topography. However, it can be clearly seen that the CPD varies with dopant density. To better visualize these variations, the average potential scan lines of the four samples have been re-plotted in Figure 5.4. For better comparison, the CPD between the tip and substrate has been adjusted to the same value.

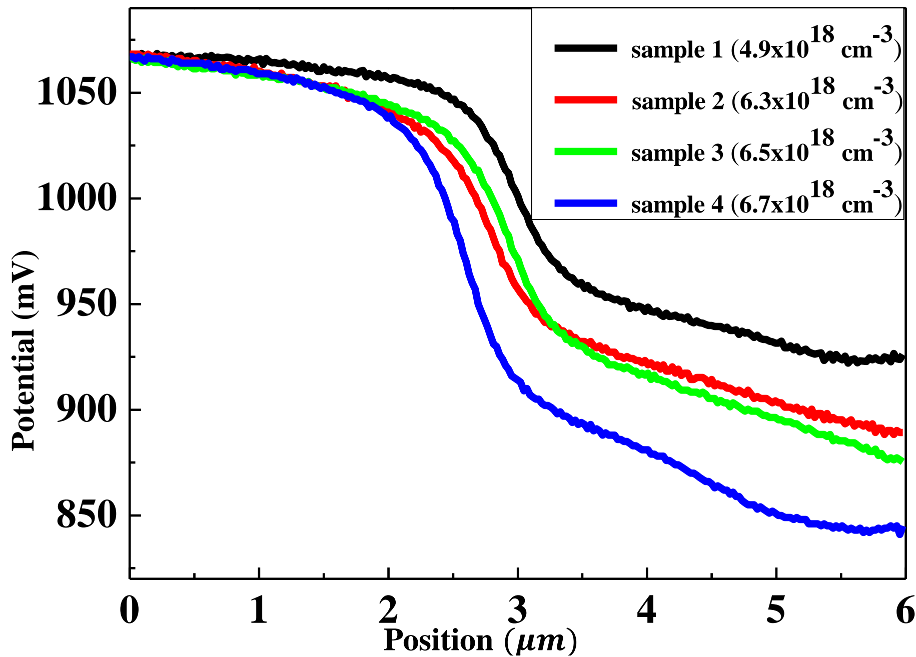

Figure 5.4: Average potential versus position for samples 1-4, obtained by using AM-KPFM.

As can be seen from this figure, the variation in *dc* voltage applied to compensate the CPD between the tip and the layer is significant. This is attributed to the difference in dopant density in the layers.

To better illustrate this, the variation of the CPD across the interface has been plotted versus electron density in Figure 5.5. As mentioned in chapter 4, the value of the electron density of each sample was obtained using Hall measurements.

Regarding the values of CPD for each sample, the calculation has been made from the average potential line scans in Figure 5.3. As indicated by the vertical arrows on each potential versus

position graph, the value of the CPD for each sample was calculated by taking the difference in potential value on the substrate side and the layer side. In principle, to get the CPD between the layer and the substrate, first the CPD between the tip and sample should be calculated. This can be achieved by taking the value of the CPD between the tip and the substrate when the tip is entirely on the SI-GaAs substrate side and doing the same when the tip is entirely on the layer side. These values should be taken far away from the junction, since the aim is to get a true representation of the CPD value on each side of the junction, without the one affecting the other. Then, finally, the difference between the two values equals the CPD between the layer and the substrate.

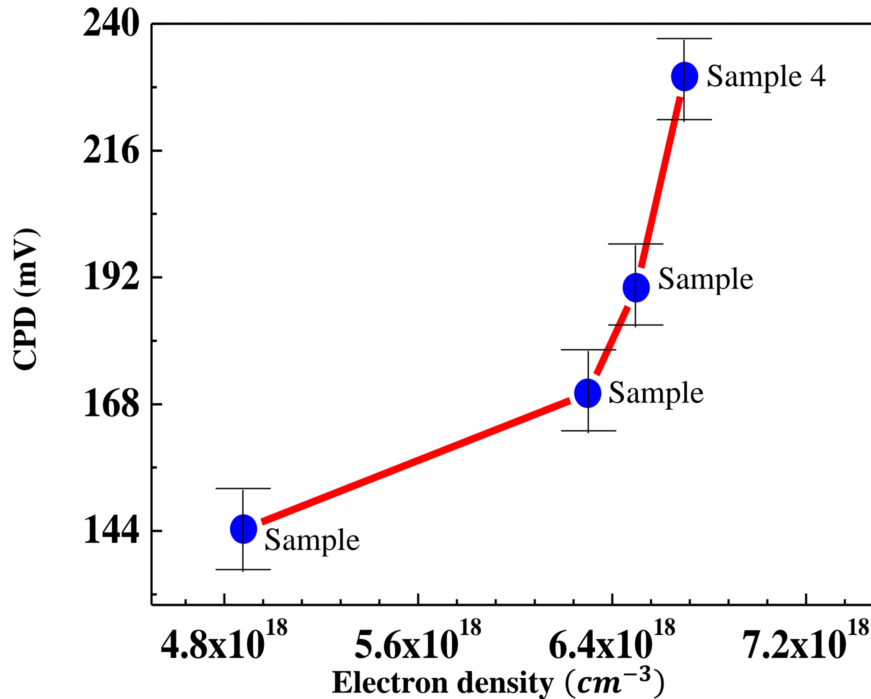

Figure 5.5: Experimental evolution of the CPD across *n-type* GaAs/SI-GaAs versus electron density, using AM-KPFM. Vertical lines are the estimated uncertainties. Four samples with difference electron densities have been used for the investigation.

As can be seen from Figure 5.5 the CPD increases by approximately 90 mV as the electron density increases, which is significant given the estimated uncertainty ($\pm 9\ mV$) in each value plotted here.

In principle, for an ideal GaAs homojunction, the CDP is equal to the Fermi energy level difference between the substrate and the epilayer. Therefore, the change in potential across the interface can be explained by means of the energy band diagrams shown in Figure 5.6 [19].

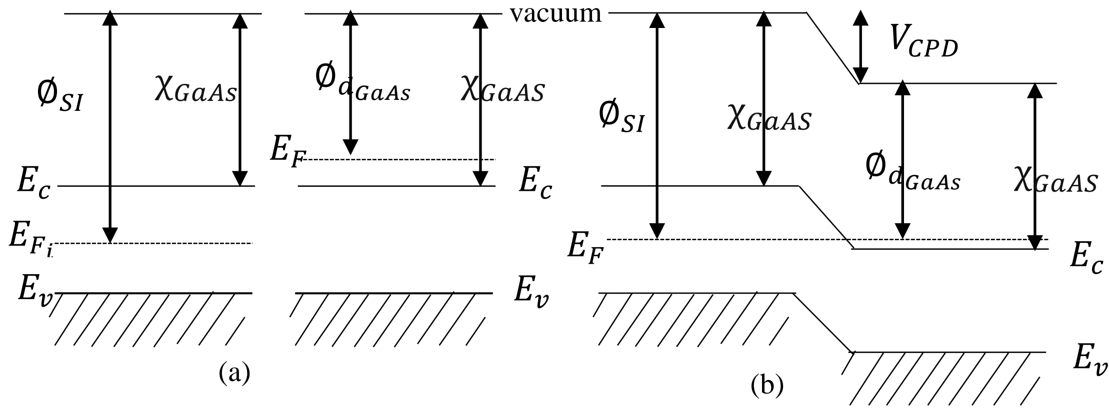

Figure 5.6: Schematic energy band diagrams for ideal semi-insulating and *n-type* GaAs. (a) Before contact, (b) after contact. $\emptyset_{d_{GaAs}}$ **and** $\emptyset_{SI}$ are the work functions of *n-type* degenerate GaAs and SI-GaAs, respectively; $\boldsymbol{E_{F_i}}$ and $\boldsymbol{E_F}$ are the intrinsic Fermi level energy and the Fermi level of *n-type* degenerate GaAs; $\boldsymbol{E_c}$ and $\boldsymbol{E_v}$ are the absolute minimum of the conduction band and absolute maximum of the valence band and $\boldsymbol{\chi_{GaAs}}$ is the electron affinity**.**

Before contact, the two semiconductor materials (substrate and layer) are neutral throughout. After contact, because of the difference in work function, charge flows from the semiconductor with the higher Fermi level to the semiconductor with the lower one until the Fermi levels are aligned. This results in a built-in-potential (CPD) between the two layers and space charge regions on both sides of the interface. To reflect these changes, there is a drop in local vacuum level across the interface (Figure 5.6 (b)) [19]. This band alignment also illustrates the change in potential across the interface between the two layers ($V_{CPD,}$ Figure 5.6 (b)). Hence, one would expect that the CPD across the interface is approximately equal to the Fermi energy or work function difference between semi-insulating GaAs and *n-type* GaAs.

As indicated in chapter 3, the DDSA compensation scheme (described in section 3.2) for SI GaAs puts the position of the Fermi level slightly above (0.038 eV) mid gap. However, as this study was conducted in ambient conditions where the experimental quantities are relative, the position of the Femi level on the SI side was assumed to be pinned approximately at the intrinsic level. On the $n+$ side it is known that as the dopant density increases, the position of the Fermi level also increases, as pointed out in section 3.2.1 (a) (Figure 3.11). Hence, the lower the Fermi energy position of the *n-type* film is (for example, for a sample with a lower electron density), the smaller will be the CPD between it and the substrate, as observed in Figure 5.5. It is important to note that for similar homojunction samples with dopant densities below $\sim(1 \pm 0.2) \times 10^{17} cm^{-3}$, a flat potential across the interface was obtained using both AM- and FM-

KPFM. This is ascribed to the fact that the two Fermi levels (*i.e.* for the substrate and the layer) are too close to each other for the system to detect any difference between them. Based on the fact that KPFM measurements in air is strongly affected by the ambient, this conclusion needs to be further investigated by measurements in vacuum, where absolute values of the CPD can be measured [75].

It should be mentioned that there are significant differences in the values of the theoretically predicted and experimentally observed CPD values. As indicated in subsection 3.2.1 (a), theoretically the CPD versus dopant density can be simulated (using equation (3.20)) by:

$$V_{CPD_{d_{GaAs}}} = \left| \frac{1}{2}\left(E_g - \Delta E_g\right) + kT\left[ln\left(\frac{n}{N_c}\right) + \frac{1}{\sqrt{8}} \times \frac{n}{N_c} - \frac{3}{4} ln\left(\frac{m^*_{h_{GaAs}}}{m^*_{e_{GaAs}}}\right)\right]\right| \quad 5.1$$

For GaAs at room temperature $E_g = 1.424$ eV, $N_C = 4.7 \times 10^{17}\ cm^{-3}$, $\frac{m^*_{h_{GaAs}}}{m^*_{e_{GaAs}}} = 7.07$. ΔE_g is dopant density (*n*) dependent. The calculated CPD values versus dopant density (*n*) are shown in Figure 5.7.

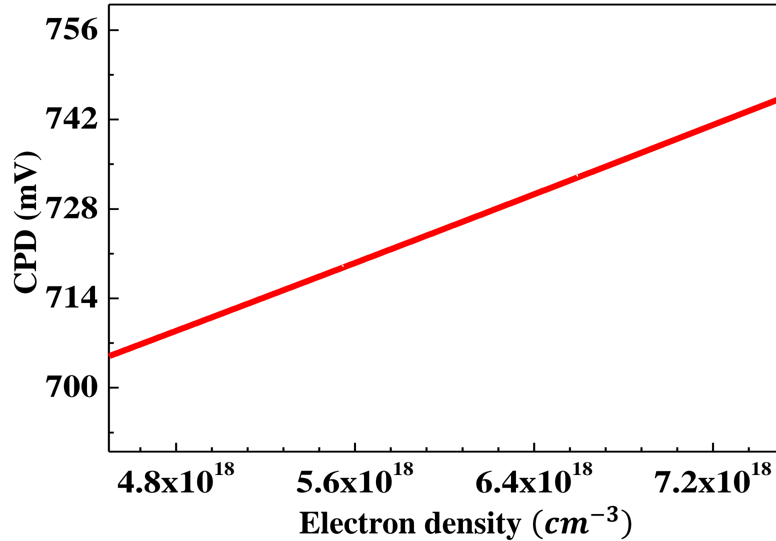

Figure 5.7: Theoretical evolution of the CPD across the *n-type* GaAs/SI-GaAs interface versus electron density.

The calculated CPD values in Figure 5.7 differ strongly from the experimental results in Figure 5.5, presumably due to surface Fermi level modifications cause by the ambient. The change in calculated CPD values (~25 mV) for the rather small electron density variation in the samples studied here, is also smaller than the experimental change of ~90 mV. The agreement between

experiment and theory is qualitative only – *i.e.* an increase in electron density of the film correlates with an increased CPD value.

As pointed out above, the experimental CPD values are much smaller than the calculated values (on average about 25% of the theoretical values). This discrepancy can be attributed to surface traps due to the exposure of the sample to the air, or to incomplete ionization as pointed out by F. Robin *et al.* in [76], where they observed that the built-in-potential measured in air across a cleaved p-i-n laser diode, was around 40% of the simulated values. In addition, this discrepancy can also be explained by the shape of SCM-PIT cantilever used to perform the current AM-mode measurements. Due to its larger length, width and tip radius compared to the PFQNE-Al probe used for FM-mode measurements and discussed in the next section, the CPD values measured are not truly local but rather a convolution over the large area covered by the cantilever. This means that when the tip is scanning across the junction, the potential measured is probably a convolution of that of the substrate and that of the layer.

5.1.2 CPD of *n*-GaAs/SI-GaAs using FM-KPFM

As described in chapter 3, unlike the case of AM mode KPFM where the electrostatic force is monitored, in FM mode KPFM the electrostatic force gradient [67], which is more confined to the apex of the tip, is detected. Therefore, by using this mode, a higher lateral resolution and more accurate CPD values are expected [75].

As in the case of AM mode, the CPD of four samples (samples 1-4) have been measured using FM-KFPM. It is important to be reminded that it is difficult to exactly scan the same spot using both methods. However, after scanning along the interface of a single sample a similar potential profile to the one obtained using AM-KPFM, has been achieved. In addition, using the same procedure used in AM-KPFM above, an uncertainty of $\pm 5\ mV$ has been obtained.

Figure 5.8 shows a cross-sectional topography and potential profile of samples 1-4. As can be seen from this figure, similar to AM mode scans, the topography of each of the samples is different, whereas the potential profiles are all similar. Two different regions are evident: one with a higher potential (SI-GaAs) and another one with a lower potential (*n-type* GaAs). It is also important to notice that there is no cross-talk between the topography and potential profiles.

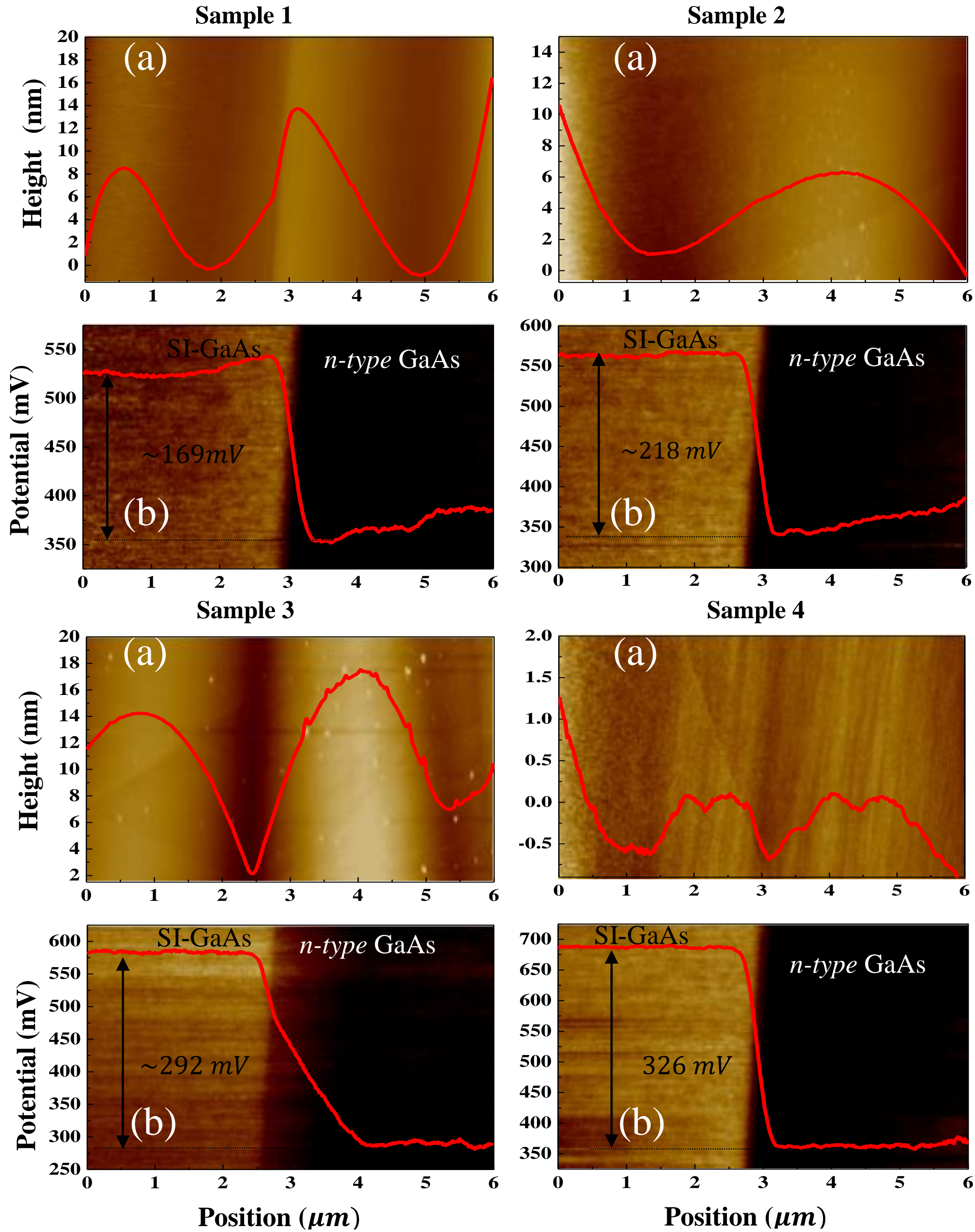

Figure 5.8: FM-KPFM scans of cross-sections of samples 1-4: (a) topography and (b) potential. Four GaAs/SI-GaAs samples with same the layer thicknesses (~3 μm), but with different electron densities have been investigated. The red curves on the topography and potential images, respectively, are the average scan lines, which indicate the shape of the topography and potential across the two different layers. The scan size was $\mathbf{6\ \mu m \times 4\ \mu m}$.

As both topography and potential measurements are collected in a single pass (no lift is required) in FM-KPFM, potential profiles usually suffer from cross-talk from the topography, which can be avoided using proper initialization of the scan parameters during the measurement. As indicated in these potential line scans, the two regions are clearly visible, indicating that FM is quite superior to AM even in ambient conditions. In addition, the transitions across the interfaces are sharper and the surface potential flattens far away from each interface.

To compare the lateral resolution of the two methods, the potential line of each sample obtained by using both AM and FM modes have been simultaneously plotted and studied. The case of the sample with the highest dopant density (sample 4) is shown in Figure 5.9 (a). As can be seen from this figure, the resolution of the FM is quite superior than that of the AM mode. As indicated in section 3.2, n^+/SI junctions do not have a depletion region on the SI side and the electric field cannot be described by that of conventional p-n junctions. For the sake of comparing the two methods, the electric field curves shown in Figure 5.9 (b) were estimated by taking the first derivative [3] of the potential curves shown in Figure 5.9 (a). As shown, the electric field is symmetric in both cases and exists in a region of ~600 nm in width (see the dotted vertical lines in the potential and electrostatic field graphs) for FM-KPFM. In the case of AM-KPFM the electric field apparently extends over more than 2 μm. As indicated in Figure 3.5 however, the electric field is un-symmetric and the space charge region extends up to 1000 nm into the SI side. It is also important to point out that the FM mode gives a more realistic value, but the symmetry of the electric field displayed in Figure 5.9 (a) is not in line with the theory of n^+/SI junctions. Therefore, the objective of Figure 5.9 (b) is simply to compare the two methods.

Furthermore, as the potential is constant far away from the junction, the electrostatic field measured using both modes are zero. However, the magnitude of the potential and electrostatic field is larger in the case of FM-KPFM: An electrostatic field of $\sim 234\, mV/\mu m$ and $\sim 1035\, mV/\mu m$ have been obtained across the homojunction for AM mode and FM mode (Figure 5.9 (b)), respectively.

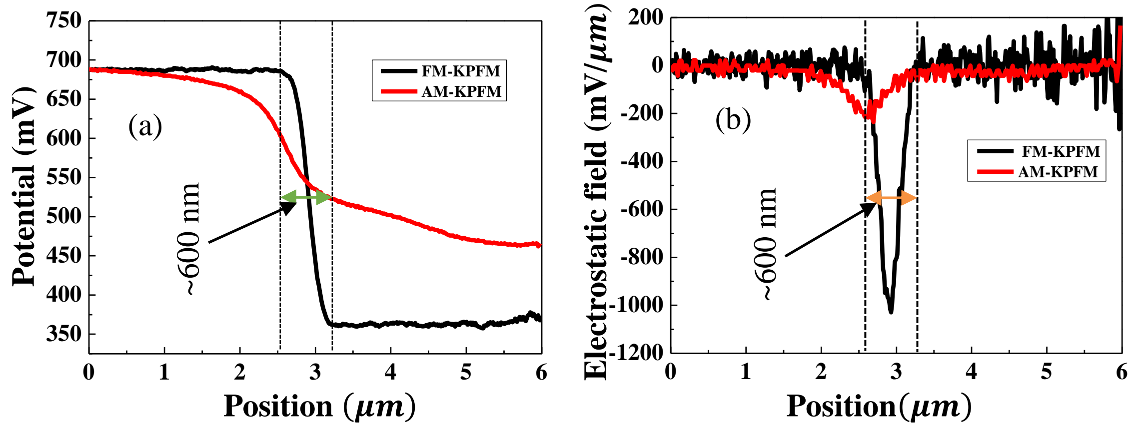

Figure 5.9: AM versus FM mode KPFM: (a) average potential line and (b) Electrostatic field of the sample with the highest dopant density (sample 4). The electrostatic field has been calculated by taking the first derivative of the potential profile. A sharper transition is obtained with FM mode than AM-KPFM mode.

Based on these observations, one can conclude that FM mode KPFM provide higher lateral resolution [67] than AM mode and consequently a more accurate CPD value [75]. As mentioned in section 3.6, this is directly linked to the probe geometry. Because of the larger decay length of F_{el}, AM mode KPFM suffers from poor spatial resolution so that quantitative CPD values can only be expected for larger homogenous sample regions [67]. Quantitative results can only be obtained with the FM mode of measurement [67]. It is important to indicate that the calculation of the depletion width or electric field for such a n^+/SI junction, using convectional *p-n* junction theory, is misleading. In fact, even using the expression for the depletion width for the convectional *p-n* junction ($w = \sqrt{\frac{2\varepsilon}{q}\left(\frac{1}{N_D}+\frac{1}{N_A}\right)V_d}$, which can be further simplified (for $N_D \gg N_A$) to $w = \sqrt{\frac{2\varepsilon}{q}\left(\frac{1}{ni}\right)V_d}$) the value is found to be 13 mm. In this calculation, $N_A = n_i \sim 1 \times 10^{12}\ m^{-3}$, $N_D = 6.7 \times 10^{24}\ m^{-3}$, $q = 1.6 \times 10^{-19}\ C$, $\varepsilon = 8.54 \times 10^{-12}\ F.m^{-1}$, dielectric constant of GaAs is $N_A = 12.9$ and $V_d = 0.6\ V$ were used.

The four potential profiles measured for the samples are plotted together in Figure 5.10. Again, the potential on the substrate side was adjusted to the same value for each profile.

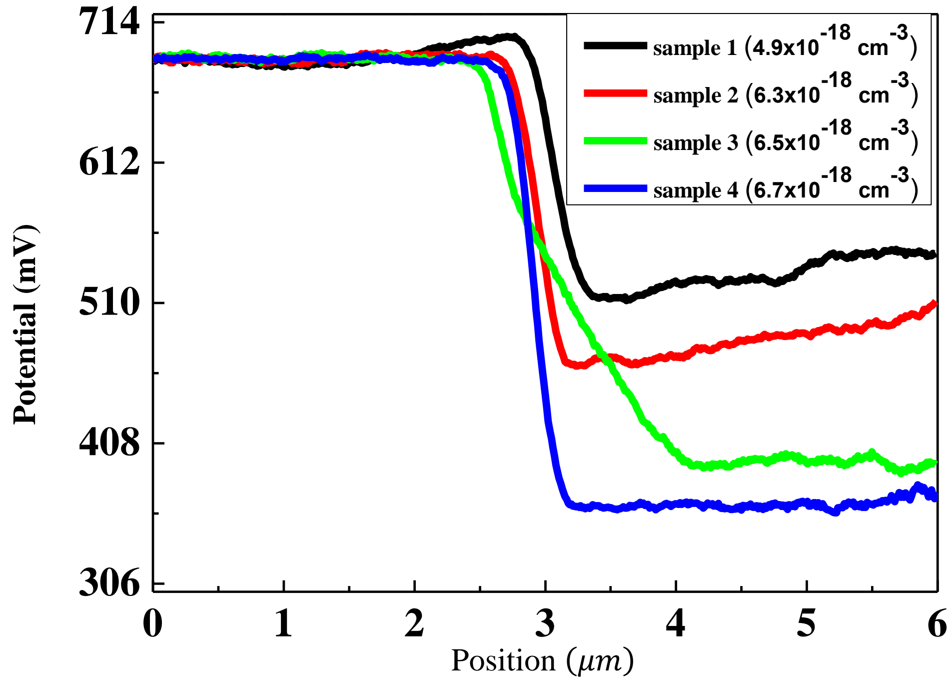

Figure 5.10: Potential versus position for samples with different dopant density, using FM-KPFM method. The potential along the substrate side is adjusted to the same value.

As in the case of the AM-KPFM, the potential along the *n-type* side varies with the dopant density. For example, there is $\sim 160 mV$ CPD difference between that of the sample with the lowest dopant density (black curve) and the one with the highest dopant density (blue curve). This is attributed to the increase in the Fermi energy level position relative to the intrinsic Fermi energy of the substrate with dopant density, as described in Figure 5.6.

The variation of the CPD with dopant density is summarized in Figure 5.11. It clearly shows the change in CPD across the interface between the substrate (semi-insulating) and the layer (*n-type*). Vertical error bars ($\sim \pm 5\ mV$) represent the estimated uncertainty in the CPD-values.

As pointed out for the AM mode analysis the values were calculated by taking the difference of the potential on the substrate and layer side. As in the case of AM mode, the FM mode analysis also reveals an increase in the CPD across the homojunction between the semi-insulating substrate and an *n-type* layer with electron density.

Except for the fact that the CPD values obtained by FM-KPFM are larger than the values obtained using AM-KPFM, the evolution of the CPD versus electron density is similar for both

modes. Compared to the case of AM mode analysis, where the experimental values were on average ~25% of the theoretical values, the CPD values from FM mode analysis are on average ~35% of the theoretical values (see Figure 5.7).

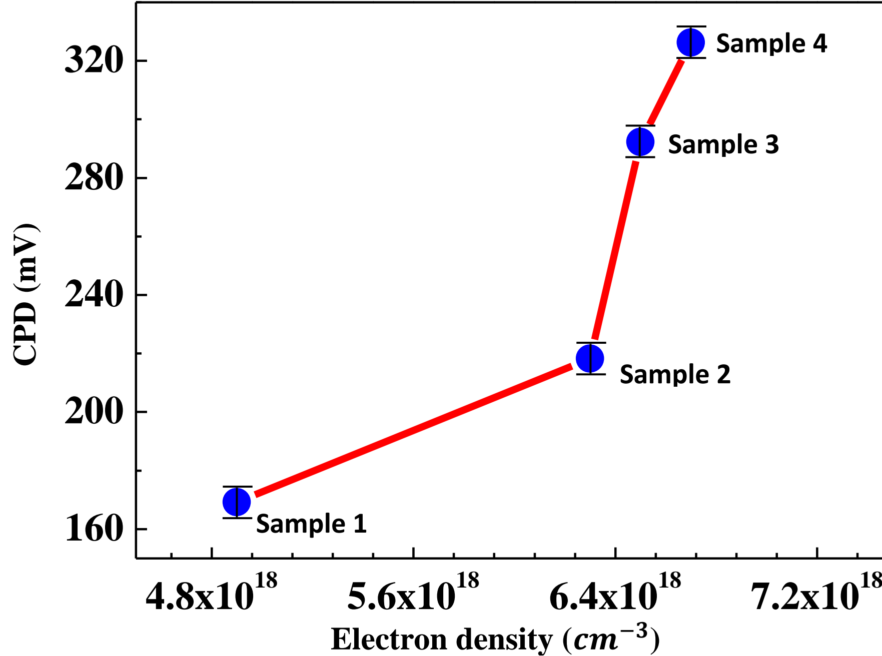

Figure 5.11: Experimental evolution of the CPD across *n*-GaAs/SI-GaAs versus electron density, using FM-KPFM method. The line is a guide to the eye.

Hence, one can conclude that even though the CPD values measured using both modes are smaller than the theoretical values, they can be used to distinguish differences in the built-in potential across the interface between two semiconductors, resulting from different dopant concentrations.

It is also important to note that for the two modes (AM and FM) the changes in measured CPD values are much larger than the 25 mV predicted theoretically for the electron density range of $4.9 \times 10^{18} cm^{-3}$ to $6.7 \times 10^{18} cm^{-3}$. This discrepancy can partly be attributed to inaccuracies in the measurements of the electron densities (*i.e.* uncertainties in the Hall measurements) considered for these studies. If one subtracts 20% from the electron density measured for the sample with the lowest electron density ($i.e. 3.9 \times 10^{18} cm^{-3}$) and add 20% to the one with the largest value ($i.e. 8.0 \times 10^{18} cm^{-3}$), the range of CPD values predicted theoretically increases from 25 mV to 60 mV, which is closer to the range of ~160 mV from FM mode measurements, but still significantly smaller.

5.1.3 CPD measurement of *n*-InGaAs/SI-GaAs using AM- and FM-KPFM

In this subsection, the study on the CPD at the hetero-interface of n-$In_{0.17}Ga_{0.83}As$/SI-GaAs is presented. Unlike the case of the homojunction n-GaAs/SI-GaAs, where the results obtained using AM and FM modes were discussed separately, results obtained using the two different modes are presented simultaneously below.

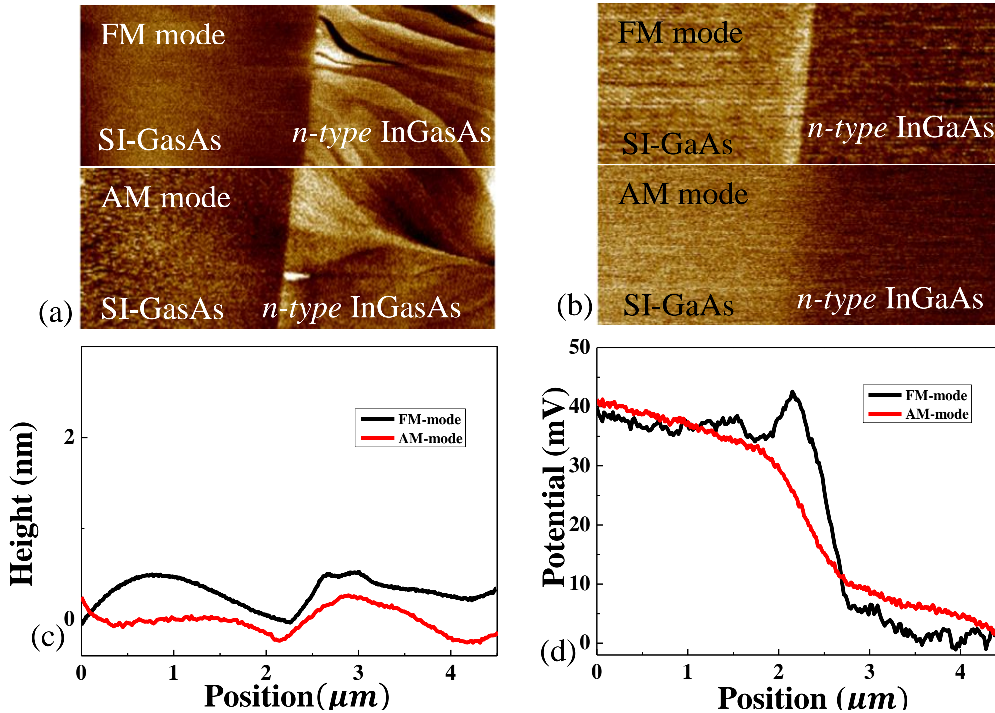

Figure 5.12: Cross-sectional (a) topography and (b) potential images of $5\ \mu m$ thick *n-type* $In_{0.17}Ga_{0.83}As$ single layers grown on SI-GaAs, using both AM and FM mode KPFM. The upper part (potential and topography, respectively) has been recorded with FM mode KPFM and the lower part with AM mode KPFM. Average scan lines for topography and potential profiles are depicted in (c) and (d), respectively. A larger contrast and a sharper transition are obtained with FM mode than with AM mode KPFM, (b) and (d) respectively.

Figure 5.12 shows topography images (a) and potential profiles (b) in which the upper and lower halves depict results obtained using FM- and AM-KPFM results, respectively. As in the case of the homojunction discussed above the features on the two topography images are different, especially on the layer side. However, both images clearly indicate the interface between the substrate and epilayer. A height difference of around $0.49\ nm$ and $0.54\ nm$, using AM and FM mode, respectively, is observed at the junction and suggested to be caused by cleaving the hetero-epitaxial structure (Figure 5.12 (c)).

As can be seen from the profiles in Figure 5.12 (d), for both analysis modes the average potential on the layer side is lower than on the substrate side, because the Fermi energy position in the

epilayer is higher than in the SI-GaAs substrate. In addition, the width of the depletion region appears to be $\sim 0.38\ \mu m$ for FM mode, while for AM mode it is ~2 μm and the potential does not saturate. A similar observation has been noted during the measurements conducted on the n-GaAs/SI-GaAs homojunction. The CPD values extracted from this figure are very similar: $\sim 38\ mV$ and $\sim 33\ mV$ from FM and AM mode analysis, respectively. All these results confirm once again the capability of FM mode KPFM to provide a better lateral resolution and more accurate CPD values than AM mode KPFM. However, even here, the CPD values measured are much smaller than the theoretical value, which is $\sim 540\ mV$. This discrepancy can be attributed (as mentioned in section 3.5) to external factors such as probe geometry, surface traps or incomplete ionization.

5.2 CPD measurement of *p*-GaAs/SI-GaAs using FM-KPFM

In this section, cross-sectional topography and potential imaging of p-type GaAs with a hole density of $\sim (1.79\ \pm 0.36) \times 10^{19}\ cm^3$, grown on semi-insulating GaAs substrate, has been investigated by using FM mode KPFM. The results of these studies are reported in Figure 5.13.

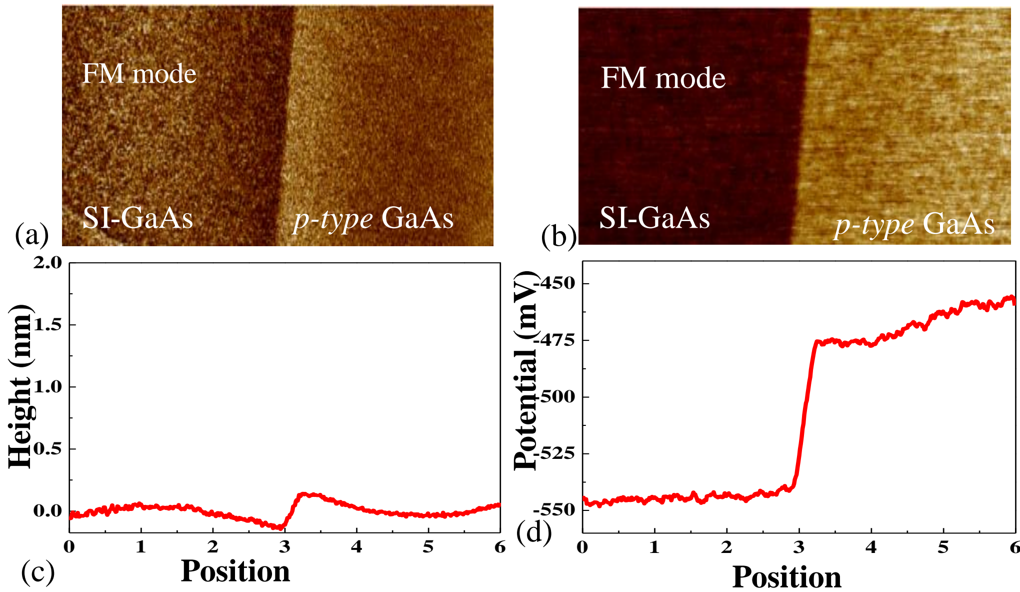

Figure 5.13: Cross-sectional (a) topography and (b) potential images of a $\mathbf{4.8}\ \boldsymbol{\mu m}$ *p-type* GaAs single layer grown on semi-insulating GaAs, obtained using FM-KPFM. Average scan lines for topography and potential profiles are depicted in (c) and (d), respectively.

A smooth surface topography is observed in Figure 5.13 (a), while the surface potential image in Figure 5.13 (b) shows two distinct regions arising from the difference in free carrier density

between the substrate and layer. Regarding the surface topography image, an interface with a height difference of $0.24\,nm$ (Figure 5.13 (c)) has been observed across the junction and is suggested to be due to cross-talk [75] between the topography and potential signal. As it is a homojunction a smooth surface topography image showing no height difference across the junction was expected. Hence, further investigations of this sample are required in the future. The only significant difference between the surface potential images and profiles obtained for *n-type* and *p-type* GaAs epilayers is that relative to the substrate, the potential is lower on the epilayer side in the former case and higher in the latter case. The value of the CPD across the homojunction (with width in the range of $0.4\,\mu m$) is estimated to be $\sim -89\,mV$ (*i.e.* negative). This is highlighted by the scan line in Figure 5.13 (d). This negative sign of the CPD is attributed to the difference in work function of the tip relative to the *p-type* GaAs, which is opposite to the case of n-GaAs. When scanning a p-GaAs/SI-GaAs sample, electrons flow from the tip to both the substrate and the epilayer. This flow of electrons creates a positive charge on the tip and a negative charge on the sample. Therefore, as the *dc* bias is directly applied to the tip, the feedback loop must apply a negative *dc* voltage to the tip to cancel the tip-sample contact potential resulting from the work function difference between the tip and sample (Figure 5.13 (d)).

5.3 CPD measurement of 10 period GaAs/AlGaAs quantum well structure

In section, cross-sectional topography and potential imaging of AlGaAs/GaAs heterostructures with an AlAs mole fraction of 0.35 in the AlGaAs layers is investigated, using both AM and FM mode KPFM. A schematic representation of this sample is depicted in Figure 5.14.

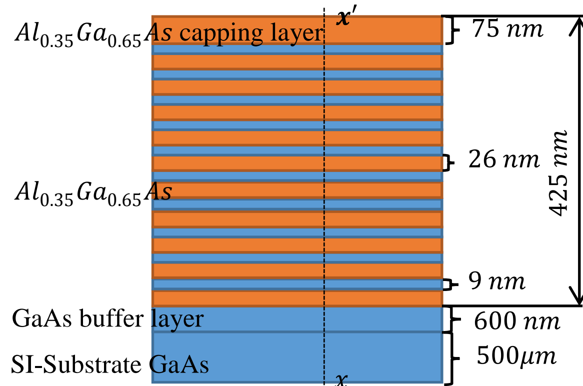

Figure 5.14: Schematic representation of GaAs/AlGaAs multiple quantum wells used for measurements.

As can be seen in Figure 5.14, the sample includes 10 GaAs quantum wells sandwiched between AlGaAs barrier layers. The thicknesses of GaAs and AlGaAs were $\sim 9\,nm$ and $\sim 26\,nm$, respectively. In addition, the thickness of the GaAs buffer layer was $\sim 600\,nm$. The structure was capped with $\sim 75\,nm$ AlGaAs. All the layers were undoped. The topography and potential profiles along the xx' line of Figure 5.14 are shown in Figures 4.15 (a)-(d).

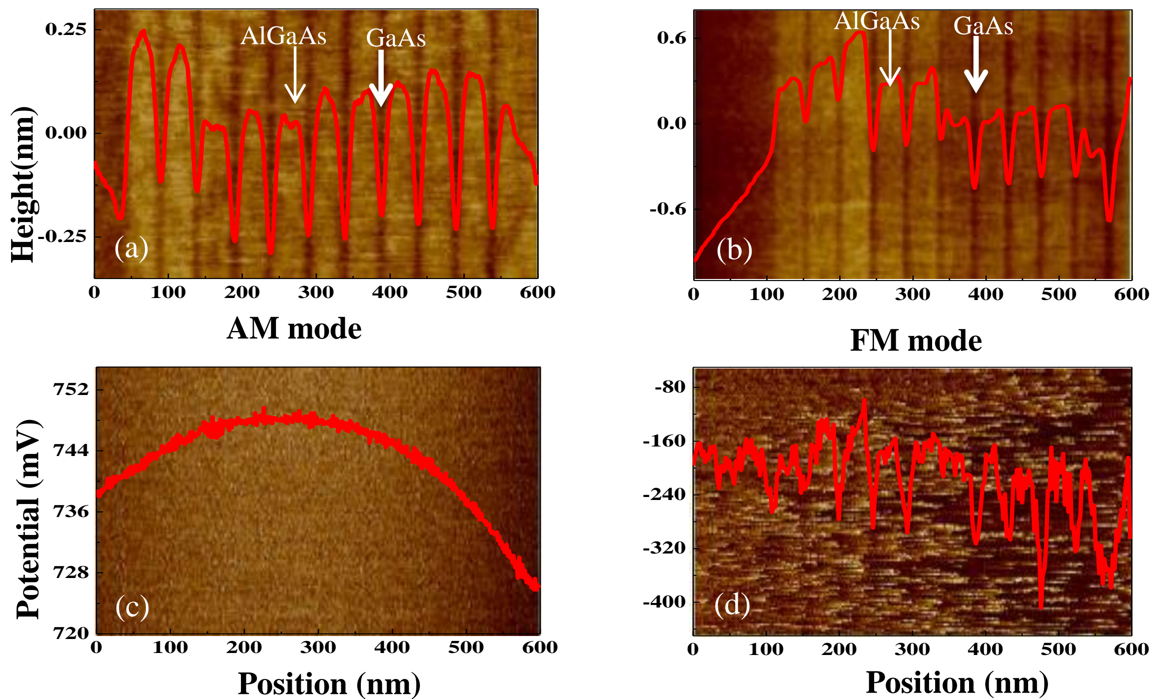

Figure 5.15: Cross-sectional (a,b) topography and (c,d) potential images of GaAs/AlGaAs heterostructure, obtained using both AM and FM mode KPFM. The left-hand side (topography and potential, respectively) has been recorded with AM mode KPFM and the right-hand side with FM mode.

The topography images in Figure 5.15 (a) and (b) clearly show 10 GaAs quantum wells embedded in the AlGaAs matrix. The AlGaAs layers are $\sim 0.3\,nm$ and $\sim 0.5\,nm$ higher than the GaAs layers, depending on the mode used for imaging. This is attributed to oxidation of the AlGaAs following cleaving. In fact, this feature has been obtained by scanning the sample $24\,H$ after the cleaving process. Similar studies of a freshly cleaved sample yielded a smooth surface topography showing no periodic height variation. Therefore, the periodic difference in height in Figure 5.15 can be attributed to the interaction between atmospheric oxygen and the aluminum contained in AlGaAs.

However, no potential difference (unlike the case of *n-type* GaAs/SI-GaAs homojunctions) was observed across the interfaces (Fig 5.15 (c)). This is speculatively attributed to a combination of the probe size and the mole fraction of the AlAs (0.35 in this case) contained in AlGaAs matrix. It has been reported that the CPD between GaAs and AlGaAs increases linearly with AlAs mole fraction [77]. CPD values $\sim 120 - 180\ meV$ (measured in air) have been reported for an AlAs mole fraction of 0.8, while the CPD between GaAs and AlGaAs with AlAs mole fraction of 0.3 was reported to be zero [13]. The small variation in potential (Figure 5.14 (d)) obtained using FM mode is ascribed to the cross-talk between the topography and the potential.

Chapter 6: Conclusions and outlook

In this study, the built-in potential across the interfaces of GaAs-based homojunctions, heterojunctions and quantum well structures, all grown by atmospheric pressure Metal-organic Vapor Phase Epitaxy (MOVPE), has been investigated. The measurements have been performed by using amplitude modulation (AM) and frequency modulation (FM) modes of KPFM, in air and at room temperature.

The homoepitaxial structures included Si-doped (*n-type*) and Zn-doped (*p-type*) degenerate GaAs layers grown on semi-insulating GaAs substrate. For the *n-type* GaAs, four samples with different electron densities were analyzed. The potential profile between each layer and the substrate was measured using both AM and FM modes. In both cases the potential profiles of all the samples indicated two main regions, related to the difference in electron density between the substrate and the epilayer. The study indicated that the CPD between the tip and semi-insulating substrate is higher than that of the CPD between the tip and the *n-type* epilayer, which implies that the Fermi level of the epilayer is higher than that of the semi-insulating side. This change in CPD across the interface has been explained by considering the Fermi energy alignment across the interface. In addition, it has also been found that the magnitude of the CPD across the interface increases with electron density. This result is in qualitative agreement with the theory.

In addition, as is well known in literature and also indicated in this study, under ambient conditions FM mode KPFM provides better lateral resolution and more realistic CPD values than AM mode KPFM. Compared to the case of AM mode analysis, where the experimental CPD values on average were $\sim 25\%$ of the theoretical values, the CPD values from FM mode were on average $\sim 35\%$ of the theoretical ones. Furthermore, by using this mode, the transitions across the interface were sharper and the surface potential flattened far away from the junction. The non-neutral space charge region, which mainly extends to the SI side of the sample with an electron density of $\sim 6.7 \times 10^{18} cm^{-3}$ for example, was $\sim 0.6\, \mu m$ as measured by FM-KPFM, whereas for AM-KPFM, the width was more than $3\, \mu m$; also, the potential profiles did not flatten within the range of the scan (~ $3\, \mu m$ away from the interface).

For the *p-type* GaAs homoepitaxial structures, only one sample has been measured using FM mode KPFM. As in the case of *n-type* GaAs, a similar potential profile showing two main

domains has been obtained. Nevertheless, unlike the case of *n-type* GaAs where the potential measured on the epilayer side was lower than that on the substrate side, an opposite result has been obtained for *p-type* GaAs homoepitaxial structures. Here, the potential on the epilayer side was higher, indicating that the Fermi level of the *p-type* layer is lower than that of the substrate.

The heteroepitaxial structures investigated included *n-type* InGaAs grown on SI-GaAs and a 10-period GaAs/AlGaAs quantum well structure, also grown on SI-GaAs. Regarding the *n-type* InGaAs structures, the potential profile resembled that of the *n-type* GaAs homojunction. By using FM mode KPFM, a non-neutral space charge region of width $\sim 0.38\ \mu m$ has been found, while for AM mode KPFM the non-neutral space charge width was more than $3\ \mu m$; again, the potential did not saturate. The topography image of the GaAs/AlGaAs quantum well structure clearly showed 10 GaAs quantum wells embedded in the AlGaAs matrix. This feature was attributed to oxidation of the AlGaAs surfaces following cleaving. However, no CPD could be measured across the interfaces. This is speculatively attributed to a combination of the tip radius and the rather low mole fraction of the AlAs (0.35 in this case) contained in the AlGaAs matrix.

Suggestions for future work

Because of the fact that the CPD measurements in this study were performed under ambient conditions, the values obtained were qualitative. Therefore, for a better understanding of the interfaces and to obtain accurate values of the built-in potential, the measurements have to be conducted in high vacuum. Furthermore, complementary studies on adsorbed surface species like O, OH and C, using surface sensitive techniques like X-ray photoelectron spectroscopy and Auger electron spectroscopy should be conducted to try and link the CPD values with surface Fermi level pinning.

References

[1] Z. Mi, Y. Chang, "III-V compound semiconductor nanostructures on silicon: Epitaxial growth, properties, and applications in light emitting diodes and lasers," *J. Nanophotonics.,* vol. 3, p. 031602, 2009.

[2] Q. Gao, H. Tan, H. Jackson, L. Smith, J. Yarrison, " Growth and properties of III–V compound semiconductor heterostructure nanowires," *Semicond. Sci. Technol.,* vol. 27, p. 059501, 2012.

[3] S. Kasap, P. Capper, Springer hand book of electronic and photonic materials, Springer, p. 527, 2006.

[4] M. P. C. M. Krijn, "Heterojunction band offsets and effective masses in Ill-V quaternary alloys," *Semicond. Sci. Technol.,* vol. 6, p. 27, 1991.

[5] https://en.wikipedia.org/wiki/Gallium_arsenide#cite_note-Moss-2, "Gallium arsenide," 02-09-2016.

[6] A. Szerling, P. Karbownik, K. Kosiel, J. K. Traczyk, E. P. Karbownik. M. Pluska and M. Bugajski, "Mid-Infrared GaAs/AlGaAs Quantum Cascade Lasers Technology," *Acta Phys. Pol., A,* vol. 116, p. S-45, 2009.

[7] H. Hasegawa, "Formation and Quantum Device Applications of III-V Compound Semiconductor Nanostructures," *J. Korean. Phys. Soc.,* vol. 39, p. 402, 2001.

[8] G. Whitesides, "Galllium asernide: Key to faster, better computing," 1988.

[9] H. Morkoc, "Potential applications of III-V nitride semiconductors," *Mater. Sci. Eng., B,* vol. 43, p. 137, 1997.

[10] H. Hayashi, "Development of Compound Semiconductor Devices— In Search of Immense Possibilities," *Sei Technical Review,* vol. 72, p. 4, 2011.

[11] A. Huijser, J. Vanlaar, T. Vanrooy, "Electronic surface properties of uhv-cleaved III–V compounds," *Surf. Sci.,* vol. 62, p. 472, 1997.

[12] T. Usunami, M. Arakawa, S. Kishimoto, T. Mizutani, T. Kagawa, H. Iwamura, "Cross-Sectional Potential Imaging of Compound Semiconductor Heterostructures by Kelvin Probe Force Microscopy," *Jpn. J. Appl. Phys.,* vol. 37, p. 1522, 1998.

[13] H. Wang, H. Yu, X. Zhou, Q. Kan, L. Yuan, W. Chen, W. Wang, Y. Ding, J. Pan, "Higher-power InGaAs/GaAs quantum laser with enhanced broad spectrum of stimulated emission," *Appl. Phys. Lett.,* vol. 105, p. 141101, 2014.

[14] H. Li, F. Reinhardt, L. Birch, G. Brodford, "High-efficient carbon-doped InGaAs/AlGaAs/GaAs Quantum well lasers," *J. Cryst. Growth,* vol. 263, p. 181, 2004.

[15] A. Bonanni, D. Stifter, A. Montaigne, K. Schmidegg, K. Hingerl, H. Sitter, "In situ spectroscopic ellipsometry of MOCVD-grown GaN compounds for on-line composition determination and growth control," *J. Crys. Growth.,* vol. 248, p. 211, 2003.

[16] M. Aagesen, "MBE grown nanorod and nanoplates," PhD thesis, University of Copenhagen, 2007.

[17] "Deposition Technology for beginners, how MOCVD works," AIXTRON SE · Dornkaulstr. 2 · 52134 Herzogenrath · Germany. [Online]. Available:

https://www.aixtron.com/fileadmin/documents/Brochures/How_MOCVD_works.pdf [accessed 15 08 2017].

[18] N. Eassa, "Surface modifications of InAs: Effect of chemical processing on electronic structure and photoluminescent properties," PhD thesis, Nelson Mandela Metropolitan University, 2012.

[19] T. Glatzel, S. Sadewasser, M. C.Lux - Steiner, "Kelvin probe force microscopy on III-V semiconductors: the effect of surface defects on the local work function," *Mater. Sci. Eng., B,* vol. 102, p. 138, 2003.

[20] Y. Wu, A. R. Chew, G. A. Rojas, G. Sini, G. Haugstad, A. Belianinov, S. V. Kalinin, H. Li, C. Risko, J. L. Bredas, A. Saleo, C. D. Frisbie, "Strain Effect on the work function of an organic semiconductor," *Nature. Com,* vol. 10, p. 1038, 2016.

[21] W. Melitz, J. Shen, A. Kummel, S. Lee, "Kelvin probe force microscopy and its application," *Surf. Sci. Rep.,* vol. 66, p. 1, 2011.

[22] K. Khaled, "Development of nano-probe techniques for work function assessment and application to materials for microelectronics," PhD thesis, Grenoble University, 2010.

[23] S. Dobson, "Development of Polymer Templates for ZnO Nanorods," Master thesis, Nelson Mandela Metropolitan University, 2014.

[24] G. Binnig, H. Rohrer, "Scanning Tunneling Microscopy-from Birth to Adolescence," 1986.

[25] J. C. Chen, "Introduction to Scanning Tunneling Microscopy," Oxford University Press, 2008.

[26] G. Binning, H. Rohrer, C. Gerber, E. Weibel, "Surface Studies by Scanning Tunneling Microscopy," *Phys. Rev. Lett.,* vol. 49, p. 57, 1982.

[27] U. Perera, "STM investigation of Charge-Transfer and Spintronic Molecular Systems," PhD thesis, Ohio University, 2011.

[28] M. Schunack, "Scanning Tunneling Microscopy Studies of Organic Molecules on Metal Surfaces," PhD thesis, Aarhus University, 2002.

[29] P. Ponath, "Construction and Assembly of a Scanning Tunneling Microscopy," Master thesis, Texas University, 2011.

[30] E. Meyer, "Atomic Force Microscopy," *Prog. Surf. Sci.,* vol. 41, p. 3, 1992.

[31] P. D. Szkutnik, A. Piednoir, A. Ronda, F. Marchi, D. Tonneau, H. Dallaporta and M. Hanbucken , "STM studies: spatial resolution limits to fit observations in nanotechnology," *Appl. Surf. Sci.,* vol. 164, p. 169, 2000.

[32] G. Binnig and C. F. Quate, "Atomic Force Microscopy," *Phys. Rev. Lett.,* vol. 56, p. 930, 1986.

[33] S. P. Sullivan, "At the nanoscale : a surface chemistry approach to the production, characterization, and modification of nanowires, Nanostructures and nanofibres," PhD thesis, Delaware University, 2008.

[34] G. Enevoldsen, "Scanning Probe Microscopy Studies of a metal Oxide Surface-a detailed study of the TiO2(110) surface," PhD thesis, Aarhus University, 2007.

[35] V. L. Mirinov, "Fundamentals of the scanning probe microscopy," 2004. [Online]. Available: http://ipmras.ru/UserFiles/publications/mironov/Fundamentals_SPM.pdf [accessed 15 08 2017].

[36] B. Bhushan, O. Marti, Chapter 2: "Scanning Probe microscopy-principles of operation, instrumentation and probes," Springer, Ed., in nanotribology and nanomechanics I: Measurement technique and namechanics, 2011.

[37] L. Liu, N. Xi, G. Li, H. Cheng, Chapter 4: Atomic Force Microscope-Based Nanorobotic System for Nanoassembly, first ed., Elsevier, p. 53, 2011.

[38] C. Rhodes, "Materials Science and Sensing Applications of Surface Plasmon Resonance in Conducting Metal Oxides," Master thesis, North Carolina State University, 2007.

[39] Y.Martin, C.C.Williams, H.K.Wickrmasinghe, "Atomic force microscope–force mapping and profiling on a sub 100- Å scale," *J. Appl. Phys.,* vol. 61, p. 4723, 1987.

[40] Bruker Corporation, "Dimension Icon Instruction Manual," 2011.

[41] S. Sadewasser, "Kelvin Probe Force Microscopy", Springer Series in Surface Sciences, vol. 48, p. 7, 2012.

[42] R. Garcia, R. Perez, "Dynamic Atomic Force Microscopy Methods," *Surf. Sci. Rep.,* vol. 47, p. 197, 2002.

[43] O. Douheret, "High resolution electrical characterization of III-V materials devices," PhD thesis, Royal Institute Technology, 2004.

[44] I. Beinik, "Electrical Characterization of Semiconductor Nanostructures by Conductive Probe Based Atomic Force Microscopy," PhD thesis, Institute of Physics Montanuniversitat Leoben, 2011.

[45] M. Guide, X. Dang, T. Nguyen, "Nanoscale Characterization of Tetrabenzoporphyrin and Fullerene-Based Solar Cells by Photoconductive Atomic Force Microscopy," *Adv. Mater.,* vol. 23, p. 2313, 2011.

[46] J. Hong, K. Noh, "Surface charge density and evolution of domain structure in triglycine sulfate determined by electrostatic-force microscopy," *Phys. Rev. B,* vol. 58, p. 151, 1998.

[47] M. Nonnenmacher, M. O'Boyle, H. Wickramasinghe, "Kelvin Probe Force Microscopy," *Appl. Phys. Lett.,* vol. 58, p. 2921, 1991.

[48] R. Diebold, M. Gordon, D. Clarke, "Effect of Silane Coupling Agent Chemistry on Electrical Breakdown Across Hybrid Organic−Inorganic Insulating Films," *ACS Appl. Mater. Interfaces,* vol. 6, p. 11932, 2014.

[49] P. Tejedor, L. Merino, I. Beinik, C. Teichert, "Conductive atomic force microscopy study of InAs growth kinetics on vicinal GaAs (110)," *Appl. Phys. Lett.,* vol. 95, p. 123103, 2009.

[50] H. Sakaguchi, F. Iwata, A. Hirai, A. Sasaki, T. Nagamura, "Nanometer-Scale Photoelectric Property of Organic Thin Films Investigated by a Photoconductive Atomic Force Microscope," *Jpn. J. Appl. Phys.,* vol. 38, p. 3908, 1999.

[51] B. D. Terris, J. E. Stern, D. Rugar, H. J. Mamin, "Contact Electrification Using Force Microscopy," *Phys. Rev. Lett.,* vol. 63, p. 2669, 1989.

[52] D. W. Abraham, C. Williams, J. Slinkman, H. K. Wickramasinghe, "Lateral dopant profiling in semiconductors by force microscopy using capacitive detection," *J. Vac. Sci. Technol. B.,* vol. 9(2), p. 703, 1990.

[53] Y. Liang, D. A. Bonnell, W. D. Goodhue, D. D. Rathman, C. O. Bozler, "Observation of electric field gradients near field- emission cathode arrays," *Appl. Phys. Lett.,* vol. 66, p. 1147, 1995.

[54] S. Watanabe, K. Hane, M. Ito, T. Goto, "Dynamic mode force microscopy for the detection of lateral and vertical electrostatic forces," *Appl. Phys. Lett.,* vol. 63, p. 2573, 1993.

[55] K. Domansky, Y. Leng, C. C. Williams, J. Janata, D. Petelenz, "Mapping of mobile charges on insulator surfaces with the electrostatic," *Appl. Phys. Lett.,* vol. 63, p. 1513, 1993.

[56] R. Bozek, "Application of Kelvin Probe Microscopy for Nitride Heterostructures," *Acta Phys. Pol., A,* vol. 108, p. 541, 2005.

[57] T. Glatzel, S. Sadewasser, M. C.Lux - Steiner, "Amplitude or Frenquency modulation - detection on Kelvin Probe Force Microscopy," *Appl. Surf. Sci.,* vol. 210, p. 84, 2003.

[58] A. Soininen, "An imcomplet guide to tapping mode, image postprocessing and life in general," 2013. [Online]. Available:

https://www.google.cm/search?q=An+imcomplet+guide+to+tapping+mode%2C+image+postprocessing+and+life+in+general%2C%22+2013.&oq=An+imcomplet+guide+to+tapping+mode%2C+image+postprocessing+and+life+in+general%2C%22+2013.&gs_l=psy-ab.3...3709.4602.0.6779.14.5.0.0.0.0.889.889.6-1.1.0....0...1.1.64.psy-ab..13.0.0.iBtv-MEtmg4 [accessed 15 08 2017].

[59] R. B. Darling, "Electrostatic and current transport properties of n+/semi-insulating GaAs Junction," *J. Appl. Phys.,* vol. 74, p. 4571, 1993.

[60] D. S. Mcgregor, R. A Rojeski, G. F.Knoll, F. L. Terry, Jr, J. East, Y. Eisen , "Present status of undoped semi-insulating LEC bulk GaAs as a radiation spectrometer," *Nucl. Instr. and Meth. in Phys Res . A,* vol. 343, p. 527, 1993.

[61] S. M. Sze, "Physics of semiconductor devices," 2nd ed., p. 18, 1981.

[62] J. Singh, "Semiconductor Devices Basic Principles," I. John Wiley and Sons, University of Michigan, p. 38.

[63] S. C. Jain and D. J. Roulston, "A simple expression for band gap narrowing (BGN) in heavily doped Si, Ge, GaAs and GexSi1-x strained layers," *Solid-State Electronics,* vol. 34, p. 453, 1991.

[64] H. Craig Casey Jr, "Properties of lattice - matched and strained Indium, Gallium Asernide," INSPEC, the Institution of Electrical Engineers, p. 65, 1993.

[65] W. Nakwaski, "Effective Masses of electrons and heavy holes in GaAs, InAs, AlAs and their ternary compounds," *Physica B,* vol. 210, p. 1, 1995.

[66] B. L. Sharma and R. K. Purohit, "Semiconductor Heterojunctions," Pergamon Press, p. 3, 1974.

[67] U. Zerweck, C. Loppacher, T. Otto, S. Grafström and M. Lukas, "Accuracy and resolution limits of Kelvin ProbeForce Microscopy," *Phys. Rev. B,* vol. 71, p. 125424, 2005.

[68] Y. Rosenwaks, R. Shikler, T. Glatzel, S. Sadewasser, "Kelvin Probe force Microscopy of semiconductor surface defects," *Phys. Rev. B,* vol. 70, p. 085320, 2004.

[69] H. O. Jacobs, H. F. Knapp, and A. Stemmer, "Practical aspects of Kelvin probe force microscopy," *Rev. Sci. Instrum.,* vol. 70, p. 1756, 1999.

[70] H. O. Jacobs, O. Leuchtmann, O. J. Homan , A. Stemmer, "Resolution And contrast in Kelvin probe force microscopy," *J. Appl. Phys.,* vol. 84, p. 1168, 1998.

[71] C. Li, S. Minne, Y. Hu, J. Ma, J. He, H. Mittel, V. Kelly, N. Erina, S. Guo, T. Mueller, "Peak Force Kelvin probe force Microscopy," 2013.

[72] J. Colchero, A. Gil and A. M. Baro, "Resolution enhancement and improved data interpretation in electrostatic force microscopy," *Phys. Rev. B,* vol. 64, p. 245403, 2001.

[73] H. L. Ehlers, A. W. R. Leitch, J. S. Vermaak, "Scanning photoluminescence study of the spatial uniformity of the growth rates of OMVPE grown GaAs quantum wells," *J. Cryst. Growth,* vol. 96, p. 101, 1989.

[74] http://www.brukerafmprobes.com/Product.aspx?ProductID=3950 [Online]. [accessed 15 08 2017].

[75] T. Glatzel, S. Sadewasser, M. C.Lux - Steiner, "Amplitude or Frenquency modulation -

detectionon Kelvin Probe Force Microscopy," *Appl. Surf. Sci.,* vol. 210, p. 84, 2003.

[76] F. Robin, H. Jacobs, O. Homan, A. Stemmer, W. Bachtold, "Investigation of the cleaved surface of a p-i-n laser using kelvin probe force microscopy and two-dimensional physical simulations," *Appl. Phys. Lett.,* vol. 76, p. 2907, 2000.

[77] T. Mizutani, T. Usunami, S. Kishimoto, K. Maezawa, "Measurement of contact potential of GaAs/AlGaAs heterostructure using Kelvin Probe Force Microscopy," *Jpn. J. Appl. Phys.,* vol. 38, p. 767, 1999.